Effects of Hydrodynamic Interaction on an AUV Operating Close to a Moving Submarine

by
Zhi Quan Leong, BE (Ocean Engineering)
National Centre for Maritime Engineering and Hydrodynamics
Australian Maritime College

Submitted in fulfilment of the requirements for the degree of Doctor of Philosophy
University of Tasmania

November 2014

[Page intentionally left blank]

DECLARATIONS

Declaration of Originality and Authority of Access

This thesis contains no material which has been accepted for a degree or diploma by the University or any other institution, except by way of background information and duly acknowledged in the thesis, and to the best of my knowledge and belief no material previously published or written by another person except where due acknowledgement is made in the text of the thesis, nor does the thesis contain any material that infringes copyright.

This thesis may be made available for loan and limited copying and communication in accordance with the Copyright Act 1968.

……...

Zhi Quan Leong (November 4, 2014)

Statement of Published Work Contained in Thesis

The publishers of the papers comprising Chapters 2 to 5 hold the copyright for that content, and access to the material should be sought from the respective journals and conference proceedings. The remaining non published content of the thesis, Chapter 6 to 7, are submitted and under review, and may be made available for loan and limited copying and communication in accordance with the Copyright Act 1968.

Statement of Co-Authorship

The following people and institutions contributed to the publication of work undertaken as part of this thesis:

- Zhi Quan Leong, University of Tasmania (**Candidate)**
- Prof. Dev Ranmuthugala, University of Tasmania (**Author 1)**
- Dr Irene Penesis, University of Tasmania (**Author 2)**
- Dr Hung Nguyen, University of Tasmania (**Author 3)**
- Dr Jonathan Duffy, University of Tasmania (**Author 4)**
- Khairul Mat Saad, University of Tasmania (**Author 5)**

Publication list and proportion of work details:

Chapter 2 (Paper 1) **RANS-based CFD Prediction of the Hydrodynamic Coefficients of DARPA SUBOFF Geometry in Straight-Line and Rotating Arm Manoeuvres** Candidate was the primary author and with Author 1 contributed to the design of the analysis, its formalisation and development. Author 2 and Author 3 assisted with refinement and presentation. [Candidate: 70%, Author 1: 15%, Author 2: 10%, Author 3: 5%]
• Chapter 3 – Part A (Paper 2) **Computational Fluid Dynamics Re-Mesh Method to Generating Hydrodynamic Models for Manoeuvring Simulation of Two Submerged Bodies in Relative Motion** Candidate was the primary author and with Author 1 contributed to the design of the analysis, its formalisation and development. Author 3 contributed to manuscript preparation. Author 2 assisted with refinement and presentation.

[Candidate: 70%, Author 1: 15%, Author 2: 5%, Author 3: 10%]
Chapter 3 – Part B (Paper 3) **Numerical Simulation of Spheres in Relative Motion using Dynamic Meshing Techniques** Candidate was the primary author. Author 1, Author 2, and Author 3 assisted with refinement and presentation. [Candidate: 75%, Author 1: 15%, Author 2: 5%, Author 3: 5%]
Chapter 4 (Paper 4) **Investigation into the Hydrodynamic Interaction Effects on an AUV Operating Close to a Submarine** Candidate was the primary author. Author 1 and Author 4 assisted with refinement and presentation. Author 5 contributed to the experimental data. [Candidate: 70%, Author 5: 10%, Author 1: 10%, Author 4: 10%]
Chapter 5 (Paper 5) **Scaling and Relative Size Effects on the Hydrodynamic Interaction on an UUV Operating Close to a Submarine** Candidate was the primary author. Author 1, Author 2, and Author 3 assisted with refinement and presentation. [Candidate: 70%, Author 1: 15%, Author 2: 10%, Author 3: 5%]
Chapter 6 (Paper 6) **Quasi-Static Analysis of the Hydrodynamic Interaction Effects on an Autonomous Underwater Vehicle Operating in Proximity to a Moving Submarine** Candidate was the primary author. Author 1, Author 2, and Author 3 assisted with refinement and presentation. [Candidate: 70%, Author 1: 15%, Author 2: 7.5%, Author 3: 7.5%]
Chapter 7 (Paper 7) **Hydrodynamic Interaction Effects on an Autonomous Underwater Vehicle Operating in Proximity and In Relative Motion to a Moving Submarine** Candidate was the primary author. Author 1, Author 2, and Author 3 assisted with refinement and presentation. [Candidate: 70%, Author 1: 15%, Author 2: 7.5%, Author 3: 7.5%]

We the undersigned agree with the above stated "proportion of work undertaken" for each of the above published (or submitted) peer-reviewed manuscripts contributing to this thesis

Signed:

……...

Prof. Dev Ranmuthugala

Primary Supervisor

National Centre for Ports
and Shipping
University of Tasmania

Date: …4/11/2014…

Dr Hung Nguyen

Co-Supervisor

National Centre for Ports
and Shipping
University of Tasmania

Date: …4/11/2014…

……...

Dr Irene Penesis

Co-Supervisor

National Centre for Maritime
Engineering and Hydrodynamics
University of Tasmania

Date: …4/11/2014…

……...

Dr Shuhong Chai

Acting Director

National Centre for Maritime
Engineering and Hydrodynamics
University of Tasmania

Date: 4/11/14

Acknowledgements

It is hard to believe my wonderful journey is coming to an end. However, the completion of this thesis marks the beginning of another great adventure ahead. Thus, it is with great pleasure to thank the many people who made this thesis possible.

First and foremost I wish to thank my supervisors Prof. Dev Ranmuthugala, Dr Irene Penesis, and Dr Hung Nguyen. It is difficult to overstate my gratitude to them as they have not only been great supervisors but also great mentors. Throughout my thesis, they have provided encouragement, sound advice, good company, and an invaluable amount of feedback and insight with regard to the technical and editorial components of the research. I hope that I can in turn pass on the research virtues that they have so generously shared. I would like recognise Max Haase, Christopher Polis, Phillip Marsh, Alex Conway, Dr Jalal Shahraki, and Khairul Mat Saad. They have been both brilliant colleagues and friends who have created a very memorable environment to work, to research and to celebrate. In particular, I would thank Khairul for his contribution to experimental work of this thesis.

Special thanks must go to:

- Dr Brendon Anderson and Dr Francis Valentinis from the Defence Science and Technology Organisation (DSTO) for their technical and financial support throughout the project.
- Luciano Mason, Dr Jonathan Binns, and Geli Kourakis for their dedication and continual work on the High Performance Cluster (HPC). The Computational Fluid Dynamics work presented in this thesis would not have been possible without the HPC.
- Dr Jonathan Duffy, Dr Gregor Macfarlane, Mr Tim Lilienthal, Kirk Meyer and Liam Honeychurch for their expertise and support in the setup and execution of the experimental work.
- David Graham and his team at LEAP Australia for providing the support on the ANSYS.

Lastly, and most importantly, I wish to thank my parents, Keng Yuen and Chai Peng for their unwavering love and support for me to pursue my dreams. To them I dedicate this thesis.

[Page intentionally left blank]

Abstract

The work detailed in this thesis investigates the behaviour of the hydrodynamic interaction effects acting on an unappended AUV manoeuvring in proximity to a larger moving underwater vehicle such as a submarine. The investigation examined the steady-state and transient interaction effects on the hydrodynamic coefficients of the AUV as a function of the relative: speed, longitudinal position, lateral position, and size between the two submerged vehicles. The work involved extensive development of Computational Fluid Dynamics (CFD) models to simulate the manoeuvres in order to map the interaction behaviour. Experimental Fluid Dynamics (EFD) involving captive-model tests of the two vehicles were carried out to validate and supplement the CFD data.

The results show that the hydrodynamic interaction acts to attract and repel the AUV at the stern and bow regions around the submarine, respectively. The magnitude of these attraction and repulsion interaction effects varied significantly due to small changes in the relative longitudinal position, suggesting the need of an accurate and fast responsive control system for the AUV to adequately maintain its trajectory around the submarine. These adverse interaction effects were found to be minimal around amidships of the moving submarine, suggesting a safe path for the AUV to approach or depart the submarine laterally within that region. In addition, the interaction effects on the hydrodynamic coefficients of the AUV were shown to reduce as the relative speed of the latter increased.

Due to the need to simulate large relative motions between the two vehicles, this thesis also investigate and identifies the merits of two dynamic mesh techniques within ANSYS CFX (i.e. Immersed Solids, and AMP Re-Meshing) to simulate multiple bodies in relative motion. Although the numerical models behind the techniques have undergone substantial development in recent years, as they are beta-features in ANSYS CFX there are currently no existing studies demonstrating their capabilities in modelling multiple bodies in relative motion. The developed CFD simulation models are suitable for future work involving appended AUVs and the coupling with a control system for manoeuvring simulations of multiple underwater vehicles.

[Page intentionally left blank]

Table of Contents

List of Figures XV

List of Tables XXI

Nomenclature XXII

Abbreviations XXV

Chapter 1 : Thesis Introduction 1

1.1 Introduction 2

1.1.2 Problem Definition 3

1.1.3 Objectives 5

1.2 Description of Geometry Model 5

1.3 Methodology 6

1.3.1 Assumptions and Limitations of the Investigation 7

1.4 Research Considerations 8

1.4.1 Hydrodynamic parameters 8

1.4.1 Geometrical Considerations 8

1.5 Novel Aspects 9

1.5 Outline of Thesis 11

Chapter 2 : RANS-based CFD Prediction of the Hydrodynamic Coefficients of DARPA SUBOFF Geometry in Straight-Line and Rotating Arm Manoeuvres 15

Abstract 16

2.1 Introduction 17

2.2 Geometry Model and Non-Dimensionalisation of Results 20

2.3.1 Simulation Setup 21

2.3.2 Discretisation Study 23

2.3.3 Comparison with Experiments 28

2.4 Rotating Arm Manoeuvre at Different Drift Angles 30

2.4.1 Simulation Setup 30

2.4.2 Verification of the Flow within the Rotational Domain 33

2.4.3 Discretisation Study 35

2.4.3 Comparison with Experiments 37

2.5 Conclusion 39

Chapter 3 : Dynamic Simulation of Two Bodies in Relative Motion 41

Chapter 3 : Part A - Computational Fluid Dynamics Re-Mesh Method to Generate Hydrodynamic Models for Maneuvering Simulation of Two Submerged Bodies in Relative Motion 43

Abstract 44

3A.1 Introduction 45

3A.2 Fluid Equation of Motion 46

3A.3 Body Equations of Motion 48

3A.4.1 CFD Re-Mesh Method 50

3A.4.2 Solution Process 51

3A.5 Results 52

3A.6 Conclusion 54

Chapter 3 : Part B - Numerical simulation of spheres in relative motion using dynamic meshing techniques 55

Abstract 56

3B.1 Introduction 57

3B.2 Numerical Model 59

3B.2.1 Single Sphere Model 59

3B.2.2 Two Spheres Model 61

3B.3 Numerical Simulation 62

3B.3.1 Single Sphere Simulations 62

3B.3.2 Two Spheres Motion Response Simulations 63

3B.4 Results and Discussion 63

3B.4.1 Single Sphere Results 63

3B.4.2 Two Spheres Results 65

3B.5 Conclusion 66

Chapter 4 : Investigation into the Hydrodynamic Interaction Effects on an AUV Operating Close to a Submarine 69

Abstract 70

4.1 Introduction 71

4.2 Investigation Programme 72

4.3 Numerical Simulation 74

4.4 Experimental Work And Validation 76
4.5 Results and Discussion 78
4.6 Conclusion 83
Chapter 5 : Scaling and Relative Size Effects on The Hydrodynamic Interaction on an UUV Operating Close to a Submarine 85
Abstract 86
5.1 Introduction 87
5.2 Investigation Programme 88
5.3 Simulation Setup 91
5.4 Experimental Work 92
5.5 CFD Verification and Validation 93
5.5.1 Mesh Independence Study 93
5.5.2 Validation against Experimental Data 94
5.6 Results and Discussions 97
5.6.1 Forward Speed 97
5.7 Conclusion 104
Chapter 6 : Quasi-static analysis of the hydrodynamic interaction effects on an autonomous underwater vehicle operating in proximity to a moving submarine 107
Abstract 108
6.1 Introduction 109
6.2 Investigation Programme 112
6.3 Simulation Setup 114
6.4 Experimental Work 115
6.5 CFD Verification and Validation 117
6.5.1 CFD Verification and Validation 117
6.5.2 Validation against Experimental Data 119
6.6 Results and Discussion 121
6.1 Forward Speed 121
6.2 Relative Size 123
6.3 Relative Longitudinal Position 126
6.4 Relative Lateral Position 129

6.7 Conclusion 132

Chapter 7 : Transient Analysis of Hydrodynamic Interaction Effects on an Autonomous Underwater Vehicle in Proximity of a Moving Submarine 135

Abstract 136

7.1 Introduction 137

7.2 Investigation Programme 140

7.3 Simulation Setup 142

7.4 Experimental Work 143

7.4.1 Experimental Setup 145

7.5 CFD Verification and Validation 146

7.5.1 Mesh Independence Study 146

7.5.2 Validation against Experiments 148

7.6 Results and Discussion 151

7.6.1 AUV Overtaking Manoeuvre 152

7.6.2 Submarine Overtaking Manoeuvre 158

7.7 Conclusion 160

Chapter 8 : Summary, Conclusions and Further Work 163

8.1 Summary 164

8.2 Conclusions 165

8.2.1 Behaviour of the Hydrodynamic Interaction 165

8.2.2 CFD, Experiments, and Modelling 167

8.3 Implications of the Research 169

8.4 Further Work 170

Bibliography 173

Appendix I: Uncertainty Analysis of the Experimental Data 179

Appendix II : Setup of the ANSYS Meshing Platform (AMP) Remeshing Method for Vehicles in Motion 183

Appendix III : The ANSYS CFX-MATLAB Interface 223

List of Figures

Figure 1.1: An AUV moving in the wake of a submarine. 3
Figure 1.2: SUBOFF (AUV) and Explorer (Submarine) geometries. 6
Figure 1.3: Axis system of the hydrodynamic forces and moments at the vehicle centre of buoyancy. 8
Figure 1.4: Positions on a submarine where recovery simulations were carried out by Fedor (2009). 10
Figure 2.1: DARPA SUBOFF unappended hull geometry. 18
Figure 2.2: Mesh model of the SUBOFF geometry. 21
Figure 2.3: Computational domain and coordinate systems for straight-line manoeuvre. 22
Figure 2.4: Percentage difference of the longitudinal force coefficient *X'*, lateral force coefficient *Y'*, and yawing moment coefficient *N'* predictions from the finest 7 million elements mesh solution vs number of mesh elements for the SUBOFF straight-line manoeuvre test case at a drift angle of 18°. 24
Figure 2.5: Percentage difference of the longitudinal force coefficient *X'*, lateral force coefficient *Y'* and yawing moment coefficient *N'* predictions as percentage difference from the y^+ of 0.5 solution versus y^+ for the SUBOFF straight-line manoeuvre test case at a drift angle of 18°. 26
Figure 2.6: Longitudinal force coefficient *X'*, lateral force coefficient *Y'*, and yawing moment coefficient *N'* predictions of different inflation layer total thickness versus y^+ for the SUBOFF straight-line manoeuvre test case at a drift angle of 18°. 27
Figure 2.7: CFD predictions and experimental measurements (Roddy 1990) of the longitudinal force coefficient *X'* versus drift angle β for the SUBOFF straight-line manoeuvre test cases. 29
Figure 2.8: CFD predictions and experimental measurements (Roddy 1990) of the lateral force coefficient *Y'* versus drift angle β for the SUBOFF straight-line manoeuvre test cases. 29
Figure 2.9: CFD predictions and experimental measurements (Roddy 1990) of the yawing moment *N'* versus drift angle β for the SUBOFF straight-line manoeuvre test cases. 30
Figure 2.10: Description of the rotating arm manoeuvre. 31
Figure 2.11: Computational domain and coordinate systems for rotating arm manoeuvre. 33
Figure 2.12: Velocity contour plot of the domain flow field at a rotational velocity of 1.312×10^{-1} radians/s, *Option 1* (top) and *Option 2* (bottom). The boundary line between the red and blue contours represents the flow where the linear velocity is 1.543m s^{-1}, while the yellow crosshair represents the intended location of the SUBOFF centre of buoyancy. 34
Figure 2.13: Velocity contour plot of the domain flow field with flow vectors superimposed at a rotational velocity of 1.312×10^{-1} radians/s, *Option 1* (top) and *Option 3* (bottom) 35
Figure 2.14: Percentage difference of the longitudinal force coefficient *X'*, lateral force coefficient *Y'* and yawing moment coefficient *N'* predictions from the finest 7.8 million elements mesh solution vs number of mesh elements for the SUBOFF rotating arm manoeuvre test case at a drift angle of 16° 36

Figure 2.15: Percentage difference of the longitudinal force coefficient *X*', lateral force coefficient *Y*' and yawing moment coefficient *N*' predictions as percentage difference from the y^+ of 0.5 solution versus y^+ for the SUBOFF rotating arm manoeuvre test case at a drift angle of 16° 37
Figure 2.16: CFD predictions and experimental measurements (Toxopeus et al. 2012) of the longitudinal force coefficient *X'*, lateral force coefficient *Y'*, and yawing moment coefficient *N'* versus drift angle for the SUBOFF rotating arm manoeuvre test cases. Error bars represent the uncertainty of the experimental measurements 38
Figure 3A.1: Interaction between vehicles (Saab 2012). 45
Figure 3A.2: Body fixed mesh simulation. 46
Figure 3A.3: Flowchart of the re-mesh method process. 50
Figure 3A.4: Flowchart of the solution procedure 52
Figure 3A.5: Mesh of two spheres (re-mesh) 53
Figure 3A.6: Sphere 1 (moving) – computed force X 53
Figure 3A.7: Sphere 2 (stationary) – computed force X 53
Figure 3B.1: CFD visualisation of the velocity field and streamlines around a sphere in motion. 58
Figure 3B.2: The single sphere computational domain. 60
Figure 3B.3: The MDARM mesh model. 60
Figure 3B.4: The ISM mesh model; sphere mesh (upper left), fluid domain mesh (bottom left). 61
Figure 3B.5: The two spheres computational domain. 61
Figure 3B.6: Mean drag coefficient of the single smooth sphere as a function of R_e. 63
Figure 3B.7: The *z*-displacements of the two spheres. 65
Figure 4.1: The 2.237:1 diameter ratio arrangement for both CFD and EFD. 73
Figure 4.2: Configurations investigated for the diameter ratios of 2.237:1 and 13.425:1 74
Figure 4.3: Computational fluid domain. 74
Figure 4.4: Mesh domain of the 2.237:1 diameter ratio model. 75
Figure 4.5: Grid independence study of the drag force for the diameter ratios of 2.237:1 and 13.425:1. 76
Figure 4.6: Grid independence study of the sway force for the diameter ratios of 2.237:1 and 13.425:1. 76
Figure 4.7: (a) SUBOFF testing rig (b) SUBOFF located adjacent to NP01. 77
Figure 4.8: Drag force coefficient vs R_{Long} at $Re_{SUBOFF} = 1.611x10^6$ (2.237:1 diameter ratio), error bars of the experimental results are at a value of 1.191E-04. 78
Figure 4.9: Sway force coefficient vs R_{Long} at $Re_{SUBOFF} = 1.611x10^6$ (2.237:1 diameter ratio), error bars of the experimental results are at a value of 1.191E-04. 78
Figure 4.10: Yaw moment coefficient vs R_{Long} for diameter ratio of 2:237:1. 79
Figure 4.11: Sway force coefficient vs R_{Long} for diameter ratio of 2:237:1. 79
Figure 4.12: Pressure visualisation vs R_{Long} at $Re_{SUBOFF} = 2.416x10^6$ and $R_{Lat} = 0.81$ for diameter ratio of 2:237:1. 80
Figure 4.13: Drag force coefficient vs R_{Long} for diameter ratio of 2:237:1 80
Figure 4.14: Yaw moment coefficient vs R_{Long} at a flow speed of $Re_{SUBOFF} = 2.416x10^6$ for diameter ratios of 2:237:1 and 13.425:1. 82

Figure 4.15: Sway force coefficient vs R_{Long} at a flow speed of Re_{SUBOFF} = 2.416x10^6 for diameter ratios of 2:237:1 and 13.425:1. 82
Figure 4.16: Drag force coefficient vs R_{Long} at a flow speed of Re_{SUBOFF} = 2.416x10^6 and at R_{Lat} = 1.34 for diameter ratios of 2:237:1 and 13.425:1. 82
Figure 4.17: Relative path for the AUV to approach the larger body with minimum hydrodynamic interaction. Forward speeds of the two bodies are matching. 83
Figure 5.1: An UUV moving in the wake of a submarine. 87
Figure 5.2: Definition of the model parameters. 89
Figure 5.3: Computation fluid domain. 91
Figure 5.4: Experimental testing rig. 92
Figure 5.5: SUBOFF support rig. 93
Figure 5.6: Percentage difference of the longitudinal force coefficient *X'*, lateral force coefficient *Y'*, and yawing moment coefficient *N'* predictions against the finest mesh solution versus number of mesh elements for the model scale and full-scale diameter ratios investigated. 94
Figure 5.7: CFD model of the experimental setup with the free surface and support rigs modelled. 95
Figure 5.8: CFD and experimental results of the longitudinal force coefficient *X'* (top), lateral force coefficient *Y*' (middle), and yawing moment coefficient *N*' (bottom) on the SUBOFF vs longitudinal separation ratio R_{Long} for a diameter ratio of 2.239 at $Re_{Explorer}$ = 2.466×10^6 and R_{Lat} = 1.70. 96
Figure 5.9: Longitudinal force coefficient *X'* (top), lateral force coefficient *Y*' (middle), and yawing moment coefficient *N*' (bottom) of the SUBOFF vs longitudinal separation ratio R_{Long} for the full-scale 2.239 diameter ratio at R_{Lat} = 1.70. 98
Figure 5.10: Interaction influence on the longitudinal force coefficient ($X'–X'_{Ref}$) of the SUBOFF vs longitudinal separation ratio R_{Long} for the full-scale 2.239 diameter ratio at R_{Lat} = 1.70 99
Figure 5.11: Interaction influence on the longitudinal force coefficient ($X'–X'_{Ref}$) vs longitudinal separation ratio R_{Long} for the length ratios of 12.362, 14.217 and 16.349; diameter ratio = 14.634, U =1.5m s^{-1} and R_{Lat} = 1.70 100
Figure 5.12: Interaction influence on the longitudinal lateral coefficient ($Y'–Y'_{Ref}$) vs longitudinal separation ratio R_{Long} for the length ratios of 12.362, 14.217 and 16.349; diameter ratio = 14.634, U =1.5m s^{-1} and R_{Lat} = 1.70 100
Figure 5.13: Interaction influence on the yawing moment coefficient ($N'–N'_{Ref}$) vs longitudinal separation ratio R_{Long} for the length ratios of 12.362, 14.217 and 16.349; diameter ratio = 14.634, U =1.5m s^{-1} and R_{Lat} = 1.70 101
Figure 5.14: Interaction influence on the longitudinal force coefficient ($X'–X'_{Ref}$) vs longitudinal separation ratio R_{Long} for the full-scale diameter ratios of 2.239 and 14.634; length ratio = 12.362, U =1.5m s^{-1} and R_{Lat} = 1.70 102
Figure 5.15: Interaction influence on the lateral force coefficient ($Y'–Y'_{Ref}$) vs longitudinal separation ratio R_{Long} for the full-scale diameter ratios of 2.239 and 14.634; length ratio = 12.362, U =1.5m s^{-1} and R_{Lat} = 1.70. 103

Figure 5.16: Interaction influence on the yawing moment coefficient ($N'–N'_{Ref}$) vs longitudinal separation ratio R_{Long} for the full-scale diameter ratios of 2.239 and 14.634; length ratio = 12.362, U =1.5m s^{-1} and R_{Lat} = 1.70.....103
Figure 5.17: Pressure coefficient contours of the flow around the SUBOFF and Explorer models at $Re_{Explorer}$ = 9.49×10^7 and R_{Lat} = 1.70 for the diameter ratios of (a) 2.239 and (b) 14.634. The pressure coefficient contour range is clipped at ±4.458×10^{-2}.....104
Figure 6.1: An AUV moving in the wake of a submarine.....109
Figure 6.2: Definition of the model parameters.....112
Figure 6.3: Computation fluid domain.....115
Figure 6.4: Experimental testing rig.....116
Figure 6.5: SUBOFF support rig.....116
Figure 6.6: Percentage difference of the longitudinal force coefficient X', lateral force coefficient Y', and yawing moment coefficient N' predictions from the finest mesh solution versus number of mesh elements for the model scale and full-scale diameter ratios investigated.....118
Figure 6.7: CFD model of the experimental setup with the free surface and support rigs modelled (top) and mesh model (bottom).....119
Figure 6.8: CFD and experimental results of the longitudinal force coefficient (X') on the SUBOFF vs longitudinal separation ratio (R_{Long}) for a diameter ratio of 2.239 at $Re_{Explorer}$ = 2.466×10^6 and R_{Lat} = 0.21.....120
Figure 6.9: CFD and experimental results of the lateral force coefficient (Y') on the SUBOFF vs longitudinal separation ratio (R_{Long}) for a diameter ratio of 2.239 at $Re_{Explorer}$ = 2.466×10^6 and R_{Lat} = 0.21.....121
Figure 6.10: CFD and experimental results of the yawing moment coefficient (N') on the SUBOFF vs longitudinal separation ratio (R_{Long}) for a diameter ratio of 2.239 at $Re_{Explorer}$ = 2.466×10^6 and R_{Lat} = 0.21.....121
Figure 6.11: Longitudinal force coefficient X' of the SUBOFF vs longitudinal separation ratio R_{Long} for the full-scale 2.239 diameter ratio at R_{Lat} = 0.21.....122
Figure 6.12: Lateral force coefficient Y' of the SUBOFF vs longitudinal separation ratio R_{Long} for the full-scale 2.239 diameter ratio at R_{Lat} = 0.21.....122
Figure 6.13: Yawing moment coefficient N' of the SUBOFF vs longitudinal separation ratio R_{Long} for the full-scale 2.239 diameter ratio at R_{Lat} = 0.21.....123
Figure 6.14: Interaction influence on the longitudinal force coefficient $X' – X'_{Ref}$ of the SUBOFF vs longitudinal separation ratio R_{Long} for the full-scale 2.239 diameter ratio at R_{Lat} = 0.21.....123
Figure 6.15: Interaction influence on the longitudinal force coefficient ($X' – X'_{Ref}$) vs longitudinal separation ratio R_{Long} for the full-scale diameter ratios of 2.239, 5.723, 14.634 at $Re_{Explorer}$ = 9.49×10^7 and R_{Lat} = 0.21.....124
Figure 6.16: Interaction influence on the lateral force coefficient ($Y' – Y'_{Ref}$) vs longitudinal separation ratio R_{Long} for the full-scale diameter ratios of 2.239, 5.723, 14.634 at $Re_{Explorer}$ = 9.49×10^7 and R_{Lat} = 0.21.....124
Figure 6.17: Interaction influence on the yawing moment coefficient ($N' – N'_{Ref}$) vs longitudinal separation ratio R_{Long} for the full-scale diameter ratios of 2.239, 5.723, 14.634 at $Re_{Explorer}$ = 9.49×10^7 and R_{Lat} = 0.21.....125

Figure 6.18: Pressure coefficient contours of the flow around the SUBOFF and Explorer models at $Re_{Explorer} = 9.49\times10^{7}$ and $R_{Lat} = 0.21$ for the diameter ratios of 2.239 on the left and 14.634 on the right. The pressure coefficient contour range is clipped at $\pm4.458\times10^{-2}$. 125
Figure 6.19: Interaction influence on the longitudinal force coefficient ($X' - X'_{Ref}$) vs longitudinal separation ratio R_{Long} for the full-scale diameter ratios of 14.634 at $Re_{Explorer} = 9.49\times10^{7}$, $Re_{SUBOFF} = 7.68\times10^{6}$ and $R_{Lat} = 0.21$. 127
Figure 6.20: Interaction influence on the lateral force coefficient ($Y' - Y'_{Ref}$) vs longitudinal separation ratio R_{Long} for the full-scale diameter ratios of 14.634 at $Re_{Explorer} = 9.49\times10^{7}$, $Re_{SUBOFF} = 7.68\times10^{6}$ and $R_{Lat} = 0.21$. 128
Figure 6.21: Interaction influence on the yawing moment coefficient ($N' - N'_{Ref}$) vs longitudinal separation ratio R_{Long} for the full-scale diameter ratios of 14.634 at $Re_{Explorer} = 9.49\times10^{7}$, $Re_{SUBOFF} = 7.68\times10^{6}$ and $R_{Lat} = 0.21$. 128
Figure 6.22: Pressure coefficient contour of the flow around the SUBOFF and Explorer at $Re_{Explorer} = 9.49\times10^{7}$ and $R_{Lat} = 0.21$ at different R_{Long} for a diameter ratio of 2.239. The pressure coefficient contour range is clipped at $\pm4.458\times10^{-2}$. 130
Figure 6.23: Interaction influence on the longitudinal force coefficient ($X' - X'_{Ref}$) vs longitudinal separation ratio R_{Long} at different R_{Lat} for the full-scale diameter ratio of 14.634 at $Re_{Explorer} = 9.49\times10^{7}$ and $Re_{SUBOFF} = 7.68\times10^{6}$. 131
Figure 6.24: Interaction influence on the lateral force coefficient ($Y' - Y'_{Ref}$) vs longitudinal separation ratio R_{Long} at different R_{Lat} for the full-scale diameter ratio of 14.634 at $Re_{Explorer} = 9.49\times10^{7}$ and $Re_{SUBOFF} = 7.68\times10^{6}$. 131
Figure 6.25: Interaction influence on the lateral force coefficient ($Y' - Y'_{Ref}$) vs longitudinal separation ratio R_{Long} at different R_{Lat} for the full-scale diameter ratio of 14.634 at $Re_{Explorer} = 9.49\times10^{7}$ and $Re_{SUBOFF} = 7.68\times10^{6}$. 131
Figure 6.26: Interaction influence on the longitudinal force coefficient ($X' - X'_{Ref}$), lateral force coefficient ($Y' - Y'_{Ref}$), and yawing moment coefficient ($N' - N'_{Ref}$) vs lateral separation ratio R_{Lat} for the full-scale diameter ratio of 14.634 at $R_{Long} = -0.45$, $Re_{Explorer} = 9.49\times10^{7}$ and $Re_{SUBOFF} = 7.68\times10^{6}$. 132
Figure 6.27: Relative path for the SUBOFF AUV to approach the Explorer submarine, where the hydrodynamic interaction is minimal. 132
Figure 7.1: An AUV moving in the wake of a submarine. 137
Figure 7.2: (a) AUV overtaking manoeuvre, (b) and submarine overtaking manoeuvre. 140
Figure 7.3: Definition of the model parameters. 141
Figure 7.4: Computational fluid domain. 143
Figure 7.5: SUBOFF undergoing a pure sway manoeuvre at a constant R_{Long} to the Explorer. 144
Figure 7.6: SUBOFF support rig. 145
Figure 7.7: Experimental testing rig. 146
Figure 7.8: Percentage difference of the longitudinal force coefficient X', lateral force coefficient Y', and yawing moment coefficient N' predictions against the finest mesh solution as a function of number of mesh elements for the model scale and full-scale diameter ratios investigated. 147
Figure 7.9: CFD model of the experimental setup, including the free surface and support rigs. 148

Figure 7.10: Mesh model of the experimental setup with the entrained water within the SUBOFF shell modelled to account for its inertia effects. 149
Figure 7.11: CFD and experimental results of the longitudinal force coefficient X' (top), lateral force coefficient Y' (middle), and yawing moment coefficient N' (bottom) on the SUBOFF as a function of longitudinal separation ratio R_{Long} for the diameter ratio of 2.239 at $Re_{SUBOFF} = 2.61\times10^6$, $Re_{Explorer} = 4.93\times10^6$, and $R_{Lat} = 1.70$. The error bars indicate the experimental uncertainty, i.e. 2.252×10^{-4} for the force coefficients and 1.446×10^{-4} for the moment coefficients. 150
Figure 7.12: CFD and experimental time traces of the longitudinal force coefficient X' and lateral force coefficient Y' on the SUBOFF for the 0.2Hz pure sway manoeuvre; $Re_{SUBOFF} = 2.09\times10^6$, $Re_{Explorer} = 3.95\times10^6$, and diameter ratio = 2.239. 151
Figure 7.13: Interaction influence on the SUBOFF's longitudinal force coefficient ($X'_{Interaction}$), lateral force coefficient ($Y'_{Interaction}$), and yawing moment coefficients ($N'_{Interaction}$) vs relative longitudinal position (R_{Long}) for the AUV overtaking the submarine at different relative speeds. 153
Figure 7.14: Pressure coefficient (C_P) contours of the flow around the SUBOFF and Explorer models at $R_{Long} = 0.00$ (top) and $R_{Long} = 0.25$ (bottom); $R_{Lat} = 0.15$. The pressure coefficient contour range is clipped at ±0.06. 154
Figure 7.15: Interaction influence on the SUBOFF's longitudinal force coefficient ($X'_{Interaction}$), lateral force coefficient ($Y'_{Interaction}$), and yawing moment coefficients ($N'_{Interaction}$) vs relative longitudinal position (R_{Long}) for the AUV overtaking the submarine at different R_{Lat}. The forward speeds of the SUBOFF and Explorer are 3.0 m/s and 1.5 m/s respectively (i.e. $U_0 = 1.5$ m/s, $U_r = 1.5$ m/s). 156
Figure 7.16: Power regression analysis of the interaction influence on the SUBOFF's longitudinal force coefficient ($X'_{Interaction}$), lateral force coefficient ($Y'_{Interaction}$), and yawing moment coefficients ($N'_{Interaction}$) as a function of R_{Lat} for the AUV overtaking the submarine at the R_{Long} of 0.4. The forward speeds of the SUBOFF and Explorer are 3.0 m/s and 1.5 m/s respectively (i.e. $U_0 = 1.5$ m/s, $U_r = 1.5$ m/s).....157
Figure 7.17: Interaction influence on the SUBOFF's longitudinal force coefficient ($X'_{Interaction}$), lateral force coefficient ($Y'_{Interaction}$), and yawing moment coefficients ($N'_{Interaction}$) vs relative longitudinal position (R_{Long}) for the submarine overtaking the AUV at different relative speeds. 158

List of Tables

Table 2.1: List of related CFD simulation studies of the SUBOFF geometry. 19
Table 2.2: Geometric characteristic of the SUBOFF model. 21
Table 2.3: Straight-line manoeuvre test case parameters. 22
Table 2.4: Theoretical estimates of the boundary layer thickness. 27
Table 2.5: Rotating arm manoeuvre test case conditions. 31
Table 2.6: Rotating arm manoeuvre test case parameters. 32
Table 3B.1: Properties of the spheres for the motion response simulation. 63
Table 3B.2: Computational effort of the simulations at $R_e = 10^6$ 65
Table 4.1: Summary of model parameters. 73
Table 5.1: Vehicle dimensions and test parameters. 90
Table 6.1: Vessel dimensions and test parameters. 113
Table 7.1: Vehicle dimensions and investigation parameters. 141
Table 7.2: Experimental parameters. 144

Nomenclature

a_y	Lateral acceleration (m s^{-2})
A_c	Characteristic Area (m^2) = $\pi D^2/4$
A_S	Surface area (m^2)
CB, B	Centre of buoyancy (m)
C_D	Drag coefficient (-) = $2F_D/(\rho U^2 A_c)$
C_P	Pressure coefficient (-) = $(p-p_\infty)/ (0.5\ p_\infty U^2)$
dz_a	Sphere analytical displacement (m) = $0.5N(m+m_a)t^2$
dz	Sphere displacement (m)
D	Diameter (m)
f	Lateral displacement frequency of the pure sway manoeuvre (s^{-1})
F_D	Drag force (N)
F_I	Inertia force (N)
F_s, F_b	Stable and apparent body forces
G	Centre of mass
I	Moments and products of inertia for body
K_{CFD}, M_{CFD}, N_{CFD}	Moment vector obtained from integrated body surface pressure and shear
K_P, M_P, N_P	Torque/moment obtained from a model of the propulsion system for body
L	Overall length (m)
L_S	Surface length (m)
m	Mass (kg)
m_a	Sphere estimated added mass (kg) = $(2/3)\pi(D/2)^3\rho$
N	Yawing moment (Nm)
N'	Yawing moment coefficient (-) = $N/(0.5\rho U^2 L^3)$
N'_{Ref}	Yawing moment coefficient without interaction influence
N	Net force of weight and buoyancy (N) = $mg - V\rho$ [Chapter 3B]
p, q, r	Angular velocities
P	Rotation origin (-) [Chapter 2]
P	Pressure (Pa)
P_∞	Freestream pressure (Pa)
O	Inertial coordinate system
r'	Non-dimensional rotation rate (-)
r	Rotational velocity, angular velocity (rad s^{-1})

R	Turning radius (m)
R, r	Position vector [Chapter 3A]
R_{Lat}	Lateral separation ratio
R_{Long}	Longitudinal separation ratio
Re	Reynolds number (-) = UL/υ
Re	Reynolds number (-) = UD/υ [Chapter 3A, 3B]
S	Static stability forces
T, t	Time (s)
u, v, w	Linear velocities
u_*	Friction velocity ($m^2\ s^{-1}$)
U	Velocity of body centre of buoyancy relative to freestream velocity ($m\ s^{-1}$)
U_0	Baseline forward velocity ($m\ s^{-1}$)
Ur	Relative velocity ($m\ s^{-1}$)
V_x	Linear velocity as a function of x ($m\ s^{-1}$)
V	Sphere volume (m^3) = $(4/3)\pi(D/2)^3$ [Chapter 3B]
x, y, z	Body axis cartesian coordinates in the x,y,z-direction (m)
$x_{distance}$	Longitudinal distance from the centre of buoyancy
X	Longitudinal force (N)
X'	Longitudinal force coefficient (-) = $X/(0.5\rho U^2 L^3)$
X'_{Ref}	Longitudinal force coefficient without interaction influence
X_{CFD}, Y_{CFD}, Z_{CFD}	Force vector obtained from integrated body surface pressure and shear
X_S, Y_S, Z_S	Weight and buoyancy component based on gravity vector
X_P, Y_P, Z_P	Thrust vector obtained from a model of the propulsion system for body
y_a	Lateral displacement amplitude of the pure sway manoeuvre (m)
$y_{distance}$	Relative lateral distance from the centre of buoyancy (m)
y_{wall}	Mesh node distance to wall (m)
Y	Lateral force (N)
Y'	Lateral force coefficient = $Y/(0.5\rho U^2 L^3)$
Y'_{Ref}	Lateral force coefficient without interaction influence
y^+	Non-dimensional wall distance (-) = $(u_* y_{wall})/\nu$
$\ddot{z}$	Sphere acceleration (m/s^2)
$\ddot{z}_a$	Sphere analytical acceleration (m/s^2) = $N(m+m_a)$
β	Drift angle (°)

ϕ, θ, ψ	Roll, pitch, yaw
ρ	Fluid density (kg m^{-3})
τ	Shear stress (Pa)
μ	Fluid dynamic viscosity (kg m^{-1} s^{-1})
ν, υ	Fluid kinematic viscosity (m^2 s^{-1}) = μ/ρ
∇	Volume (m^3)

Abbreviations

3D	Three-dimensional
ALE	Arbitrary Lagrangian-Eulerian
AMC	Australian Maritime College
AMCTT	Australian Maritime College Towing Tank
AMP	ANSYS Meshing Platform
AUV	Autonomous Underwater Vehicle
BSLRSM	Baseline Reynolds Stress Model
CFD	Computational Fluid Dynamics
CFL	Courant-Friedrichs-Lewy
DARPA	Defense Advanced Research Projects Agency
DNS	Direct Numerical Simulation
DOF	Degree-Of-Freedom
DSTO	Defence Science and Technology Organisation
EFD	Experimental Fluid Dynamics
HPC	High Performance Cluster
HPMM	Horizontal Planar Motion Mechanism
ITTC	International Towing Tank Conference
ISM	Immersed Solid Method
ISE	International Submarine Engineering
LES	Large Eddy Simulation
MATLAB	Matric Laboratory
MDARM	Mesh Deformation and Adaptive Remeshing Method
NCMEH	National Centre for Maritime Engineering and Hydrodynamics
RAN	Royal Australian Navy
RANS	Reynolds-Averaged Navier-Stokes
RINA	Royal Institution of Naval Architects
RBD	Rigid Body Dynamics
RNG	Re-Normalised Group
SA	Spalart-Allmaras
SSGRSM	Sarker and Gatski Reynolds Stress Model
SSK	Conventional Powered Submarine (classification)
SST	Shear Stress Transport
SSTCC	Shear Stress Transport with Curvature Correction
UUV	Unmanned Underwater Vehicle
WB	WorkBench

[Page intentionally left blank]

Chapter 1 :

Thesis Introduction

1.1 Introduction

An Autonomous Underwater Vehicle (AUV) is an underwater robot containing its own power and control systems to accomplish a pre-defined task with little operator intervention. In recent decades, the research and development of AUVs have grown significantly due to the recognition by AUV operators, such as the offshore oil and gas industry and the defence sector, for the ability of AUVs to operate independently of a human pilot in hazardous environments for long periods of time. This development has been aided by the significant improvement of relevant technologies such as power storage, navigation systems, control systems, and computational hardware which have increased the capabilities, applications, and efficiencies of AUVs. However, in the design of the autonomous capabilities of AUVs, there is still a substantial amount of work to be done in terms of its hydrodynamic stability and manoeuvrability. In particular, there is very little information on the hydrodynamic interaction between submerged vehicles within the public domain, let alone the transient interaction effects acting on an AUV manoeuvring in relative motion to a larger underwater vehicle. These interaction effects can substantially hinder the operation of multiple underwater vehicles operating in close proximity, such as the deployment and recovery of an unmanned underwater vehicle from a submarine (Hardy & Barlow 2008; Watt et al. 2011).

In 2006, a joint AUV development programme was initiated between the Defence, Science and Technology Organisation (DSTO) and the National Centre for Maritime Engineering and Hydrodynamics (NCMEH) at the Australian Maritime College (AMC). The aims of the programme were to explore both the design and operational challenges associated with the use of Unmanned Underwater Vehicles (UUVs) to meet the needs of the Royal Australian Navy (RAN); in particular, the RAN's vision to extend beyond single-vehicle undersea operations to multiple vehicles operating within a cooperative framework. In support of this approach, the work presented in this thesis was initiated and partially funded by DSTO to:

- provide insight into the effects of hydrodynamic interaction on an AUV manoeuvring near a larger moving underwater vehicle such as a submarine; and
- develop the means to investigate such interaction through an integration of Computational Fluid Dynamics (CFD) modelling and experimental work.

1.1.2 Problem Definition

Hydrodynamic interaction is classified as the external forces acting on a vessel that occur only when the vessel is close to another vessel or an obstruction such as an iceberg, the seabed, underwater structures, etc. (Mackay 2003; Acosta et al. 2008; Kimball & Rock 2011). When an AUV is manoeuvring in proximity to a moving submarine, interaction with the latter's wake and pressure fields can impose rapid changes in the acceleration of the AUV (Fedor 2009; see Figure 1.1). This can substantially hinder the approach and recovery of the AUV, and increase the risk of collision as the two vehicles draw closer. In extreme cases collision can result in damage or destruction of the AUV and possible damage to the submarine's appendages or sensors. Given that the AUV is relatively small and self-piloted by an on-board computer, the vehicle is more susceptible to the interaction effects. Therefore, it is important to have a good understanding of the AUV's behaviour under the effects of the interaction to enable the designers and operators to deal with rapid changes in the pressure and velocity fields. This includes developing control systems that are sufficiently robust and adaptive, improving the hydrodynamic design of the vehicle and developing operating procedures in order to improve the safety of the vehicle when manoeuvring in close proximity to a submarine.

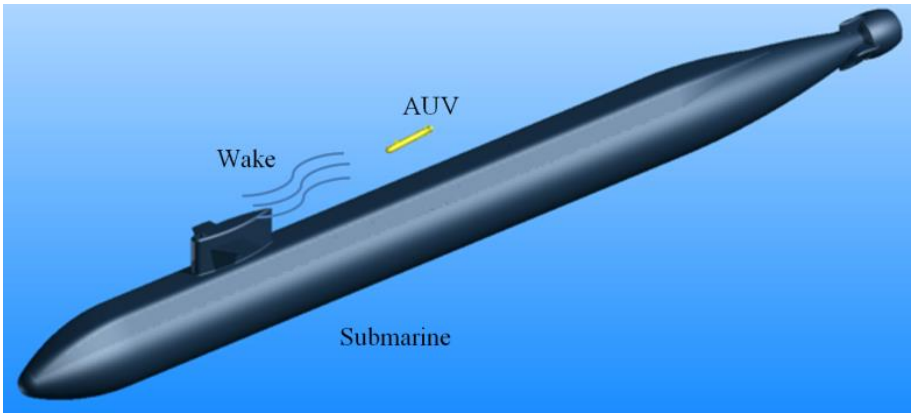

Figure 1.1: An AUV moving in the wake of a submarine.

In general, the hydrodynamic and manoeuvring characteristics of AUVs can be evaluated and quantified through experimental and empirical methods such as captive model testing and system identification of the actual vehicle respectively. However, these methods require considerable cost and time, and are restricted by the requisite of a physical model of the vehicle and suitable test facilities. In the case of multi-vehicle investigations, the cost can

significantly increase for each additional vehicle involved due to the measurement equipment and infrastructure required (Park et al. 2008).

For the prediction of the vehicle's hydrodynamic characteristics in unrestricted water; the facilities need to be sufficiently large to avoid excessive blockage effects (Quick et al. 2012), and sufficiently deep to avoid interaction effects with the free surface and the bottom of the tank (Mackay 2003). The size of the facility also imposes a speed restriction on the vehicle (Bertram 2000). For system identification of the vehicle's hydrodynamic characteristics from sea trials, the accuracy of the method is limited to the flow quality of the environment and the capability of the algorithms to estimate the hydrodynamic coefficients from the measured data (Pereira & Duncan 2000; Yoon & Rhee 2003; Xie et al. 2014). While many experimental studies have investigated hydrodynamic interactions between surface ships (Taylor 1909; Newman 1960; Remrey 1974; Kyulevcheliev & Varyani 2004; Kribel 2005), the hydrodynamic interaction effects between underwater vehicles in relative motion are harder to model and measure experimentally, due to their greater free-body motion in six degrees of freedom (6-DOF) and as such have not been as extensively investigated.

With the ongoing development of high performance computing facilities and numerical codes to predict fluid flow and pressure fields, computer based simulations using CFD are becoming more capable of replicating conditions that are difficult or costly to achieve through experimental processes. Properly developed Reynolds Averaged Navier-Stokes (RANS)-based CFD simulations have shown to be capable of predicting the hydrodynamic coefficients of underwater vehicles with a high degree of accuracy, and are comparable to experimental methods (Watt et al. 2006; Toxopeus 2008; Phillips 2010; Toxopeus 2012; Kim et al. 2013; Zhang et al. 2013). They offer a greatly reduced computational cost in comparison to Large Eddy Simulation (LES) and Direct Numerical Simulation (DNS) due to the lesser mesh requirement to capture the boundary layers on the vehicles (Alin et al. 2010). In addition, CFD has been demonstrated to capture interactions between surface ships with good agreement to experimental measurements (Chen et al. 2003; Huang and Chen 2003). This makes RANS-based simulations attractive to investigate the hydrodynamic interaction between multiple underwater vehicles by simulating conditions that are difficult or costly to achieve through experimental means, e.g. full-scale tests, free running vehicles, and flow visualisation. However, one of the major challenges faced when using CFD as an analysis tool is that the computational results can vary greatly depending on the experience of the

analyst, the settings utilised such as the boundary condition and the turbulence models, and the quality of the mesh model; thus necessitating verification through processes such as grid independence studies and validation through experimental or full-scale data.

Another numerical approach is potential flow modelling, which is widely accepted to be a lot faster and computationally cheaper to solve fluid flow problems compared to CFD. However, studies by many researchers (e.g. Kadri and Weihs, 2014; Jayrathne et al., 2014) show that potential flow modelling is unable to produce accurate force and moment predictions of the interaction effects between surface vehicles when compared to experimental measurements. This is due to the limited capability of potential flow solvers to model recirculating flow which is important to capture the wake behind a vehicle. Thus, CFD is used in this thesis.

1.1.3 Objectives

The aims of the project are to investigate the hydrodynamic behaviour of an AUV under the influence of the interaction with a larger moving underwater vehicle by examining the AUV's hydrodynamic coefficients for a range of relative positions and velocities between the two vehicles through CFD and experimental work. The motivation behind the study is to quantify the hydrodynamic interaction that significantly influences the AUV's ability to safely manoeuvre in close proximity to a submarine and identify a safe operational envelop. Thus, the specific research question for this project is:

What are the hydrodynamic interaction effects on an AUV manoeuvring in the proximity of a larger moving underwater vehicle?

Due to the previously mentioned challenges associated with CFD, experimental captive model tests were carried out in conjunction to validate the CFD models and supplement the investigation. Based on the work, the implications of the interaction behaviour on the AUV's safe operating envelope around the submarine, and guiding principles with regard to CFD modelling of the problem are presented.

1.2 Description of Geometry Model

The smaller (AUV) and the larger (submarine) vehicle models were represented by the following geometries. The smaller AUV is represented by the axisymmetric SUBOFF hull form (Groves et al. 1989) developed by the Defence Advanced Research Projects Agency (DARPA), while the larger body representing the submarine is a modified geometry based on the International Submarine Engineer Ltd. designed Explorer (ISE 2005). Figure 1.2 shows the geometries of the two vehicles.

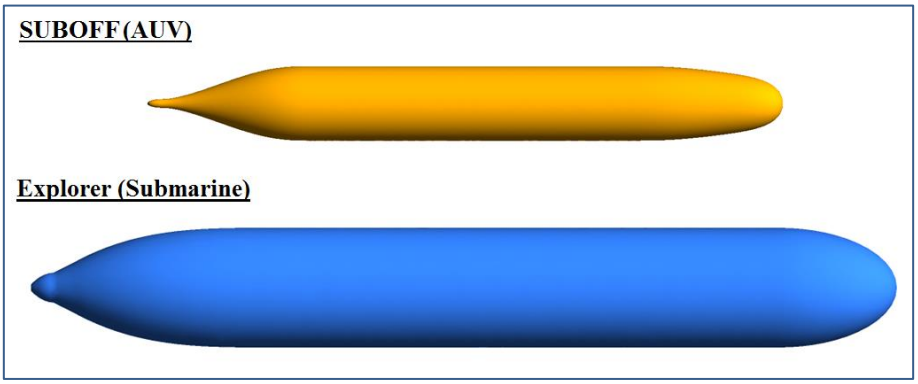

Figure 1.2: SUBOFF (AUV) and Explorer (Submarine) geometries.

1.3 Methodology

To achieve the outcomes of the study, the research question is addressed through three main components:

- a review of the literature on hydrodynamic interaction and its influence on the behaviour of multiple underwater vehicles operating in close proximity;
- development and validation of the CFD simulation model capabilities to capture the hydrodynamic characteristics of an AUV with and without the influence of the hydrodynamic interaction due to another nearby underwater vehicle; and
- analysis of the hydrodynamic interaction behaviour on an AUV operating at different positions and velocities relative to a larger moving underwater vehicle, including the effects of the relative size between the two vehicles on the interaction behaviour.

In order to establish confidence in the accuracy and findings of the latter two components, a build-up approach was undertaken. The approach is broken down into the following phases:

Phase 1: Evaluation of the CFD simulation model capability to predict the hydrodynamic characteristics of the SUBOFF geometry.

Phase 2: Development of the CFD model to simulate two underwater bodies in relative motion.

Phase 3: Validation of the hydrodynamic interaction between the SUBOFF and Explorer hull forms via scaled-model captive experimental work, including the means to extrapolate the CFD model-scale results to full-scale.

Phase 4: Steady-state analysis of the hydrodynamic interaction effects on the SUBOFF hull form at different relative positions to the Explorer hull form, including the influence of varying the relative size between the two geometries.

Phase 5: Transient analysis of the hydrodynamic interaction effects on the SUBOFF vehicle when overtaking and being overtaken by the Explorer vehicle at different lateral distances and relative velocities.

1.3.1 Assumptions and Limitations of the Investigation

The current study focuses only on the unappended configuration of the vehicles. This allows the hydrodynamic interaction between the barehulls of the vehicles to be the focal point of the study, thus enabling an unadulterated investigation into the interaction behaviour of the two vehicles due to the effects of relative size, position, and velocity between them. The study also focuses on the interaction behaviour between the vehicles at a zero incidence angle with the flow. The result of this work can then be compared against future work on fully appended configurations of the two vehicles at different incidence angles in order to quantify the contribution of the appendages and incidence angles to the interaction behaviour.

The test speeds carried out to investigate the interaction behaviour between the vehicles are assumed to induce fully turbulent flows around the vehicles (i.e. $Re > 1 \times 10^6$). They also correspond to operating speeds commonly encountered for underwater vehicles (Gertler, 1950; Joubert, 2006).

1.4 Research Considerations

1.4.1 Hydrodynamic parameters

This study focuses on the forces and moments induced on an AUV as a result of the hydrodynamic interaction when operating in close proximity to a submarine. The induced interaction force and moments are investigated as a function of relative position, size, and velocity between the two vehicles in order to characterise the interaction behaviour.

The hydrodynamic force and moments present in this study are based on the local coordinate system of the vehicles (see Figure 1.3). The hydrodynamic forces along the directions *x, y* and *z* are *X, Y,* and Z respectively, with the corresponding moments being *K, M, and N*. As the flow conditions investigated in this study predominantly aligned with the longitudinal axis of the vehicle, the overall length of the vehicle was used as the characteristic length for the non-dimensionalisation of the hydrodynamic forces and moments, as well as for Reynolds scaling. The equations and notations used in this thesis are defined in the Nomenclature Section and is in accordance with the ITTC Symbols and Terminology List (ITTC, 2011b), unless otherwise stated.

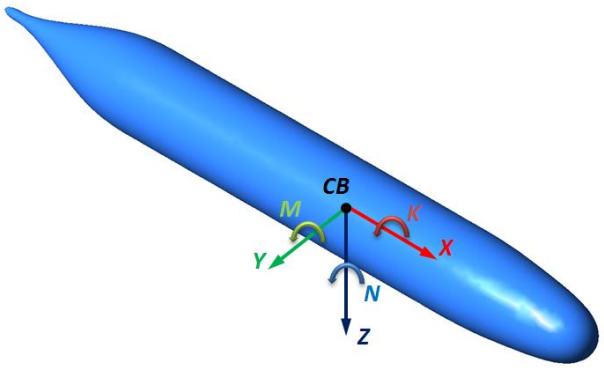

Figure 1.3: Coordinate system and the hydrodynamic forces and moments acting at the vehicle's centre of buoyancy.

1.4.1 Geometrical Considerations

This study aims to investigate the interaction behaviour between an AUV and a conventional submarine under full-scale conditions. However, such measurements are difficult to obtain using actual vehicles due to the difficulties associated with the availability and accessibility

to such vehicles and the risk of collision damage to the vehicles. Furthermore, experimental full-scale model testing is generally prohibitive due to cost and space. Therefore, experimental captive scaled model tests were used to validate the CFD models in this study. This enabled the validated CFD models to be used for the analysis of the interaction under full-scale conditions. An analysis of the validity and reliability of extending the CFD simulation from model-scale to full-scale conditions is presented in Chapter 5.

1.5 Novel Aspects

There are three areas in which this project provides original contributions to the field. The first is that it is a pioneering study that investigates and quantifies the hydrodynamic interaction effects between underwater vehicles in relative motion; in particular an AUV operating in close proximity to a larger moving underwater vehicles such as a submarine. Although a few studies on the interaction of underwater vehicles exist within the public domain, they provide limited contribution, as discussed below.

Bryne (1998) developed a real-time manoeuvring simulator to evaluate and demonstrate the manoeuvring and control performance of the Phoenix AUV undertaking a docking operation via the torpedo tube of a moving submarine. The hydrodynamic interaction between the two vehicles was modelled by introducing a parabolic flow velocity profile along the submarine hull in order to represent the reduced flow velocity encountered by the AUV as it approached the boundary layer of the submarine. However, this is an over-simplification of the interaction effects, since it did not account for operational issues associated with the more dominant potential field effects generated by a moving submarine that can either repel or attract the AUV depending on their relative positions.

Fedor (2009) investigated a feasible region to conduct a recovery of an UUV by a submarine. The study involved three-dimensional (3-D) steady-state CFD simulations of an UUV fixed within four regions adjacent to the submarine at different distances from the submarine hull as shown in Figure 1.4. The findings of the study suggest that Region 1 would be the most feasible as it offered the least disturbance away from the large trailing wakes of the sail present in Regions 3 and 4. The observed repulsion force acting on the UUV as it moved closer to the submarine was greater in Region 2 than in the other regions. With regard to the

limitations of the study, the simulations were steady-state in nature (i.e. vehicles were travelling at the same forward speed and fixed relative positions) and were carried out for only four regions relative close to the submarine. Therefore, it is uncertain how far the interaction effects extend, and how the interaction effects evolve as the UUV approaches the locations at different relative speeds to the submarine

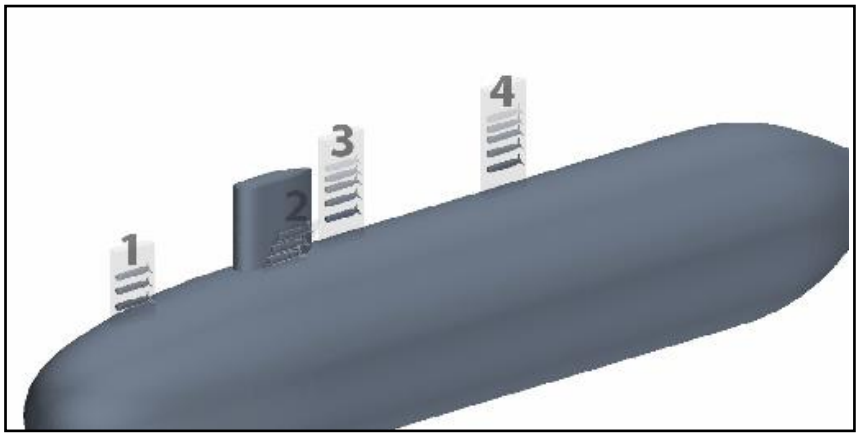

Figure 1.4: Positions on a submarine where recovery simulations were carried out by Fedor (2009).

The studies by Bryne (1998) and Fedor (2009) offered an insight into the interaction effects acting on an AUV operating within the proximity of a larger moving underwater vehicle such as a submarine. However, their investigations focused on locations very close to the submarine, thus the parameters surrounding the broader extent of the interaction effects (e.g. interaction influence of the submarine hull) and the means for the AUV to approach the regions investigated were not discussed. Furthermore, their studies were purely simulation-based, thus lacking experimental data to validate the predictions of the numerical models.

The second original contribution of this thesis is the application of two dynamic meshing methods under development within ANSYS CFX, i.e. Immersed Solids and ANSYS Meshing Platform (AMP) Remeshing. These methods enable the vehicles within the CFD model to undergo large and relative motions, which is not possible using a body-fixed mesh approach. While the alogrithms behind the methods have undergone substantial development in recent years, there are currently no existing studies demonstrating their capabilities in modelling multiple bodies in relative motion, let alone their performance in terms of accuracy. Furthermore, the AMP Remeshing method is a beta feature in ANSYS CFX that has yet to be

fully integrated into the software, requiring a user-defined script for the method to work. It is noted that an alternative fully integrated remeshing method through the ICEM meshing module exist within ANSYS CFX. However, the ICEM method handles only translational mesh motion. This project presents the underlying concepts behind the methods, the evaluation of their performance in modelling underwater bodies in relative motion, and guiding principles in utilising the methods.

The third novelty of this project is the interface to couple the ANSYS CFX model with a MATLAB-based control system for future work. The coupled model is intended for use in a dynamic manoeuvring simulation to develop and trial control strategies for underwater vehicles undergoing close proximity manoeuvres before implementation. The nature of the CFD-MATLAB coupled environment moves beyond the primary aim of this thesis, and hence, demonstration of the environment's capabilities is presented in Appendix III.

1.5 Outline of Thesis

This thesis follows a "chapterised thesis" structure, where Chapters 2 to 7 comprises of scientific papers. The structure of the thesis is outlined below.

Chapter 1: The introductory chapter, which clarifies the research question, objectives, and methodology of the project, including a brief description of the issues and past work on the hydrodynamic interaction of underwater vehicles. It also outlines the structure of the thesis, linking together the subsequent chapters consisting of the academic papers.

Chapter 2: Examines the ability of RANS-based CFD to reproduce the experimentally measured forces and moments acting on an unappended SUBOFF geometry undergoing steady straight-line and rotating arm manoeuvres at different drift angles, showing that the selection of the boundary conditions and turbulence models, and the quality of the mesh model can have a considerable and independent effect on the computational results. The predictions of two of the most compressive RANS-based turbulence models: Baseline Reynolds Stress Model (BSLRSM) and Shear Stress Transport with Curvature Correction (SSTCC) are analysed for performance and computational cost, and compared to published experimental data for both manoeuvres, showing that with a sufficiently fine mesh, appropriate mesh treatment, verification of the simulated flow field, and simulation

conditions matching the experiments; the BSLRSM predictions offer good agreement with experimental measurements, at a relatively low increase in cost. The SSTCC model predictions are agreeable with the longitudinal force but fall outside the experimental uncertainty for both the lateral force and yawing moment. The CFD methodology and key findings from Chapter 2 are used to provide the basis and support for the more comprehensive simulations of the hydrodynamic interaction between the SUBOFF and Explorer geometries in the subsequent chapters.

Chapter 3: Introduces the underlying concepts behind the two dynamic mesh techniques within ANSYS CFX, i.e. Immersed Solids and AMP Remeshing, and an evaluation of their performance in terms of accuracy and computational speed for modelling fluid flow around spheres in motion. A comparison of their performance and requirements utilising the Shear Stress Transport k-omega (SST k-ω) and Baseline Reynolds Stress Model (BSLRSM) turbulences models as well as a laminar flow model to provide a baseline for computational speed comparison are also presented. The computational results were compared to published experimental data to benchmark their accuracy and efficiency. Coupled simulations of the fluid flow and Rigid Body Dynamics (RBD) solvers were also carried out to investigate the accuracy of the motion response predictions compared to analytical solutions for spheres in relative motion. The methodology and key findings from this modelling spheres are used to build up the CFD capabilities for the more comprehensive simulations of the SUBOFF and Explorer geometries in relative motion in Chapter 6.

Chapter 4: Investigates the hydrodynamic interaction effects on the hydrodynamic coefficients of the SUBOFF hull form at different relative longitudinal and lateral positions to the Explorer hull form. The analysis is conducted at model-scale through a series of steady-state CFD simulations and captive model experiments in the AMC towing tank. The simulations were carried out at different fixed speeds and relative positions for two diameter ratios, i.e. 2.237:1 and 13.425:1, by scaling the dimensions of the Explorer geometry while keeping the SUBOFF geometry consistent. The higher diameter ratio represents the relative size between a typical conventional (SSK) submarine and an AUV, while the lower diameter ratio was used for validation against the experimental results. The findings enabled the refinement of future two-body interaction simulation models in subsequent chapters, including the mesh structure, simulation settings, and analysis techniques. An initial assessment of the adverse implications of the interaction effects on an AUV approaching a

submarine is also presented, with locations experiencing minimum and maximum interaction effects identified.

Chapter 5: This chapter focuses on the analysis of the scaling and relative size effects on the hydrodynamic interaction behaviour between the SUBOFF and the Explorer hull forms at different relative longitudinal positions and velocities, and at one relative lateral position. The experimental results from captive scaled model tests were used to validate the steady-state CFD model, taking into consideration experimental limitations. This enables the validated CFD models to be used for further analysis of the interaction under full-scale conditions, including different diameter to length ratios between the two vehicles representing the operation between a typical UUV and a SSK submarine. An analysis of the validity and reliability of extending the CFD simulation from model-scale to full-scale conditions is also presented. The findings of this chapter provide the basis and support for the full-scale work in the subsequent chapters.

Chapter 6: Complements the work presented in Chapter 5 by examining the steady-state hydrodynamic interaction effects on the hydrodynamic coefficients of SUBOFF vehicle at different relative longitudinal and lateral positions to the Explorer vehicle under full-scale conditions. The study is conducted for three vehicles size ratios by scaling the dimensions of the SUBOFF geometry as required. The largest ratio represents the typical size ratio between an AUV and a SSK submarine. Validation is carried out at model-scale against experimental work carried out within the AMC towing tank. The analysis also includes flow visualisation to assist in the interpretation of the interaction behaviour. The implications of the interaction effects on the ability of an AUV to manoeuvre in close proximity to a submarine are also discussed.

Chapter 7: Presents the transient analysis of the hydrodynamic interaction effects on an AUV operating in close proximity and in relative motion to a larger moving submarine. The effects of relative motion on the interaction behaviour were investigated via two manoeuvres, i.e. the AUV overtaking and being overtaken by the submarine at different relative forward velocities and lateral distances. The SUBOFF and Explorer hull forms are used to represent the AUV and submarine respectively. The results presented are from a series of transient CFD simulations utilising the AMP Remeshing technique to model the vehicles in relative motion. Validation of the transient CFD model is carried out through captive scaled model

experiments. The results provide information on options to reduce the effects of the interaction on the AUV. An analysis of the AUV's control planes' ability to effectively manoeuvre under the influence of the interaction is also presented.

Chapter 8: The concluding chapter provides an overall summary of the project, bringing together the findings of the individual chapters. It also concludes on the findings and outcomes, as well as discussing the implications of the findings, the limitations, and the recommendations to meet the project requirements and for future work.

Appendices: Appendix I outline the uncertainty analysis of the experimental data for Chapters 4 to 7. **Appendix II** provides information on the setup of the AMP Remeshing method to model the vehicles in relative motion. **Appendix III** describes the setup and provides a demonstration of the interface to control the simulation of the vehicles in relative motion through a MATLAB environment.

Chapter 2 :

RANS-based CFD Prediction of the Hydrodynamic Coefficients of DARPA SUBOFF Geometry in Straight-Line and Rotating Arm Manoeuvres

This chapter has been accepted for publication in the "Transactions of the Royal Institution of Naval Architects, Part A1 – International Journal of Maritime Engineering" and at the time of writing will be published at the first available issue of the journal. The citation for the research article is:

Leong, Z.Q., Ranmuthugala, D., Penesis, I., & Nguyen, H. 2014, 'RANS-Based CFD Prediction of the Hydrodynamic Coefficients of DARPA SUBOFF Geometry in Straight-Line and Rotating Arm Manoeuvres', *Transactions RINA: Part A1- International Journal Maritime Engineering*. [Accepted for publication, 20 September 2014]

Chapter 3 :
Dynamic Simulation of Two Bodies in Relative Motion

This chapter consists of two subchapters:

Part A- Computational Fluid Dynamics Re-Mesh Method to Generate Hydrodynamic Models for Manoeuvring Simulation of Two Submerged Bodies in Relative Motion.

Part B- Numerical Simulation of Spheres in Relative Motion Using Dynamic Meshing Techniques.

[Page intentionally left blank]

Chapter 3 :

Part A -

Computational Fluid Dynamics Re-Mesh Method to Generate Hydrodynamic Models for Maneuvering Simulation of Two Submerged Bodies in Relative Motion

---

This subchapter has been published in the Journal of Computer Science and Cybernetics. The citation for the research article is:

Leong, Z.Q., Ranmuthugala, D., Penesis, I., & Nguyen, H. 2011, 'Computational Fluid Dynamics Re-Mesh Method to Generate Hydrodynamic Models for Manoeuvring Simulation of Two Submerged Bodies in Relative Motion', *Journal of Computer Science and Cybernetics*, vol. 27, no. 4, pp. 353-362.

Abstract

An Autonomous Underwater Vehicle (AUV) operating closer to a larger vessel experiences significant hydrodynamic forces requiring an adaptive control mechanism to maintain acceptable trajectory. It is therefore important that the designer understands the hydrodynamic characteristics of the vehicle in this scenario in order to develop appropriate control algorithms to deal with its dynamic behaviour. This requires developing simulations of the vehicle's behaviour close to the larger vessel, the control algorithms, and the dynamic interface between the two.

This paper presents a method to generate a complete hydrodynamic model of underwater vehicles using the Computational Fluid Dynamics (CFD) code ANSYS CFX, which can then be interfaced with the vehicle's control algorithms within a simulation environment. The essential aspect of the method is the re-mesh approach, where the mesh deforms locally around the bodies using an Arbitrary Lagrangian-Eulerian form of the governing fluid equations and re-meshes when the deformation significantly compromises the quality of the mesh. This overcomes the motion limitations imposed by a pure deforming mesh approach.
Preliminary work to validate the method is based on two smooth spheres moving relative to each other. It is found that this method is able to adequately simulate the fluid behaviour around the bodies. The paper also describes the future work focused on a 6-DOF AUV modelled in CFD to obtain its hydrodynamic behaviour to be interfaced to the control system within MATLAB.

3A.1 Introduction

When an AUV is operating close to a larger vessel such as a submarine or a surface ship, the hydrodynamic interactions between the two can be significant. Given that the AUV is relatively small, this interaction can adversely affect its trajectory, which in extreme cases can cause collision or loss of the vehicle. Therefore, it is essential that the AUV's control system is sufficiently robust and adaptive to deal with rapidly varying pressure and velocity fields around the vehicle (Figure 3A.1).

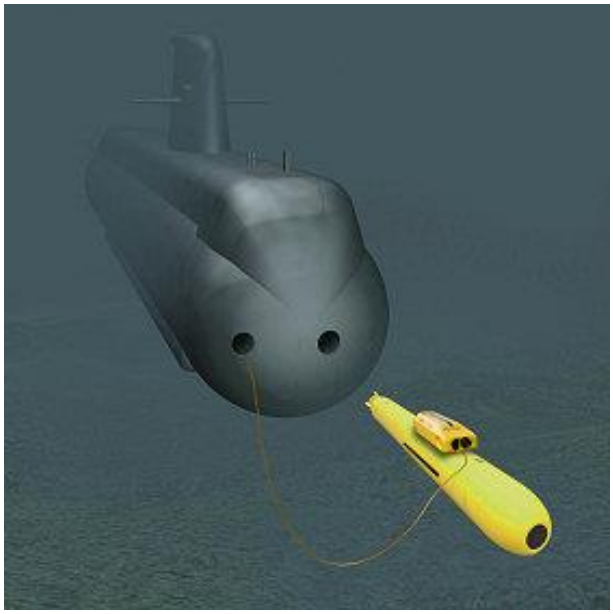

Figure 3A.1: Interaction between vehicles (Saab 2012).

In order to quantify the interaction between the two vehicles, it is required to conduct numerical and/or experimental work to obtain their hydrodynamic characteristics during operations in close proximity. One method of numerically obtaining this is to conduct CFD simulations of the vehicle manoeuvres to predict the resulting forces and moments, which will characterise the behaviour of the vehicles. This can then be fed into the control system simulation to develop the necessary algorithms to maintain the required trajectory.

To date, many of the numerical approaches to simulate the hydrodynamic characteristics adopt a body fixed mesh to simulate the flow around a body moving in 6 degrees-of-freedom (6-DOF). The fluid domain mesh is rigid and moves in 6-DOF with the body (Figure 3A.2).

However, this approach is not suitable for simulation of two bodies in relative motion since the bodies are fixed at a location relative to the fluid domain.

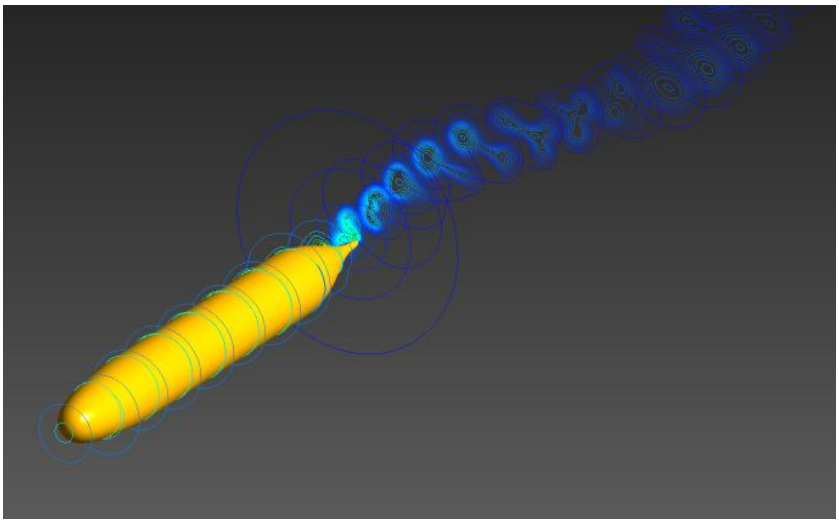

Figure 3A.2: Body fixed mesh simulation.

This paper describes the implementation of the re-mesh method which theoretically allows an arbitrary number of bodies in relative motion to be simulated. (Note: an example of CFD mesh used in the current simulation is shown in Figure 3A.5. The main purpose of this paper is to:

- present the underlying theory behind the re-mesh method and its implementation for 6-DOF simulations;
- outline the solution procedure of the simulation; and
- provide preliminary results of the method in terms of accuracy.

3A.2 Fluid Equation of Motion

The CFD re-mesh method requires an Arbitrary Lagrangian-Eulerian (ALE) form of the governing fluid equations to accommodate the deformation in the mesh and requires only the one apparent body force term for the linear accelerations. The ALE formulation allows the mesh motion to be defined independent of the motion of the fluid being analysed.

The mass momentum equations in ALE form are as shown below, where calculation of the mesh velocity u_{mj} is based on the domain boundary movement of the body.

Mass conservation:

$$\frac{\partial \rho}{\partial t} + \frac{\partial \rho \left(u_j - u_{mj} \right)}{\partial x_j} = 0 \tag{3A.1}$$

Momentum:

$$\frac{\partial \rho u_i}{\partial t} + \frac{\partial \rho u_i \left(u_j - u_{mj} \right)}{\partial x_j} = F_s + F_b \tag{3A.2}$$

where stable forces on the body F_s is

$$F_s = \frac{\partial p}{\partial x_i} + \frac{\partial}{\partial x_j}\left(\mu \frac{\partial u_i}{\partial x_j} \right) \tag{3A.3}$$

and the apparent body force F_b is

$$F_b = -\rho \frac{d_o^2 R}{dt^2} \tag{3A.4}$$

To account for the deforming mesh, the turbulence equations are also in ALE form:

k-equation:

$$\frac{\partial \rho k}{\partial t} + \frac{\partial \rho k (u_j - u_{mj})}{\partial x_j} = P_k - \beta' \rho k \omega + \frac{\partial}{\partial x_j}\left[\left(\mu + \frac{\mu_t}{\sigma_k} \right) \frac{\partial k}{\partial x_j} \right] \tag{3A.5}$$

ω-equation:

$$\frac{\partial \rho \omega}{\partial t} + \frac{\partial \rho \omega (u_j - u_{mj})}{\partial x_j} = \alpha \frac{\omega}{k} P_k - \beta \rho k \omega^2 + \frac{\partial}{\partial x_j}\left[\left(\mu + \frac{\mu_t}{\sigma_\omega} \right) \frac{\partial \omega}{\partial x_j} \right] \tag{3A.6}$$

Details on the turbulence model source terms are available in ANSYS (2011). An additional set of mesh displacement Laplace equations is added to solve the ALE formulation. The Laplace equations diffuse boundary motion into the interior of the fluid domain. The resulting solution, obtained by integrating over the time interval, allows for the extraction of the mesh velocity $u_{mj.}$ The set of Laplace equations is as follows:

Mesh displacement equations:

$$\frac{\partial \rho}{\partial x_j}\left(\Gamma \frac{\partial x_i'}{\partial x_j}\right) = 0 \tag{3A.7}$$

where

$$x_i' = x_i - x_i^0 \tag{3A.8}$$

The displacement diffusion coefficient Γ can be a function of near wall distance or mesh volume size.

3A.3 Body Equations of Motion

The set of equations described below is used to illustrate the coupling of the body equations of motion with the fluid equations of motion in ALE form for a 6-DOF simulation (Dajka et al. 2007). The body equations of motions, based on a translating coordinate system fixed to a submerged body and are as follows:

General equation of motion:

$$\sum F = m\dot{u}_G \tag{3A.9}$$

$$\dot{u}_G = \left(\dot{u}_O\right)_{xyz} + \omega u_O + \dot{\omega} r_G + \omega\left(\omega r_G\right) \tag{3A.10}$$

$$\sum M_O = \left([I]\alpha\right)_{xyz} + \left([I]\omega\right)\omega + + r_G m\dot{u}_G \tag{3A.11}$$

The moments of inertia are functions of time and evaluated at each new time interval where,

$$[\dot{I}]\omega + [I]\alpha = \frac{d([I]\omega)}{dt} \tag{3A.12}$$

This allows a system of equations to be solved to track the motion of the body, where axial (*x*-axis), lateral (*y*-axis), and normal (*z*-axis) forces are,

$$m[\dot{u} - x_G(q^2 + r^2) + y_G(pq - \dot{r}) + z_G(pr + \dot{q})] = X_{CFD} + X_S + X_P \tag{3A.13}$$

$$m[\dot{v} - y_G(r^2 + p^2) + z_G(qr - \dot{p}) + x_G(qp + \dot{r})] = Y_{CFD} + Y_S + Y_P \tag{3A.14}$$

$$m[\dot{w} - z_G(p^2 + q^2) + x_G(rp - \dot{q}) + y_G(rq + \dot{p})] = Z_{CFD} + Z_S + Z_P \tag{3A.15}$$

with the force vectors obtained from the stable and apparent forces. Similarly rolling (*x*-axis), pitching (*y*-axis) and yawing (*z*-axis) moment are,

$$I_x\dot{p} - I_{zx}\dot{r} - I_{xy}\dot{q} - \dot{I}_x p - \dot{I}_{zx} r - \dot{I}_{xy} q + m[y_G\dot{w} - z_G\dot{v}] = K_{CFD} + K_S + K_P \tag{3A.16}$$

$$I_y\dot{q} - I_{xy}\dot{p} - I_{yz}\dot{r} + \dot{I}_y q - \dot{I}_{xy} p - \dot{I}_{yz} r + m[z_G\dot{u} - x_G\dot{w}] = M_{CFD} + M_S + M_P \tag{3A.17}$$

$$I_y\dot{r} - I_{yz}\dot{q} - I_{zx}\dot{p} + \dot{I}_z r - \dot{I}_{yz} q - \dot{I}_{zx} p + m[x_G\dot{v} - y_G\dot{u}] = N_{CFD} + N_S + N_P \tag{3A.18}$$

This results in a matrix system:

$$\begin{pmatrix} m & 0 & 0 & 0 & mz_G & -my_G \\ 0 & m & 0 & -mz_G & 0 & mx_G \\ 0 & 0 & m & my_G & -mx_G & 0 \\ 0 & -mz_G & my_G & I_x & -I_{xy} & -I_{zx} \\ mz_G & 0 & -mx_G & -I_{xy} & I_y & -I_{yz} \\ -my_G & mx_G & 0 & -I_{zx} & -I_{yz} & I_z \end{pmatrix} \begin{pmatrix} \dot{u} \\ \dot{v} \\ \dot{w} \\ \dot{p} \\ \dot{q} \\ \dot{r} \end{pmatrix} = \begin{pmatrix} X_{RHS} - X_{LHS} \\ Y_{RHS} - Y_{LHS} \\ Z_{RHS} - Z_{LHS} \\ K_{RHS} - K_{LHS} \\ M_{RHS} - M_{LHS} \\ N_{RHS} - N_{LHS} \end{pmatrix} \tag{3A.19}$$

The solution of the matrix system results in estimates at the new time level of accelerations $(\dot{u}, \dot{v}, \dot{w}, \dot{p}, \dot{q}, \dot{r})$, which in turn with the known time step allow for calculation of velocities (u, v, w, p, q, r).

The auxiliary derivatives in the inertial frame $(\dot{x}_0, \dot{y}_0, \dot{z}_0, \dot{u}_0, \dot{v}_0, \dot{w}_0, \dot{\phi}, \dot{\theta}, \dot{\psi})$ is then integrated to obtain the new position and angular movement $(x_0, y_0, z_0, \phi, \theta, \psi)$.

3A.4 BODY EQUATIONS OF MOTION

3A.4.1 CFD Re-Mesh Method

The essential aspect of the method is that the mesh in the fluid domain deforms locally around the body as it moves, and re-meshes when the mesh quality is deemed poor. The simulation information from the previous mesh is interpolated into the new mesh. The re-mesh process is summarized in the flowchart given in Figure 3A.3.

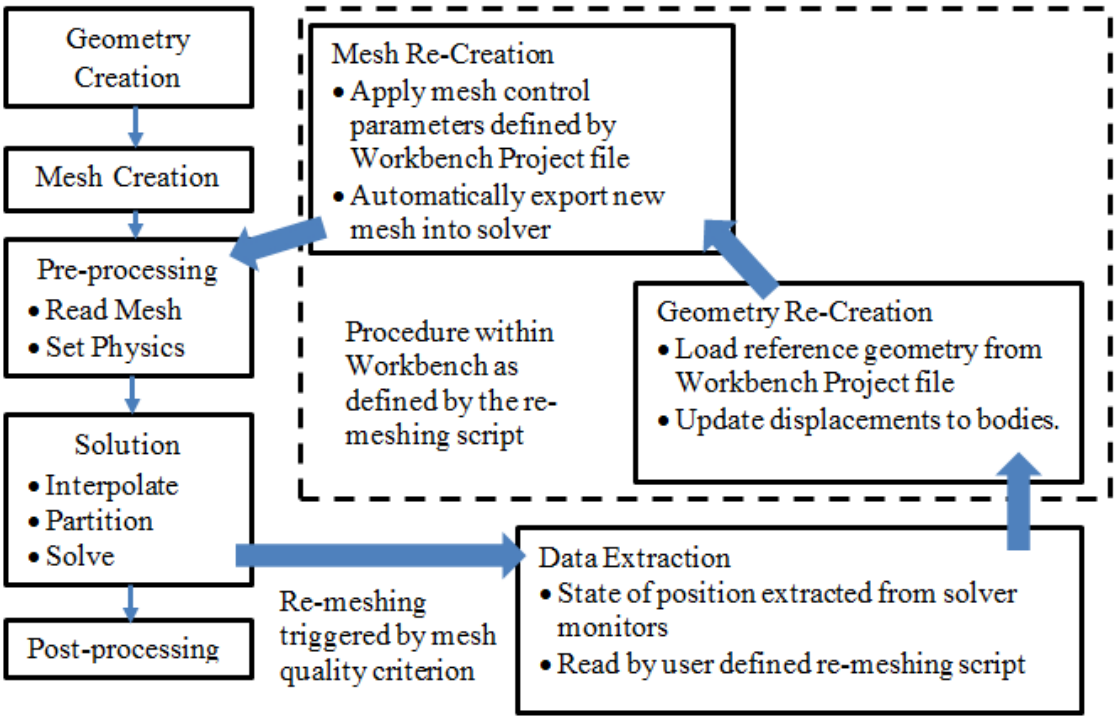

Figure 3A.3: Flowchart of the re-mesh method process.

The interrupt conditions, e.g. mesh quality below a predetermined threshold, to initiate remeshing script is defined in the solver control. The process of the remeshing script is summarized into five main parts:

- Part 1: Opens ANSYS WorkBench (WB) project component.
- Part 2: Extract monitor data from current the time step.
- Part 3: Override values of WB parameters for the geometry and mesh based on monitor data.
- Part 4: Recreate geometry and mesh.
- Part 5: Replace mesh, interpolate solution on new mesh, continue solver run.

3A.4.1.1 Limitations

The method requires separate preprocessing and meshing setups. The remeshing component is also not integrated in CFX and requires the user defined remeshing script to transfer the displacement in WB for the re-creation of the geometry and mesh.

3A.4.2 Solution Process

The solution procedure involves iterating within a time step to obtain the average force and moment conditions over the time step that result in a new predicted velocity state for the next time step.

Within a time step, the hydrodynamic variables are recomputed providing a new set of forces and moments to use in the body equations of motion. The repetition of the iterations (coefficient loops) and re-evaluation of the body state is continued until the RMS residuals in the fluid equations are reduced below a specified limit. The solution process is summarized in the flowchart shown in Figure 3A.4.

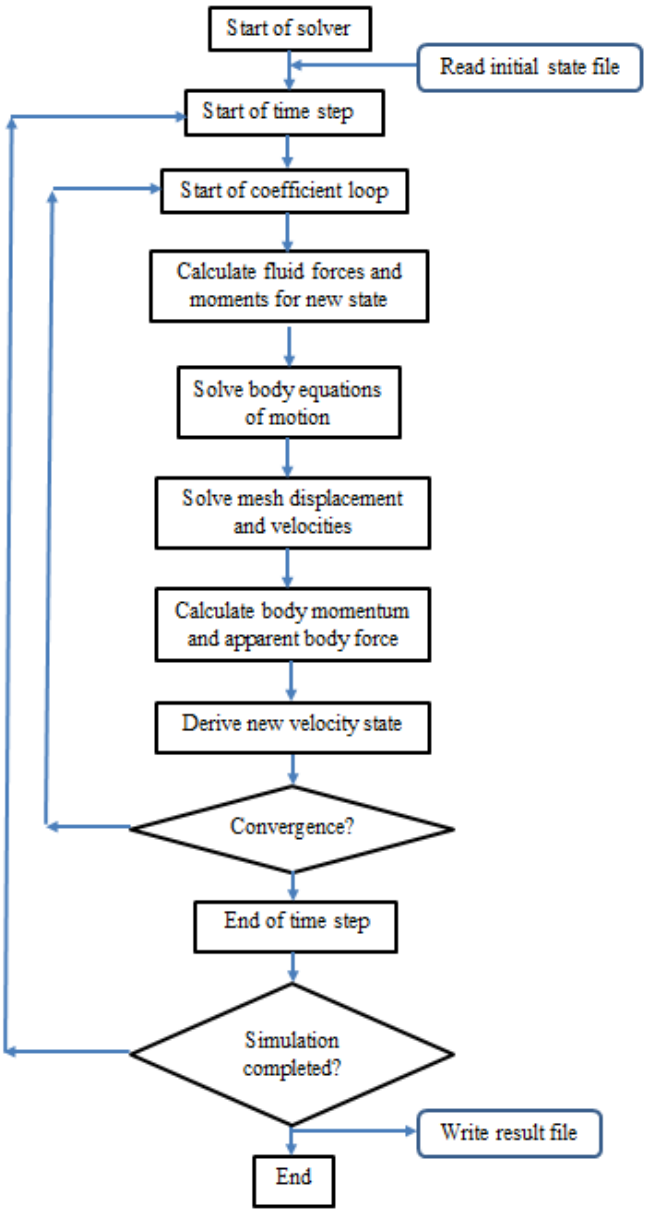

Figure 3A.4: Flowchart of the solution procedure

3A.5 Results

The current development work focused on the re-mesh method. The coupling of the fluid equations of motion with the body equations of motion as described in Section 3A.3 and Section 3A.4 will be incorporated in future work for a full 6-DOF AUV simulation manoeuvring close to a larger vessel. The simulation presented in this paper examines the accuracy of the re-mesh method to predict the flow around the bodies.

To validate the re-mesh method, two identical smooth spheres are considered as shown in Figure 3A.5. The simulation case is described below.

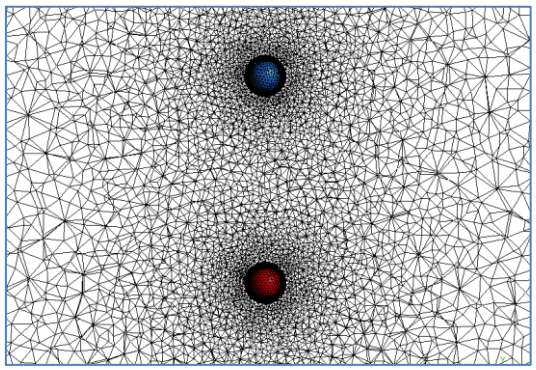

Figure 3A.5: Mesh of two spheres (re-mesh)

Simulation Case

Two spheres, Sphere 1 and Sphere 2, are to maintain position parallel to a free stream of *Re* = $1x10^4$ for 2 seconds. Sphere 2 maintains position throughout simulation to serve as a control. At simulation time, *t* = 2s, Sphere 1 moves forward in the x-direction under a prescribed acceleration, increasing at a rate of $0.179m/s^2$ per second, for 3 seconds.

Figure 3A.6 and Figure 3A.7 show the X forces on the two spheres plotted in comparison to the experimental results by Morrison (2010). As seen by the results, the general trend is well replicated. However, there are some issues in capturing certain aspects of the force curve, such as the 'dip' experienced in Morrison's curve for the moving sphere as its velocity increases and the boundary layers transits from laminar to turbulent. This will require further refinement to the mesh and the model settings.

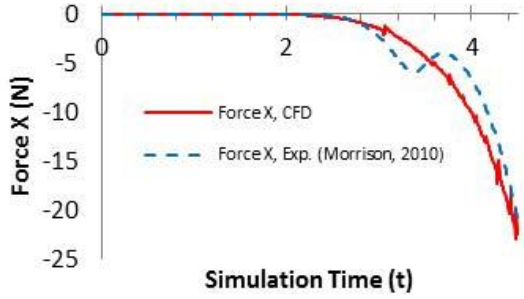

Figure 3A.6: Sphere 1 (moving) – computed force X

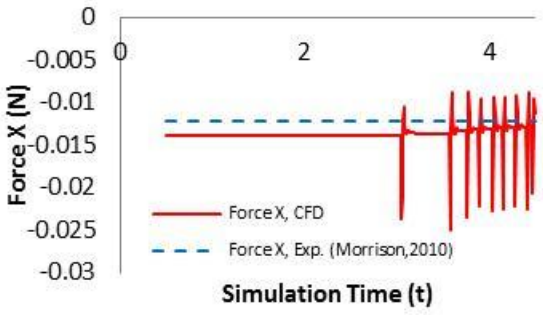

Figure 3A.7: Sphere 2 (stationary) – computed force X

The CFD forces on the stationary body in Figure 3A.7 are relatively close to the experimental results. The spike exhibited in the CFD results represents the remeshing, as the solver has to re-establish convergence.

(Note: The magnitude of the spike have been substantially reduced through improvements to the re-mesh algorithm and further reduced through a median filter in the results presented in the subsequent chapters)

3A.6 Conclusion

AUVs operating close to larger surface and submerged vessels will require simulations of both the hydrodynamic behaviour and the adaptive control system to enable proper design of the vehicle. The two components of the simulation need to be interfaced to enable the designer to understand the response of the vehicle due to the interaction between the AUV and the vessel.

The paper described the simulation of two underwater bodies moving relative to each other to provide hydrodynamic data to feed into the AUV control system simulation. Initially this consisted of two spheres; however, this will be expanded to simulate a 6-DOF AUV and a submerged moving vessel. The process employed is the remeshing method in ANSYS-CFX, which provided promising results in comparison to experimental data. This method is being improved to provide faster real time data linked to a MATLAB control environment replicating the AUV's control algorithm.

Chapter 3 :

Part B -

Numerical simulation of spheres in relative motion using dynamic meshing techniques

---

This chapter has been published in the Proceedings of the 18th Australasian Fluid Mechanics Conference. The citation for the research article is:

Leong, Z.Q., Ranmuthugala, D., Penesis, I., & Nguyen, H. 2012, 'Numerical Simulation of Spheres in Relative Motion Using Dynamic Meshing Techniques', *Proceedings of the 18th Australasian Fluid Mechanics Conference,* 3-7 December 2012, Tasmania, pp. 1-4.

Abstract

The commercial Computational Fluid Dynamics (CFD) code *ANSYS CFX* was used to simulate the flow around three dissimilar spheres in relative motion over a large range of Reynolds numbers (R_e) from 10^2 to 10^6. The simulations utilise a six degrees-of-freedom Rigid Body Dynamics (RBD) solver to predict the motion of spheres in response to external forces. The simulations were intended to provide a benchmark of the code in its ability to accurately predict the flow around multiple submerged bodies, such as submarines and unmanned underwater vehicles (UUV) in relative motion. The simulations were found to be in good agreement with both experimental data for the drag predictions and analytical solutions for the simulated motions.

Due to the large relative motions between the spheres, the CFD simulation domain undergoes significant deformation, requiring dynamic meshing techniques to maintain the integrity of the mesh and solution. A number of options including mesh deformation and adaptive remeshing, immersed solids, turbulence models, and the interface with the RBD solver were evaluated to optimise the time and resource utilisation, while maintaining acceptable accuracy and stability. The study identifies the merits of the different options to simulate multiple bodies in relative motion and provide time dependent hydrodynamic data at sufficient accuracy and speed to enable dynamic coupling with a control system for manoeuvring simulation of underwater vehicles.

3B.1 Introduction

When an UUV is operating in proximity to a larger vessel, interaction with the wake and pressure field generated by the latter can impose rapid acceleration changes on the UUV. This can cause the vehicle to undergo uncontrollable oscillations which in extreme cases can result in collision or loss of the vehicle. Therefore, it is important for designers to have a good understanding of the vehicle's behaviour under the effects of the interaction. This will enable designers to: develop control systems that are sufficiently robust enough to deal with the changes in acceleration, improve the hydrodynamic performance of the vehicle, and establish safe operating envelopes.

In general, the hydrodynamic characteristics of underwater vehicles can be evaluated and quantified through experimental and empirical methods such as captive model testing and actual vehicle trials. However, these methods require considerable cost and time, and are restricted by the availability of suitable physical models of the vehicles and appropriate test facilities. For multi-body investigations the cost can increase up to three times that for a single body due to the complexities involved in the experimental setup (Park et al. 2008).

Ongoing development of high performance computing facilities and numerical codes to predict fluid flow and pressure fields has enabled computer based simulations using CFD to replicate conditions that are difficult or costly to achieve through experimental processes. One of the major challenges faced when using CFD as an analysis tool for hydrodynamics is that computational results can vary greatly depending on the experience of the analyst, the setting utilised such as the boundary condition and the turbulence models, and the quality of the mesh grid. However, by combining both computational and experimental work, a validated simulation model could be obtained and used with confidence over the wider analysis range. This approach would be a more cost effective, faster, and viable alternative compared to one that is purely dependent on experimental work.

The flow past a sphere was chosen as a starting point for this study as there is extensive literature on its characteristics. Most numerical investigations on fluid flow around a sphere have been focused on using higher order schemes such as *Large Eddy Simulation* (LES) and *Direct Numerical Simulation* (DNS). These schemes have produced high quality and accurate

predictions of the wake structure, shedding frequencies, and forces associated with a flow within a R_e range between 10^2 and 10^6 (Jones & Clarke 2008; Beratlis et al. 2012). Despite extensive numerical studies on sphere hydrodynamics, there appears to be limited work using *Reynolds-Averaged Navier-Stokes* (RANS) simulations.

In RANS simulation, all scales of turbulence are modelled and the transport equations are represented in mean flow quantities. Although, this approach is less accurate for time dependent flow phenomena, e.g. vortex shedding, it offers a viable means to obtain reasonably accurate hydrodynamic forces acting on a submerged body in motion at greatly reduced computational effort. The reduction in mesh requirements for RANS simulation can be up to 10^3 orders of magnitude compared to an LES mesh of ~10^9 cells for equivalent accuracy (Menter 2012). In addition, the required time step for stability in RANS is determined by the fluctuation in the mean flow rather than turbulence. This allows RANS simulation to be carried out at time step of up to 100 times coarser than LES, especially for transient simulation with turbulent flows.

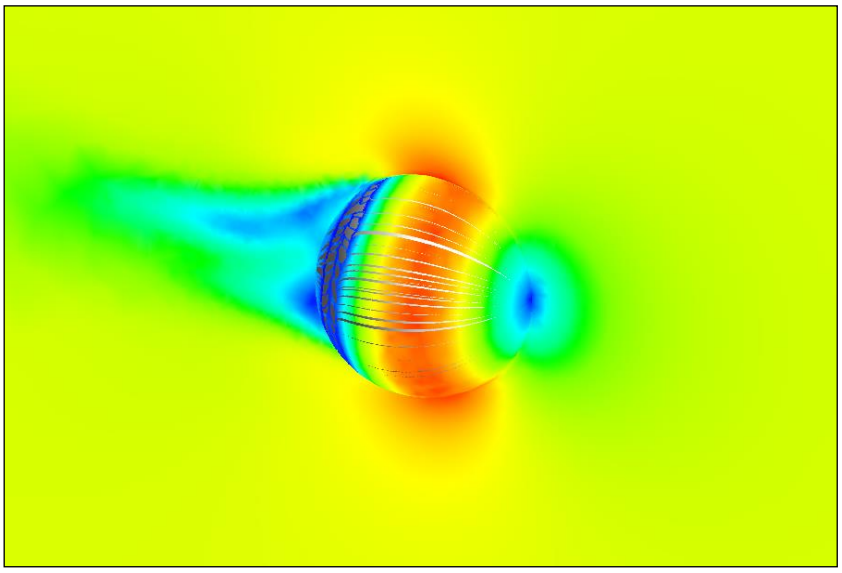

Figure 3B.1: CFD visualisation of the velocity field and streamlines around a sphere in motion.

In this study, two dynamic mesh techniques, Mesh Deformation and Adaptive Remeshing Method (MDARM) and Immersed Solid Method (ISM) are evaluated in terms of accuracy and computational speed for modelling fluid flow around a single smooth sphere in motion over a R_e range of 10^2 to 10^6. The MDARM simulations (see Figure 3B.1) were carried out

with the *Shear Stress Transport k-omega* (SST) and *Baseline Reynolds Stress Model* (BSLRSM) turbulences models in addition to a laminar flow model providing a baseline for computational speed comparison. The ISM simulations were carried out with the SST model. The computational results were compared to experimental data to benchmark their accuracy. Coupled simulations of the flow and RBD solvers were also carried out to investigate the accuracy of the motion predictions compared to analytical solutions for three spheres in relative motion. The aim of the study was to establish which combination of turbulence model and dynamic meshing technique offered an efficient trade-off between accuracy and computational speed.

3B.2 Numerical Model

3B.2.1 Single Sphere Model

The three-dimensional (3D) computational domain is presented in Figure 3B.2. The size of the domain was 10m long, 2m wide and 2m deep. The diameter of the sphere was 0.1m. The sphere was located at an initial position 2m forward of the Outlet boundary and 1m away from the Farfield boundaries to ensure the pressure field generated by the sphere was well within the computational domain.

The MDARM simulations were carried out on an unstructured mesh containing 5.9×10^5 cells, made up of tetrahedrons in the regions away from the sphere and prisms around the sphere to capture the boundary layer as shown in Figure 3B.3. The sphere resides in a subdomain which allows the mesh within subdomain to be rigid, with deformation occurring only in the outer fluid domain. The mesh was progressively refined by subdividing the cells of the sphere surface and subdomain to examine the sensitivity of the drag predictions to the mesh density. At 7×10^6 cells, the variation in the predicted mean drag of the sphere was 6% compared to the 5.9×10^5 mesh cells model with the SST model at $R_e = 10^6$. Therefore, the latter mesh model was deemed sufficiently mesh independent with an uncertainty of 12% (2×6%). Further refining the mesh would result in the simulations being too expensive for coupling with a control system, as a smaller time step is required for smaller cells in order to satisfy the *Courant-Friedrichs-Lewy* (CFL) numbers of below 10 across the domain.

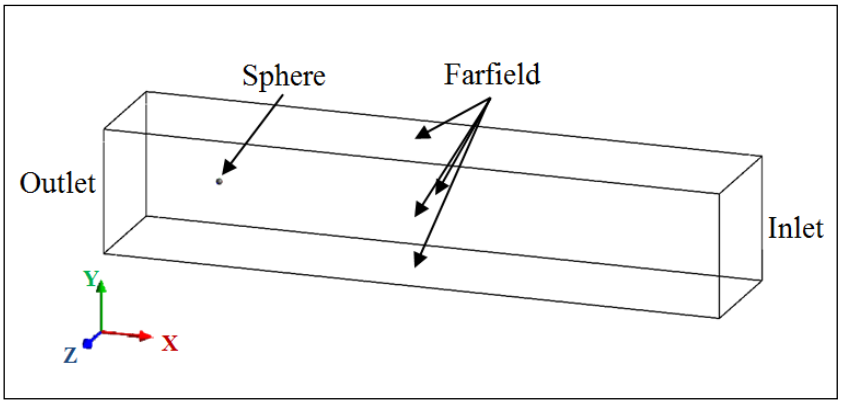

Figure 3B.2: The single sphere computational domain.

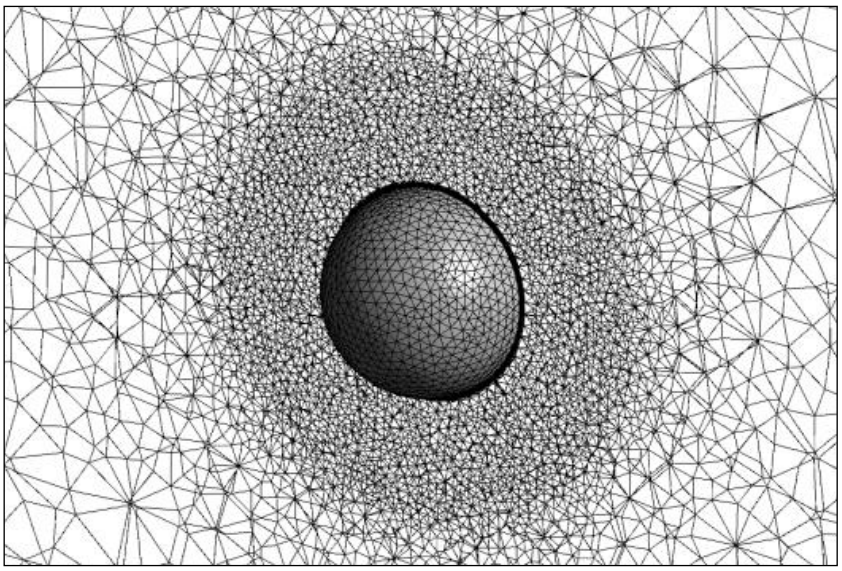

Figure 3B.3: The MDARM mesh model.

For the evaluation of the ISMs simulations, the mesh for the sphere and fluid domain were individually generated and then overset as shown in Figure 3B.4. The mesh model of the sphere consists of the inner volume which requires only good mesh resolution on the sphere surface, e.g. mesh surface area error of less than 1%. The volume mesh inside the sphere may be arbitrarily coarse. The fluid mesh cells in which the sphere travels were refined to half the sphere surface mesh size to ensure two fluid domain nodes to every sphere domain node exist at the boundaries where the two domains intersect. This is required to ensure stability and smooth interpolation between the nodes of the fluid domain and the sphere. The result is a mesh model of approximately 7×10^6 cells.

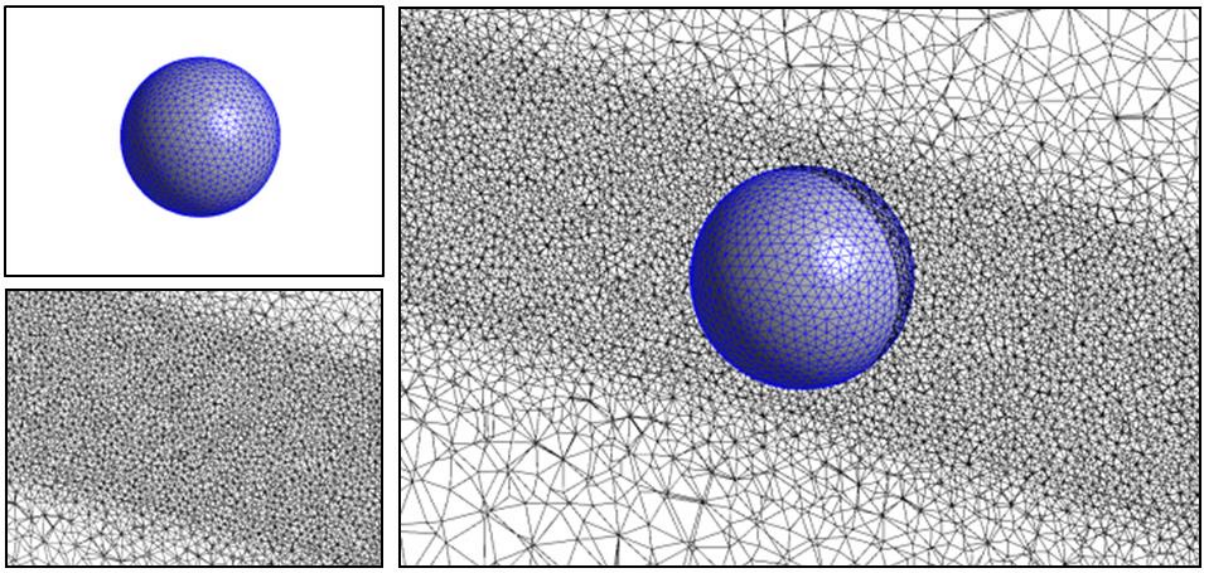

Figure 3B.4: The ISM mesh model; sphere mesh (upper left), fluid domain mesh (bottom left).

3B.2.2 Two Spheres Model

Two spheres with a diameter 0.1m were located within a computational domain size of 3m long, 2m wide, and 12m deep as shown in Figure 3B.5. The initial locations of the spheres were at z = -10m, 1m apart from each other, and 1m away from the Farfield boundaries. The mesh setup of the spheres was identical to the single sphere MDARM model. The mesh size was approximately 1.2×10^6 cells.

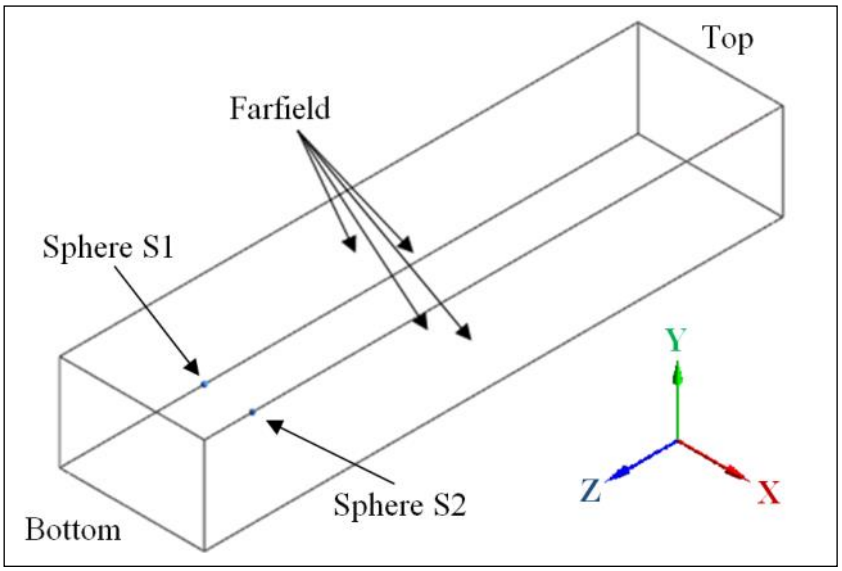

Figure 3B.5: The two spheres computational domain.

3B.3 Numerical Simulation

The simulations were performed using the CFD code *ANSYS CFX v14*, which uses a control volume based finite element discretisation scheme. A time step between 0.1ms-1ms was used throughout the simulations in order to provide reasonably good time resolution of the forces and motions while maintaining CFL numbers of below 10 in the majority of the computational domain. The density and kinematic viscosity of the fluid were $997 kg/m^{-3}$ and $8.899 \times 10^{-4} m^2/s$ respectively.

3B.3.1 Single Sphere Simulations

The essential aspect of the MDARM is that the mesh in the fluid domain deforms locally around the sphere as it moves and remeshes when the mesh quality is deemed compromised in terms of accuracy and stability. This overcomes the limited motions imposed by using a pure mesh deformation approach. Although mesh deformation is fully supported in *ANSYS CFX*, the remeshing component is a *beta* feature and requires the use of a user-defined script. The latter, triggered by the mesh quality criterion, interrupts the simulation and transfers the positional state of the sphere into *ANSYS Workbench* in order to update the geometry and the mesh. The script then transfers the new mesh into the solver where the simulation information from the previous mesh is interpolated into the new mesh and the simulation is resumed. The mesh quality criterion was defined as the orthogonality angle in the mesh cells of no less than 10°.

For the ISM simulations, the sphere is defined as an immersed solid. As the sphere moves within the fluid domain, the velocity of the fluid nodes is enforced to be same as the velocity of the sphere by applying a set of source terms in the regions where the sphere mesh overlaps the fluid domain mesh. This method essentially avoids any mesh deformation, therefore remeshing is not required. The simulations were carried out with the SST turbulence model to model the turbulence in the freestream and the regions affected by the pressure field of the sphere. The ISM method does not resolve the boundary layer due to the inability to apply a wall treatment on the surface of the sphere.

3B.3.2 Two Spheres Motion Response Simulations

For the motion response simulation, the flow solver was coupled with the RBD solver using the MDARM for modelling the relative motion between spheres. The spheres were submerged at an initial depth of 10m and were allowed to rise up freely. Different mass values were defined for each of the spheres, with the motion of each sphere dictated by the net force of its weight and buoyancy. The properties of the spheres are outlined in table 1.

Table 3B.1: Properties of the spheres for the motion response simulation.

Sphere	**S1**	**S2**
Mass, *m* [kg]	4.568E-1	3.915E-1

3B.4 Results and Discussion

3B.4.1 Single Sphere Results

Figure 3B.6 shows the mean drag coefficient (C_D) predictions of the MDARM simulations with SST, BSLRSM and Laminar model and the ISM simulations with SST against the experimental results by Schlichting (1979).

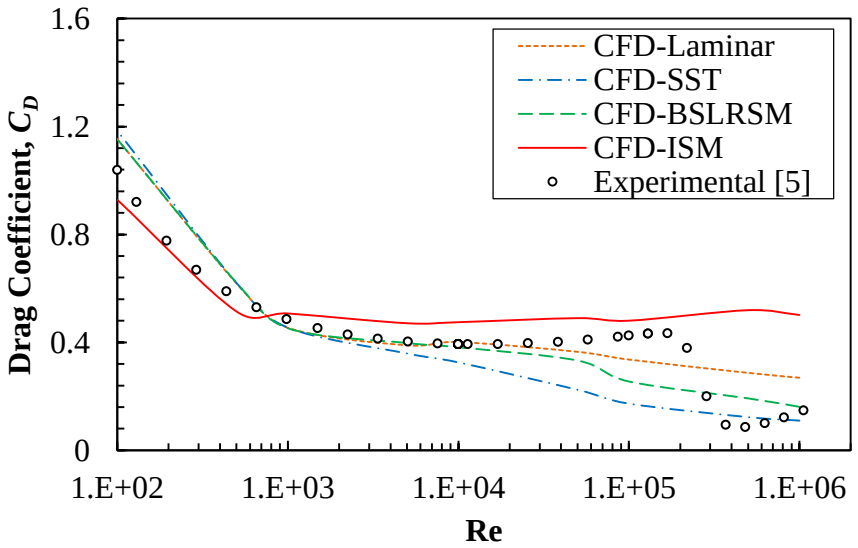

Figure 3B.6: Mean drag coefficient of the single smooth sphere as a function of R_e.

At $R_e < 10^3$, where the flow around the sphere is below the turbulence wake regime, the ISM and the MDARM predictions compares favourably with the experimental results. The

predictions of the MDARM-SST model and MDARM-BSLRSM were within 5% of the Laminar model. Although this is counterintuitive when turbulence models are applied for laminar flow since the boundary layer is modelled to be fully turbulent, the SST and BSLRSM are able to handle very small turbulence kinetic energy in the flow field thus able to give similar predictions to the Laminar model within the regime.

At $10^3 < R_e < 10^4$, the wake behind the sphere changes from laminar to turbulent, while its boundary layer remains laminar. The drag predictions of all models were in good agreement as shown in Figure 3B.6. At $R_e = 10^4$, the MDARM-SST model increasingly underpredicts the sphere drag as *Re* increases. The same was observed for the MDARM-BSLRSM drag predictions at $R_e \sim 6\times10^4$ onwards. This is possibly due to the models overpredicting the turbulence kinetic energy in the sphere boundary layer thus pushing its separation further back. The predictions of MDARM-Laminar model and the ISM-SST model were found to be in good agreement with experimental results. It is noted that the predicted mean drag coefficient by the ISM-SST model remains around 0.5 as R_e increases thereafter.

At $10^5 < R_e < 10^6$, the flow in sphere boundary layer transitions from laminar to turbulent causing a sudden drop in drag which is commonly referred as the 'drag crisis'. None of the models were able capture the drag crisis characteristics. This was expected as none of the models were designed for transitional flows. However, the MDARM used with turbulence models were able to exhibit a gradual decline in drag within the regime and gave good predictions when the flow was fully turbulent at $R_e = 10^6$. Both the MDARM-Laminar and ISM-SST models were unable to accurately predict the drag on the sphere for turbulent boundary layer dependent flow.

The MDARM simulations were carried out with 6 core processers, and the ISM simulations 16 core processers due to its high mesh density. Table 2 outlines the computational effort of the simulations at $R_e = 10^6$. The time for each remeshing event in the MDARM simulations was approximately 50 seconds. Although the MDARM-Laminar required the least computational effort, the model was insufficiently accurate for flow speeds where turbulence is prevalent. The MDARM-BSLRSM drag prediction was the most accurate, 11% closer to experimental results compared to MDARM-SST, however, the former required 42% more computation effort. Therefore, the MDARM-SST model was reasoned to be the most

efficient in terms of accuracy and computational speed. The ISM was the most computational expensive option in both mesh requirement and computational time. Although the ISM does not require remeshing, the advantage was offset by the fine mesh required in regions where the sphere travels to maintain simulation stability resulting in a substantial increase in mesh density. The ISM is more suited for simulations of bodies undergoing localised rotational motion or medium displacement.

Table 3B.2: Computational effort of the simulations at $R_e = 10^6$.

Model	Mesh cells	Time per inner loop [s]	Effort compared to MDARM-Laminar
MDARM-Laminar	6×10^5	24	1.00
MDARM-SST	6×10^5	29	1.20
MDARM-BSLRSM	6×10^5	41	1.70
ISM-SST	7×10^6	400	194

3B.4.2 Two Spheres Results

The simulation results for the linear acceleration of the spheres, were found to be in good agreement with the analytical solution, $\ddot{z}_a$, which was based on Newton's second law of motion,. The simulation result for the linear acceleration of S1 was 0.866m/s^2 while the analytical result was 0.892m/s^2, giving an error of 3%. For S2, the simulation result was 1.803m/s^2 with the analytical result being 1.962m/s^2, giving an error of 8%.

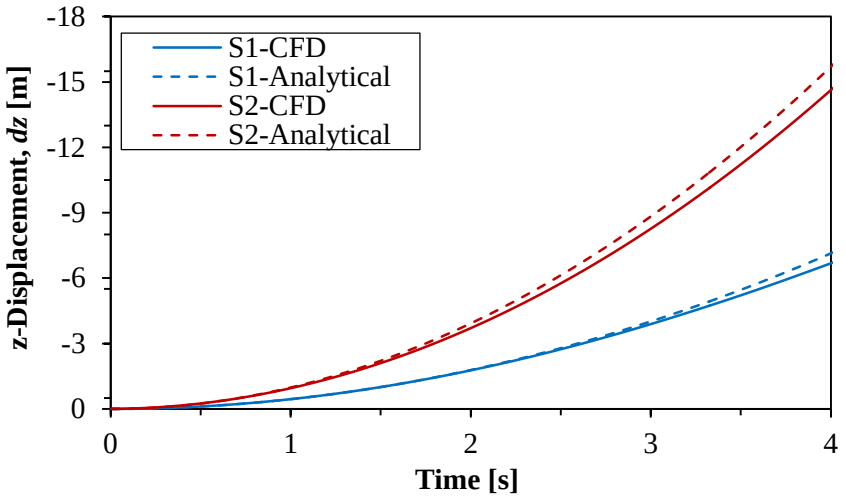

Figure 3B.7: The *z*-displacements of the two spheres.

Figure 3B.7 shows the simulation results for the *z*-displacement of the two spheres plotted in comparison to the analytical results. The analytical results were obtained by twice integrating $\ddot{z}_a$ with respect to time. The simulation results underpredicted the motions compared to the analytical results but were within 10% of the latter. This was considered acceptable as the analytical results did not take into account the fluid drag acting on the spheres.

3B.5 Conclusion

The present work is directed towards developing a simulation environment of an underwater vehicle manoeuvring in relative motion to a larger vessel, with the extensibility for coupling with the vehicle's control system. The simulation model needs to provide time dependent hydrodynamic data of reasonable accuracy and sufficient speed to enable efficient coupling with the control system for manoeuvring simulations of underwater vehicles.

The performance of RANS-based simulations with and without turbulence models, coupled with the dynamic mesh techniques, to simulate the fluid flow around a sphere undergoing large displacements within $10^2 < R_e < 10^6$ were examined. The MDARM-SST model was the most efficient in terms accuracy and computational speed with the drag predictions of the model being in good agreement with experimental data, except for within the flow regime where the sphere boundary layer changes from laminar to turbulence. The MDARM-BSLRSM predictions were 11% closer to experiment at fully turbulent flow at $R_e = 10^6$ compared to the SST model but took 42% more computational time.

The MDARM was found to be far superior for modelling bodies with large displacement compared to the ISM in both accuracy and computational effort. Although the ISM does not require remeshing or a mesh to resolve the boundary layer around each body, it still requires a fine mesh in the fluid domain regions where the body travels. This fine mesh increases substantially with the motion range thus also increasing computational time. In addition, the inability of the ISM to model the boundary layer accurately has shown to give poor drag predictions at higher flow speeds. The motion predictions of the coupled flow solver and RBD solver simulations for two spheres in relative motion were found to be in good agreement to analytical solutions.

Currently, work is being carried out to model a 6-DOF UUV and a larger submerged vessel in relative motion, which requires simulation of the vehicle's hydrodynamic behaviour close to the larger vessel. The simulation model is also being improved to provide faster real time data linked to a MATLAB-based control environment replicating the UUV's control algorithm. In conjunction with the numerical work, experimental model tests are being carried out to validate the capability of the simulation to predict the hydrodynamic interaction between the UUV and the larger vessel.

[Page intentionally left blank]

Chapter 4 :

Investigation into the Hydrodynamic Interaction Effects on an AUV Operating Close to a Submarine

This chapter has been published in the Proceedings of the Pacific 2013 International Maritime Conference. The citation for the research article is:

Leong, Z.Q., Saad, K.A.M., Ranmuthugala, D., & Duffy, J. 2013, 'Investigation into the Hydrodynamic Interaction Effects on an AUV Operating Close to a Submarine', *Proceedings of the Pacific 2013 International Maritime Conference*, 7-9 October 2013, Darling Harbour, Australia, pp. 1-11.

Chapter 5 :

Scaling and Relative Size Effects on The Hydrodynamic Interaction on an UUV Operating Close to a Submarine

This chapter has been published in the Proceedings of the Warship 2014: Naval Submarines & UUVs Conference. The citation for the research article is:

Leong, Z.Q., Ranmuthugala, D., Penesis, I., & Nguyen, H. 2014, 'Scaling and Relative Size Effects on the Hydrodynamic Interaction on an UUV Operating Close to a Submarine', *Proceedings of the Warship 2014: Naval Submarines & UUVs Conference*, 18-19 June 2014, Bath, United Kingdom, pp. 105-114.

Chapter 6 :

Quasi-static analysis of the hydrodynamic interaction effects on an autonomous underwater vehicle operating in proximity to a moving submarine

---

This chapter has been submitted for publication in the Journal of Engineering and at the time of writing is under review. The citation for the research article is:

Leong, Z.Q., Ranmuthugala, D., Penesis, I., & Nguyen, H. 2014, 'Quasi-Static Analysis of the Hydrodynamic Interaction Effects on an Autonomous Underwater Vehicle Operating in Proximity to a Moving Submarine', *Journal of Ocean Engineering*. [Under review, 2014].

Abstract

When an Autonomous Underwater Vehicle (AUV) operates close to a submarine, interaction with the flow and pressure fields of the submarine can adversely affect the motion of the AUV. These interactions can result in uncontrollable motions of the AUV, which in extreme cases can lead to mission failure due to the inability of the AUV to maintain the desired trajectory or from collision with the submarine. This paper outlines the steady-state interaction forces and moments acting on the AUV at different fixed speeds and relative positions to the submarine, with an aim to identify the regions where adverse effects due to interaction are minimal. The results presented in this paper are from a series of model scale and full-scale Computational Fluid Dynamics (CFD) simulations on axisymmetric AUV and submarine models at diameter ratios between the two vehicles models of 2.239, 5.723 and 14.634. Validation was carried out for the lower diameter ratio at model scale using captive model experiments. Results show that the adverse effects of the interaction forces and moments were minimal when the AUV's centre of buoyancy is around amidships of the submarine, providing a relatively safe operating path for the AUV.

6.1 Introduction

The increasing capabilities of Autonomous Underwater Vehicles (AUVs) have resulted in greater usage of AUVs within both the civilian and the defence sectors in potentially hazardous environments for long periods of time with no real-time user intervention. One such area is the operation of an AUV in close proximity to a moving submarine, requiring the AUV to safely negotiate the hydrodynamic interaction effects between the two vessels. These interaction effects are of particular interest to submarine and AUV designers as navies around the world begin to equip their submarine fleets with the capability to launch, retrieve and recharge AUVs, in addition to the ability to communicate data between them during operations (Rodgers et al. 2008; Hardy & Barlow 2008; DARPA 2013). Currently, there is very little information with regard to this in the public domain.

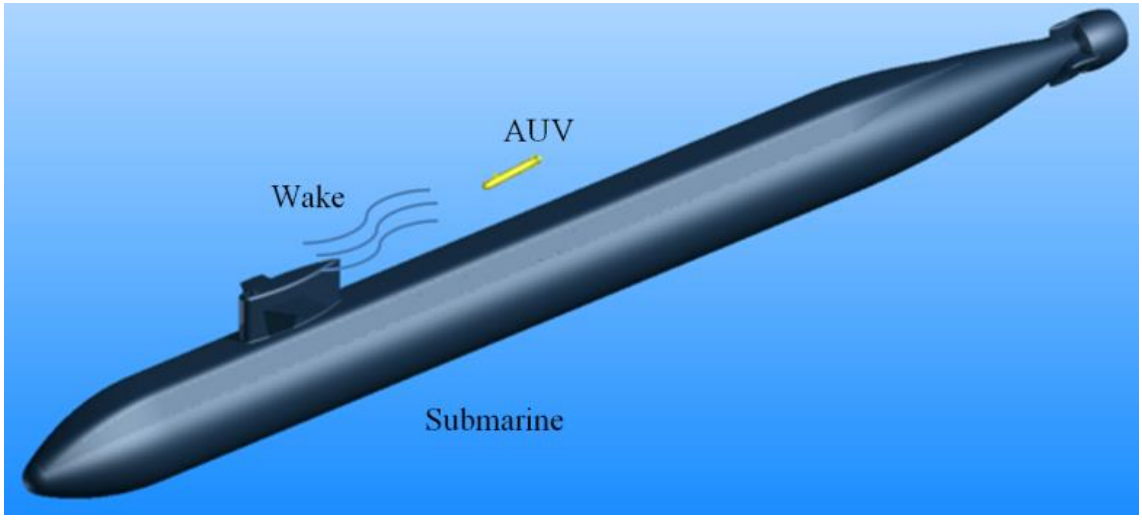

Figure 6.1: An AUV moving in the wake of a submarine.

When an AUV is operating close to a moving submarine (see Figure 6.1), interaction with the submarine's wake and pressure fields can impose unwanted forces and moments on the AUV. These interaction effects can cause the AUV to undergo uncontrollable motions which can result in mission failure due to the vehicle's inability to maintain its desired trajectory and in extreme cases lead to collision with the submarine, resulting in the damage or destruction of the AUV and possible damage to the submarine appendages or sensors (Byrne 1998). Since the AUV is relatively small compared to the submarine, it would be the principle vessel adversely affected by the interaction. Thus, designers need to have a good understanding of the hydrodynamic interaction between the two vehicles in order to develop AUV control

systems that can ensure vehicle stability and identify operating parameters in which an AUV can effectively manoeuvre near a submarine.

A recent study was carried out numerically by Byrne (1998), based on a real-time manoeuvring simulator developed by Brutzman (1994) to evaluate the manoeuvring and control performance of an AUV in response to steady-state ocean currents. Byrne (1998) attempted to extend the simulator capabilities to include flow forces induced by an adjacent submarine. The aim of the simulation was to evaluate the manoeuvring and control performance of the Phoenix AUV undertaking a docking operation with a 688-class submarine via a retractable recovery tube located at the front end of the submarine parallel midsection. The hydrodynamic interaction between the two vessels was included in a module which is based on Ludwig Prandtl's classical boundary layer theory for a flat-plate. The module introduced a parabolic flow velocity profile along the submarine hull in order to represent the reduced flow velocity encountered by the AUV as it approached the boundary layer of the submarine. However, this is an over-simplification of the interaction effects, as it did not account for operational issues associated with the submarine wake effects and the more dominant potential field effects generated by the submarine which can either repel or attract the AUV depending on their relative positions.

Using steady-state Computational Fluid Dynamics (CFD) simulations, Fedor (2009) investigated the hydrodynamic interaction effects on an AUV at a fixed position relative to the sail of a moving submarine. The aim of the study was to establish a feasible region to launch and recover the vehicle around the submarine. It was found that in the forward region of the sail the interaction acts to repel the underwater vehicle, with the repelling force increasing as the vehicle gets closer to the submarine. General trends were less observable in the regions to the side and astern of the sail, where the direction of the force and moments acting on the vehicle fluctuate due to the horseshoe vortices generated by the sail. Since the investigation focused on locations very close to the submarine, the parameters surrounding the broader extent of the interaction effects and the means for the AUV to approach the regions were not discussed.

To date, there have been very few experimental studies investigating the hydrodynamic interaction between two submerged vessels. The studies by Byrne (1998) and Fedor (2009) offer an insight into the interaction effects acting on an AUV operating within the proximity

of a larger moving underwater vessel. However, they both state that their results were based purely on numerical work, requiring adequate validation.

For experimental methods, the hydrodynamic characteristics of AUVs can be evaluated and quantified through captive model testing or in-water testing of the actual vehicle. However, these methods require considerable cost and time, and the requisite of a physical model of the vehicle and suitable test facilities. For multi-vehicle investigations, the cost can increase substantially for each additional vehicle involved due to complexities in the test setup, in particular for an AUV operating within the proximity of a larger moving underwater vessel. As such, the hydrodynamic interaction effects between submerged vehicles have not been extensively investigated experimentally. Nevertheless, some parallels can be drawn from experimental studies on the hydrodynamic interactions between surface ships, deducing that the interaction effects will depend on the: relative size between the submerged vessels, lateral separation distance, longitudinal relative positions, vessel speeds, hull shapes, submerged depths, and water depth (Taylor 1909; Newman 1960; Remrey 1974; Kyulevcheliev & Varyani. 2004; Kribel 2005, Lataire et al. 2012).

This paper presents the hydrodynamic interaction effects on an AUV operating in close proximity to a larger moving submarine, obtained through CFD modelling to quantify the surge force, sway force, and yaw moment acting on the AUV at different lateral and longitudinal positions relative to the submarine. In order to examine the influence of relative size between the two vessels, three AUV models were used giving diameter ratios (i.e. submarine diameter to AUV diameter, $D_{\text{Explorer}}/D_{\text{SUBOFF}}$ in Figure 6.1) of 2.239, 5.723, and 14.634, with the latter closely representing a typical AUV and a conventional submarine. Experimental Fluid Dynamics (EFD) involving captive-model tests of the two vehicles at a diameter ratio of 2.239 were carried out to validate and supplement the CFD simulations. The results assisted in identifying the adverse interaction regions around the submarine and a safe path for the AUV to approach and depart the former. In addition, the resulting map of interaction forces and moments is intended to be used in a dynamic manoeuvring simulation to evaluate the motion behaviour of the AUV and develop the necessary algorithms to maintain the desired trajectory of the vehicle when in operation near a moving submarine.

6.2 Investigation Programme

The interaction between the two underwater vessels was investigated through CFD and EFD work for the diameter ratio of 2.239 and through CFD for the diameter ratios of 5.723 and 14.634, at different longitudinal and lateral distances over a range of speeds. The smaller AUV was represented by the axisymmetric SUBOFF hull form (Groves et al. 1989) developed by the Defence Advanced Research Projects Agency (DARPA), while the larger body representing the submarine was based on the International Submarine Engineer Ltd. designed Explorer vehicle (ISE 2005).

Figure 6.2 shows the two geometries, with the principal dimensions, relative longitudinal distance, and relative lateral distance defined. The length to diameter ratios of the SUBOFF and Explorer are 8.575 and 7.243 respectively. The relative lateral distance x_{distance} and relative longitudinal distance y_{distance} are measured from the centre of buoyancy *CB* of the larger vessel to that of the smaller vessel. For x_{distance} a 'positive' distance signifies that the SUBOFF is located in front of the *CB* of the larger vessel. For the remainder of this paper, the longitudinal and lateral distances are referred to as non-dimensionalised ratios R_{Long} and R_{Lat}, i.e.,

$$R_{\text{Long}} = \frac{x_{\text{distance}}}{L_{\text{Explorer}}} \tag{6.1}$$

$$R_{\text{Lat}} = \frac{y_{\text{distance}}}{L_{\text{Explorer}}} \tag{6.2}$$

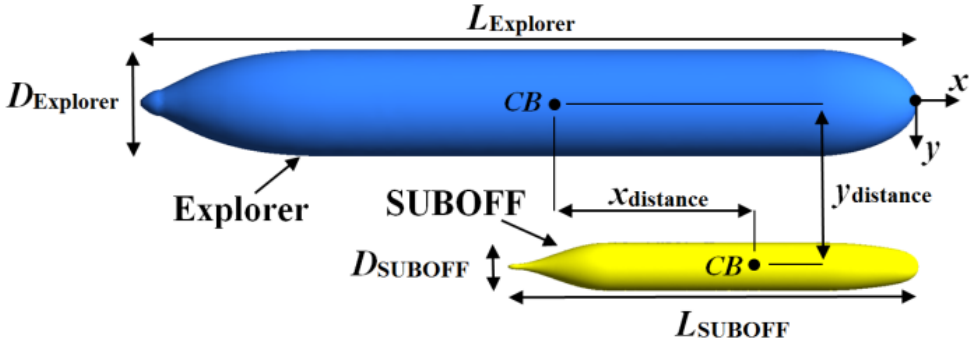

Figure 6.2: Definition of the model parameters.

The influence of relative size on the interactions was examined as function of diameter ratio through CFD. The three diameter ratios of 2.239, 5.723 and 14.634 were achieved by scaling the SUBOFF to a diameter of 3.484m, 1.363m and 0.533m respectively, while maintaining the diameter of the Explorer at 7.8m. The variables investigated included the length-based coefficients of the drag force, sway force, and the yaw moment acting on the SUBOFF geometry, with the latter calculated at a reference point located at $0.462L_{SUBOFF}$ aft of the SUBOFF geometry nose tip.

Table 6.1: Vessel dimensions and test parameters.

Diameter Ratio	Parameter	SUBOFF	Explorer	
Full-scale				
($-3.00 \leq R_{Long} \leq 3.00$, $0.21 \leq R_{Lat} \leq 2.45$)				
2.239	Length, L	29.875	56.795	[m]
	Diameter, D	3.484	7.800	[m]
	Displacement, ∇	2.255×10^{2}	2.309×10^{3}	[m^3]
	Forward speed, U	7.75×10^{-2}, 0.75, 1.50, 3.00	7.75×10^{-2}, 0.75, 1.50, 3.00	[$m\ s^{-1}$]
	Reynolds Number, Re	2.61×10^{6}, 2.51×10^{7}, 5.02×10^{7}, 1.00×10^{8}	4.93×10^{6}, 4.75×10^{7}, 9.49×10^{7}, 1.90×10^{8}	[-]
5.723	Length, L	11.685	56.795	[m]
	Diameter, D	1.363	7.800	[m]
	Displacement, ∇	1.350×10^{1}	2.309×10^{3}	[m^3]
	Forward speed, U	1.50	1.50	[$m\ s^{-1}$]
	Reynolds Number, Re	1.96×10^{7}	9.49×10^{7}	[-]
14.634	Length, L	4.570	56.795	[m]
	Diameter, D	0.533	7.800	[m]
	Displacement, ∇	8.075×10^{-1}	2.309×10^{3}	[m^3]
	Forward speed, U	1.50	1.50	[$m\ s^{-1}$]
	Reynolds Number, Re	7.68×10^{6}	9.49×10^{7}	[-]
Model Scale				
($-0.62 \leq R_{Long} \leq 0.92$, $0.21 \leq R_{Lat} \leq 0.29$)				
2.239	Length, L	1.552	2.935	[m]
	Diameter, D	0.181	0.405	[m]
	Displacement, ∇	3.162×10^{-2}	3.237×10^{-1}	[m^3]
	Forward speed, U	0.75, 1.50	0.75, 1.50	[$m\ s^{-1}$]
	Reynolds Number, *Re*	1.30×10^{6}, 2.61×10^{6}	2.47×10^{6}, 4.93×10^{6}	[-]

In order to supplement and establish the credibility of the CFD predictions, a series of captive-model experiments was carried out for the diameter ratio of 2.239. Since the larger vessel had a more dominant pressure field in the interaction compared to the smaller vessel, the length of the Explorer was used as the characteristic length scale for dynamic similarity between the model scale and full-scale parameters. Table 6.1 summarises the test parameters and vehicle model dimensions.

6.3 Simulation Setup

The simulations were performed with ANSYS CFX, a commercial CFD code. The Reynolds Averaged Navier-Stokes (RANS) -based Baseline Reynolds Stress Model (BSLRSM) was utilised in this analysis using a steady-state approach to the solutions. Previous CFD and EFD work by the authors on underwater vehicles of similar geometry to the SUBOFF (Leong et al. 2014a), showed that the BSLRSM was more accurate in predicting the forces and moments acting on vehicles. This was due to its more comprehensive modelling of rotational flow, flow separation, and flows that are strongly anisotropic in comparison to RANS-based eddy-viscosity models.

Figure 6.3 shows the computational fluid domain in a fixed frame of reference, with its centre of origin located at the centre of buoyancy of the Explorer (CB_{Explorer}). The far field boundaries were kept six body lengths away from the CB_{Explorer}, with the exception of the outlet which was kept eight body lengths away, to ensure that boundaries had no blockage effect on flow around the vehicles and the wake of the vehicles were sufficiently resolved within the domain. The flow at the inlet was prescribed to match the desired vehicle speed while the outlet was set as an opening with zero relative pressure. The surfaces of the vehicles were prescribed as no-slip walls, while the remaining boundaries were set as free-slip walls.

The fluid domain was divided into three parts: two subdomains for each of the regions around the Explorer and SUBOFF, and an outer domain for the remaining region. The division of the domain allowed each part to be meshed and refined individually. This also allowed for easier changes in location and configuration for each vehicle without remeshing the entire domain. To ensure continuity throughout the domain, the separate parts were connected together using

the General Grid Interface (GGI) functionality in ANSYS CFX utilising similar mesh sizes at the interface surfaces.

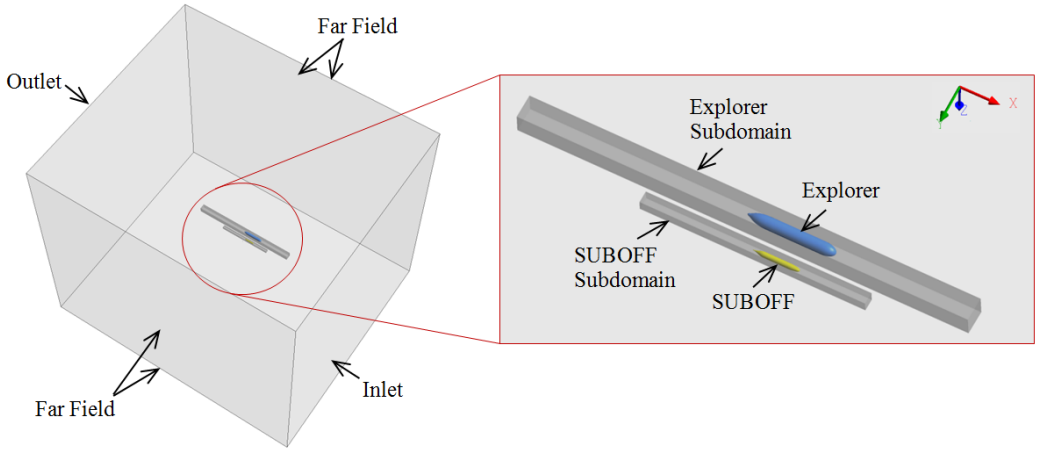

Figure 6.3: Computation fluid domain.

For the discretisation of the fluid domain, an unstructured mesh approach was used, i.e. triangular prismatic inflation layers around the SUBOFF to capture the boundary layer and unstructured tetrahedrons in the far field. An unstructured mesh approach was selected due to its ability to easily accommodate mesh deformation and automatic remeshing, features that will be required when future simulations of multiple vehicles in relative motion are carried out. A well thought out unstructured mesh, although requiring a higher mesh density, offers the same degree of accuracy in comparison to a structured mesh (Duda 2011).

6.4 Experimental Work

For the interaction test programme, the experimental data was based on previous work carried out by the authors (Leong et al. 2013), which were conducted in the Australian Maritime College (AMC) Towing Tank. The 100 × 3.5 × 1.5 m^3 tank is equipped with a manned variable speed carriage and a wave generator, and uses a Horizontal Planar Motion Mechanism (HPMM) capable of generating horizontal motion on an underwater vehicle model, and recording the resulting forces and moments.

The SUBOFF model was mounted to the HPMM using a ‘sting’ arrangement that connects to the model through the aft end, with the forces acting on the SUBOFF model recorded using two 6-Degree of Freedom (6-DOF) load cells located inside the model as shown in Figure

6.5. The Explorer model was mounted directly onto the carriage by means of a rigid beam construction as shown in Figure 6.4, with no forces recorded, as the objective of the work was to investigate the behaviour of the smaller vehicle due to the interaction. The R_{Lat} between the two models was adjusted by shifting the lateral position of the SUBOFF using the HPMM, while the R_{Long} was adjusted by shifting the longitudinal position of the Explorer along the support beam. Both models were fully flooded and located mid-depth of the tank.

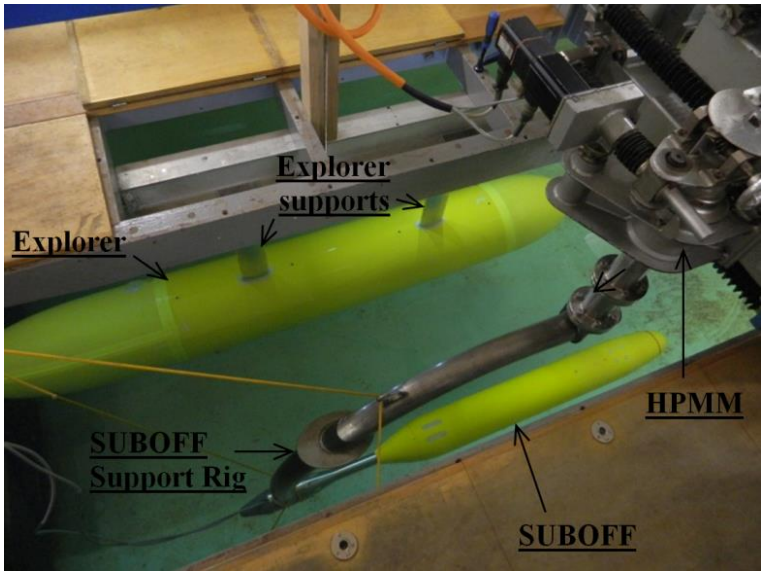

Figure 6.4: Experimental testing rig.

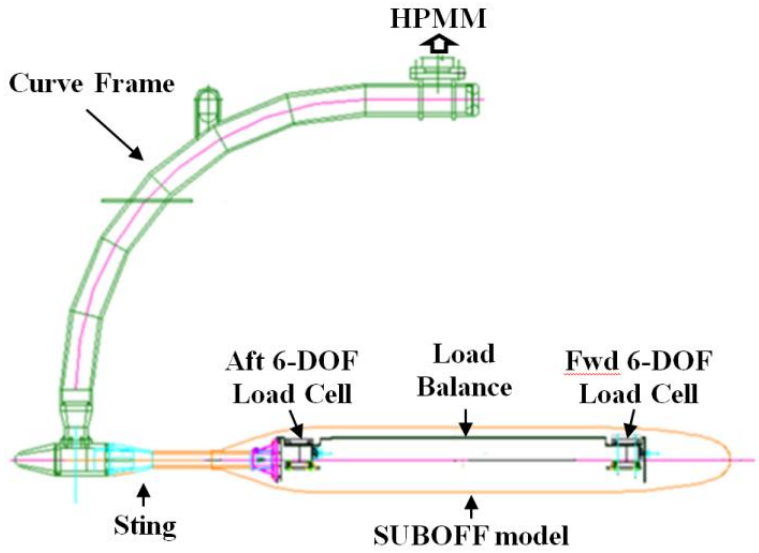

Figure 6.5: SUBOFF support rig.

The experiments were conducted under steady-state conditions, i.e. the vehicles were moved together at constant speed. The estimated uncertainty for the measured force and moment coefficients were 2.252×10^{-4} and 1.446×10^{-4} respectively, based on the recommended analysis procedure outlined in ITTC (2002).

The experiments were only carried out for the 2.239 diameter ratio due to limitations on the size of the models in relation to the dimensions of the towing tank. The SUBOFF model had to be sufficiently large to accommodate the load balance, while both captive models had to be sufficiently small to fit within the towing tank to provide meaningful data without causing excessive blockage effects. Although the 2.239 diameter ratio reduced the dominance of the larger vehicle on the flow and pressure regime and the resulting behaviour of the smaller SUBOFF model, it was reasoned that good agreement between experimental and CFD results at the 2.239 diameter ratio provided sufficient validation for the CFD model to be extended to the full-scale cases investigated.

6.5 CFD Verification and Validation

6.5.1 CFD Verification and Validation

In order to establish the mesh requirements for the simulations, the effects of the mesh resolution on the predicted interaction forces and moments acting on the SUBOFF model were examined.

An initial mesh model was created based on the following criteria: the surface area of the mesh model of the vehicles was within 0.1% of the geometry model with a maximum domain mesh body size equivalent to the diameter of the Explorer. The non-dimensional distance (y^+) of the first inflation layer around the SUBOFF and Explorer for the various simulation runs was maintained below one in order to adequately resolve the viscous layer and accurately predict the forces and moments on the vehicles using the BSLRSM simulation (Leong et al. 2014a). The total thickness of the inflation layers around the vehicles was matched to two times Prandtl's theoretical estimate of turbulent boundary layer thickness over a flat plate, i.e. $2\times0.16L_S/\mathrm{Re}_{L_S}^{1/7}$ (White 2011), where L_S is the surface length of the vehicle. Under-prescribing the total thickness below 1.5 times the theoretical estimate results in higher longitudinal force predictions and lower lateral force predictions compared to the

recommended thickness. Over-prescribing the total thickness has no noticeable effect on the predictions (Leong et al. 2014a). The surface mesh size on the SUBOFF and Explorer was selected as the refinement variable for the mesh independence study. The following discusses the mesh independence study conducted at a speed of $Re_{Explorer} = 9.545\times10^{7}$, with the SUBOFF fixed at R_{Long} and R_{Lat} of 0.00 and 0.21 respectively.

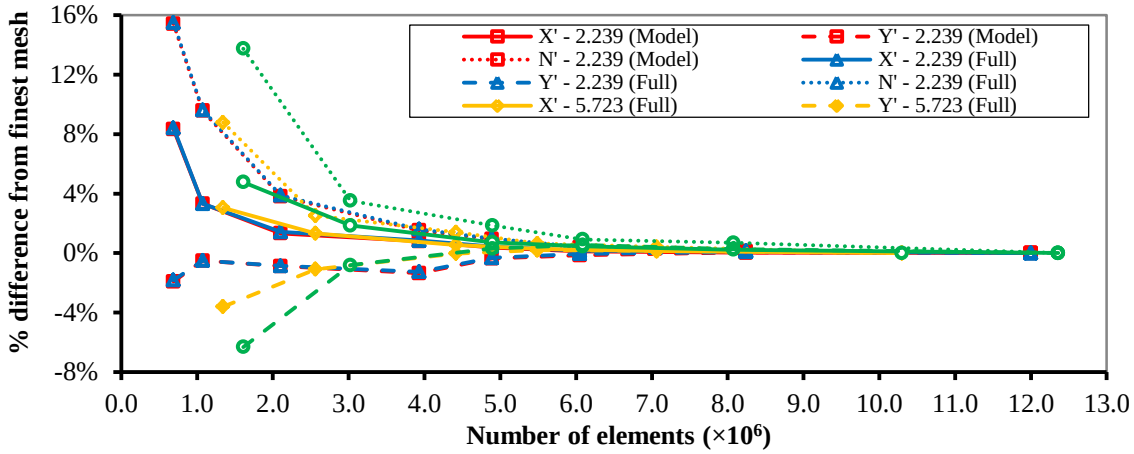

Figure 6.6: Percentage difference of the longitudinal force coefficient *X'*, lateral force coefficient *Y'*, and yawing moment coefficient *N'* predictions from the finest mesh solution versus number of mesh elements for the model scale and full-scale diameter ratios investigated.

Figure 6.6 shows the percentage difference of the predicted longitudinal force, lateral force, and yawing moment for the finest mesh solution as a function of the mesh element density for the diameter ratios investigated. For the 2.239 diameter ratios, it is seen that at 3.9 million elements and above, the forces and moment predictions for both the model scale and full-scale were within 2% of the finest mesh investigated (hereafter referred to as 'mesh independence'). The mesh independence of the moment predictions occurred at higher mesh densities compared to the forces predictions. The similar mesh independence requirement between the two scales indicates that that the mesh model settings can be scaled based on Re for the current study. At the higher diameter ratios, the mesh independence of the forces and moments occurred around 4.3 million elements for the 5.723 diameter ratio and 4.9 million elements for the 14.634 diameter ratio. The increase in mesh density requirement for mesh independence as the diameter ratio increases is due to the decrease in the displacement of the SUBOFF. As a conservative measure the 4.9, 5.4 and 6.0 million elements mesh model configurations were used to represent the 2.239, 5.723 and 14.634 diameter ratio simulations

respectively, as they were well within 1% of the forces and moment predictions of the finest mesh investigated and provided good flow visualisation to assist with the interpretation of the results.

6.5.2 Validation against Experimental Data

In order to assist with validation of the CFD results against the experimental data, the computational fluid domain was given the same dimensions as the AMC towing tank except for the domain length, which was reduced from 100m to 40m in order to reduce the computational requirement while ensuring that the pressure and wake fields generated by the vehicles were well resolved within the domain. The free surface of the water, and the experimental rig used to support the vehicles were modelled (Figure 6.7) in order to account for their effects on the interaction forces and moments acting on the SUBOFF.

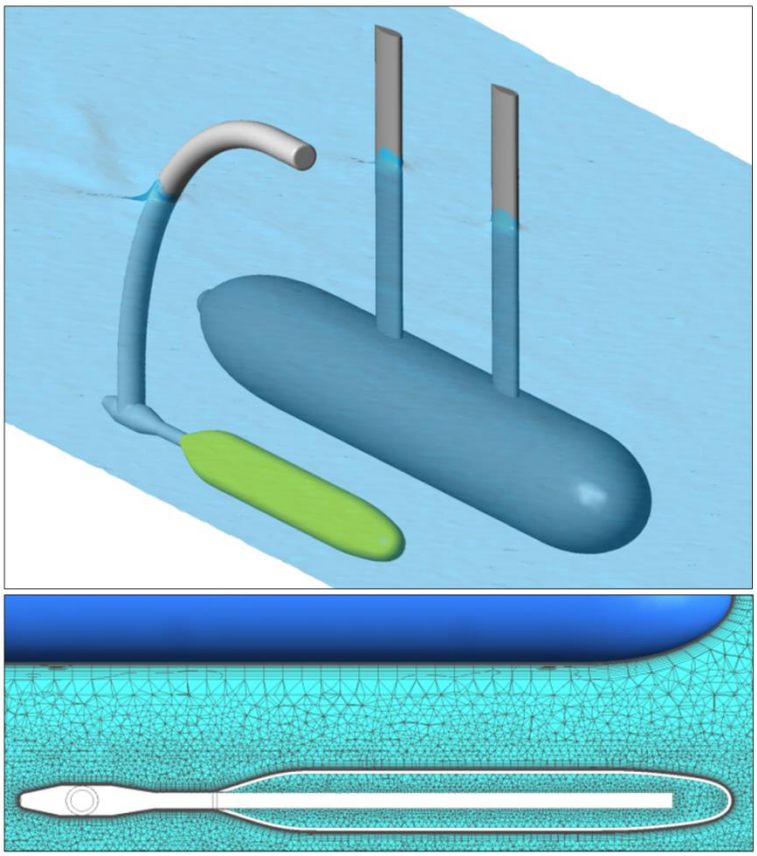

Figure 6.7: CFD model of the experimental setup with the free surface and support rigs modelled (top) and mesh model (bottom).

The validation was conducted at the R_{Lat} of 0.21 and R_{Long} between -0.62 and 0.92. The limited range of the R_{Long} positions investigated was due to limitations in the available test area on the carriage and the towing tank. Figures 6.8, 6.9, and 6.10 show the CFD predicted longitudinal force, lateral force, and yawing moment respectively acting on the SUBOFF at different R_{Long} in comparison with the experimental measurements. The figures show good agreement between the CFD and experimental results throughout the R_{Long} range, with the difference being less than the experimental uncertainty, i.e. 2.252×10^{-4} for the force coefficients and 1.446×10^{-4} for the moment coefficients. The figures also show the CFD model scale and full-scale predictions with no blockage and free surface effects on the flow around the vehicles. The latter was achieved by extending the domain boundaries six $L_{Explorer}$ away from the $CB_{Explorer}$, with the exception of the outlet which was kept eight body lengths away. The model scale predictions with the boundaries extended indicated a substantial blockage effect in the EFD results. Thus, the extended domain was used for the remainder of the study. The close agreement between the model scale and full-scale predictions with the extended boundaries showed that Re scaling based on the $L_{Explorer}$ was appropriate for dynamic similarity between the two scales, thus providing sufficient validation for the CFD model to be extended to the full-scale cases investigated.

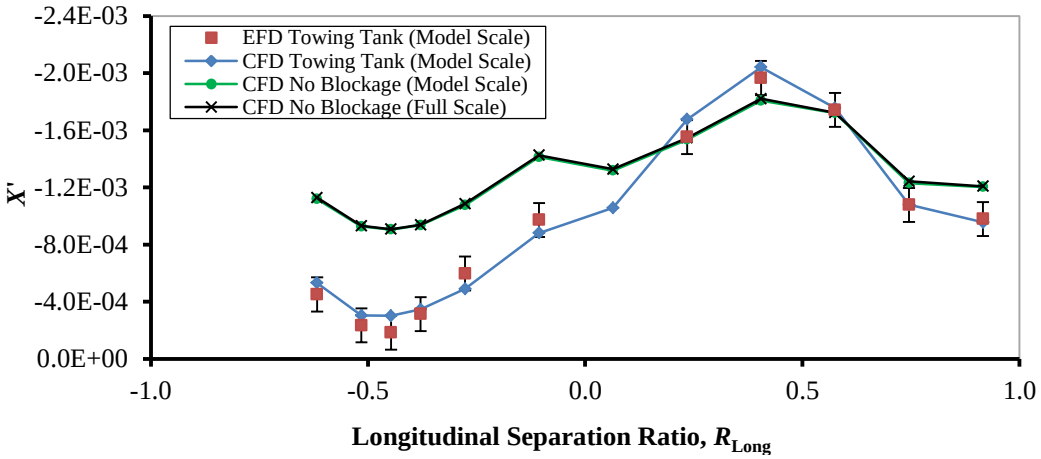

Figure 6.8: CFD and experimental results of the longitudinal force coefficient (X') on the SUBOFF vs longitudinal separation ratio (R_{Long}) for a diameter ratio of 2.239 at $Re_{Explorer}$ = 2.466×10^{6} and R_{Lat} = 0.21.

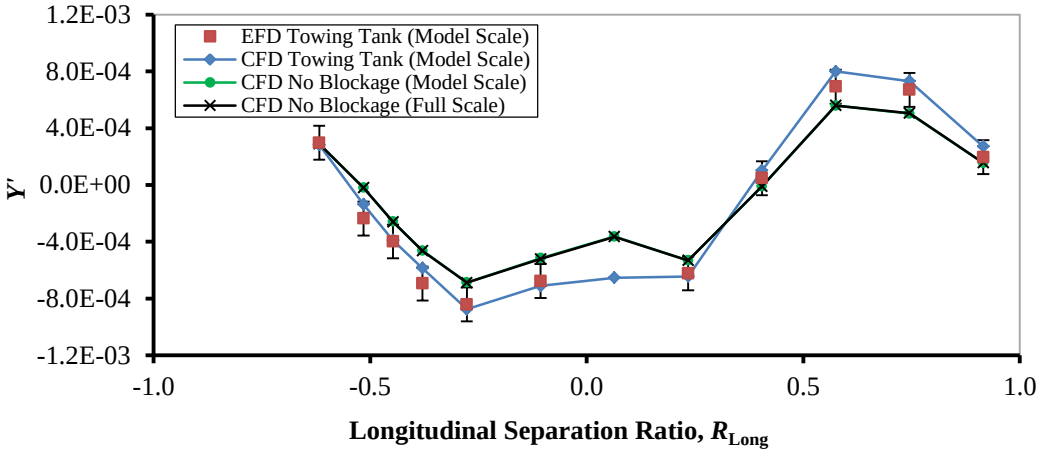

Figure 6.9: CFD and experimental results of the lateral force coefficient (Y') on the SUBOFF vs longitudinal separation ratio (R_{Long}) for a diameter ratio of 2.239 at $Re_{Explorer} = 2.466\times10^6$ and $R_{Lat} = 0.21$.

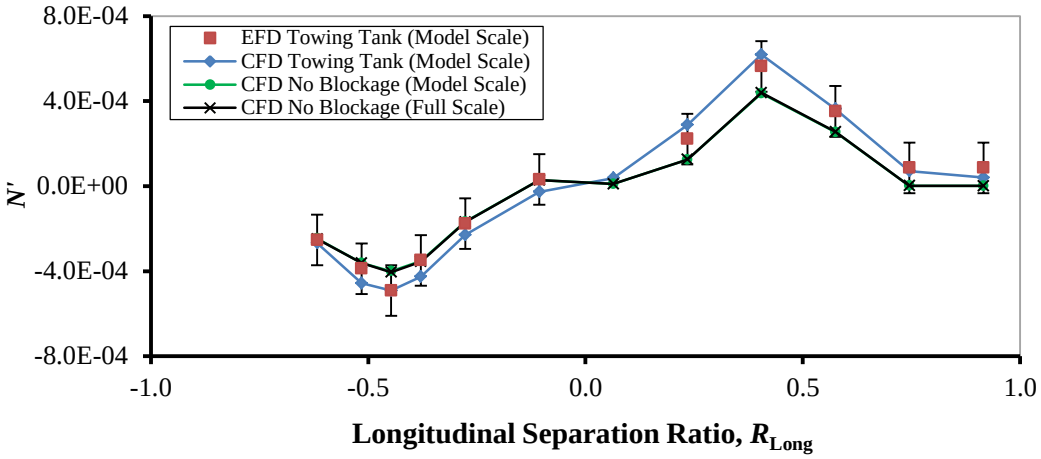

Figure 6.10: CFD and experimental results of the yawing moment coefficient (N') on the SUBOFF vs longitudinal separation ratio (R_{Long}) for a diameter ratio of 2.239 at $Re_{Explorer} = 2.466\times10^6$ and $R_{Lat} = 0.21$.

6.6 Results and Discussion

6.1 Forward Speed

Figures 6.11, 6.12, and 6.13 give the longitudinal force coefficient, lateral force coefficient, and yawing moment coefficient respectively on the SUBOFF for the full-scale diameter ratio of 2.239 at different R_{Long} and forward speeds, and at a constant R_{Lat} of 0.21. The lateral force and yawing moment coefficients with respect to R_{Long} were similar for the forward speeds

investigated. However, the longitudinal force coefficient (X') increased as the forward speed increased. Further examination revealed that the change in longitudinal force coefficient due to the influence of the interaction effects was independent of the forward speed (see Figure 6.14). The interaction effect was obtained by subtracting the longitudinal force coefficient of the SUBOFF alone at R_{Long} = -3.0 (X'_{Ref}) from X', i.e. X'_{Ref} - X'. These findings suggest that the influence of the interaction on the longitudinal force, lateral force, and yawing moment coefficients is independent of Re. Therefore, for the remainder on the study, test cases at one Re speed is used to investigate the interaction behaviour of the three coefficients. The behaviour of the interaction is hereafter represented as X' - X'_{Ref}, Y' - Y'_{Ref}, and N' - N'_{Ref} for the longitudinal force, lateral force, and yawing moment coefficients respectively in order to focus on the influence of the interaction.

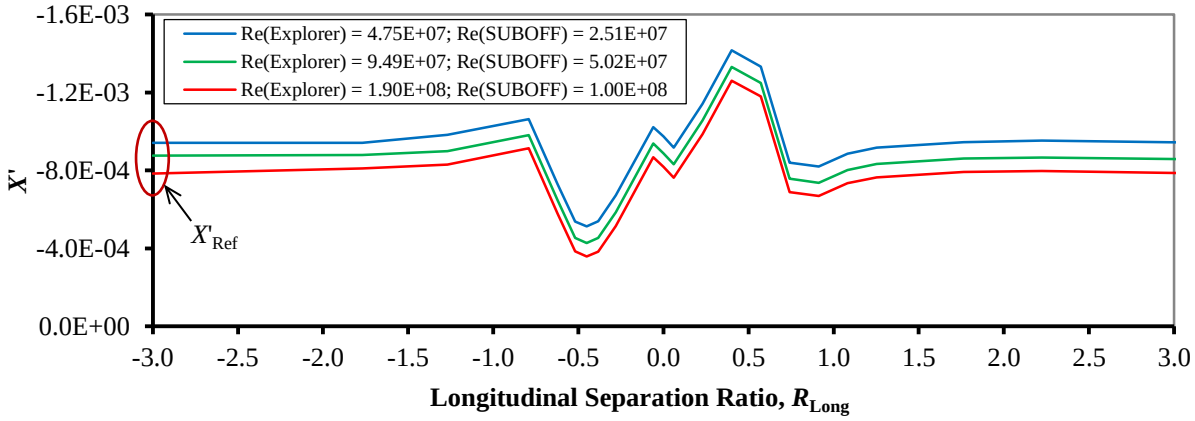

Figure 6.11: Longitudinal force coefficient X' of the SUBOFF vs longitudinal separation ratio R_{Long} for the full-scale 2.239 diameter ratio at R_{Lat} = 0.21.

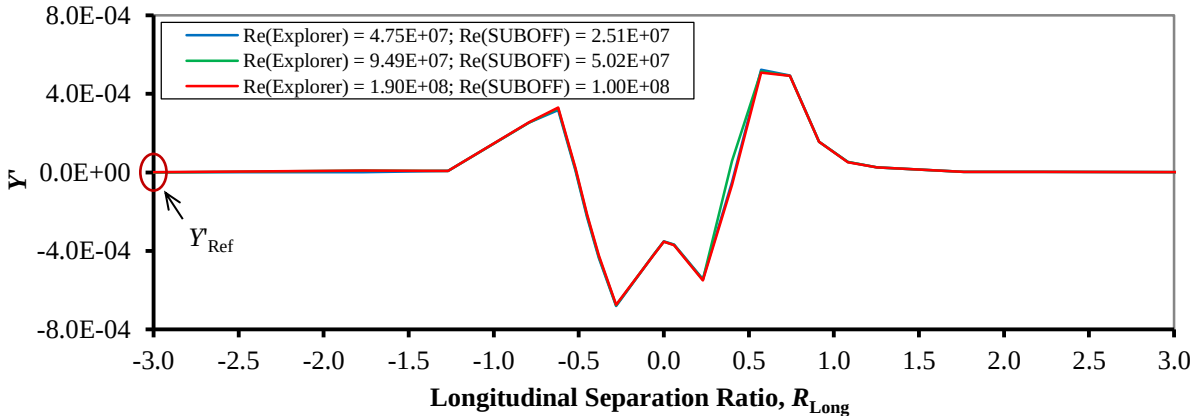

Figure 6.12: Lateral force coefficient Y' of the SUBOFF vs longitudinal separation ratio R_{Long} for the full-scale 2.239 diameter ratio at R_{Lat} = 0.21.

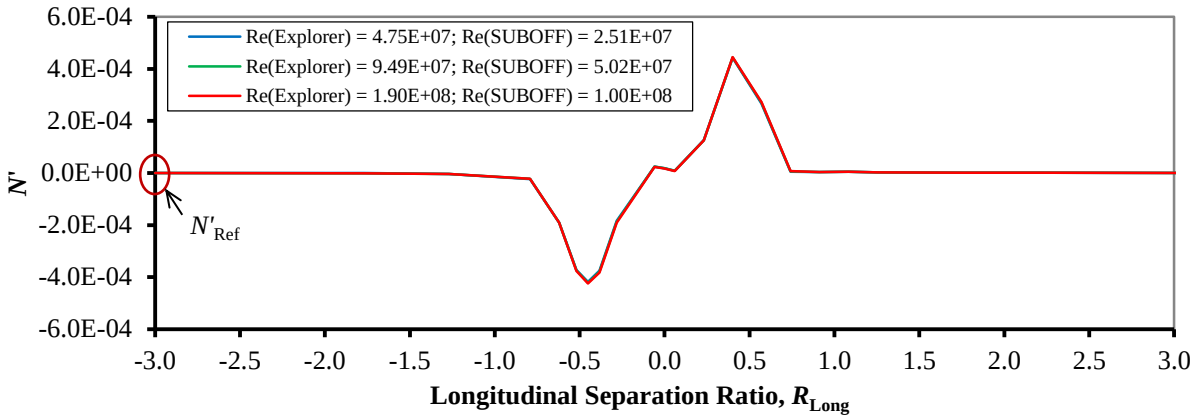

Figure 6.13: Yawing moment coefficient N' of the SUBOFF vs longitudinal separation ratio R_{Long} for the full-scale 2.239 diameter ratio at R_{Lat} = 0.21.

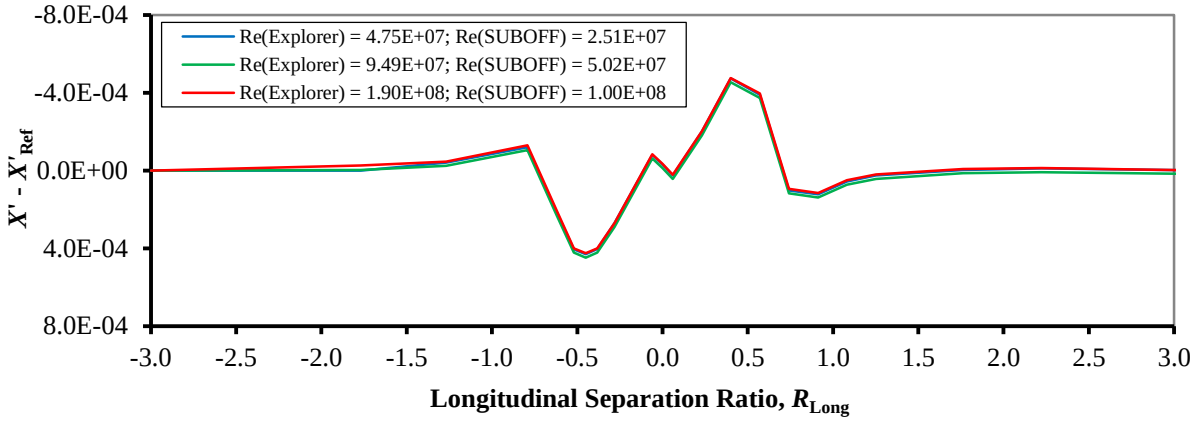

Figure 6.14: Interaction influence on the longitudinal force coefficient $X' - X'_{Ref}$ of the SUBOFF vs longitudinal separation ratio R_{Long} for the full-scale 2.239 diameter ratio at R_{Lat} = 0.21.

6.2 Relative Size

The interaction dominance of the Explorer over the smaller SUBOFF will depend on the relative size between the two vehicles. Figures 6.15, 6.16, and 6.17 show the influence of the interaction on the longitudinal force coefficient, lateral force coefficient, and yawing moment coefficient respectively acting on the SUBOFF with respect to different R_{Long} and full-scale diameter ratios at the forward speed of $Re_{Explorer} = 9.49\times10^{7}$, and R_{Lat} of 0.21. The figures show that the peaks and troughs of the interaction influence on the force and moment coefficients decrease as the diameter ratio increases. This is due to the exposure of the SUBOFF to the pressure field of the Explorer decreasing as the SUBOFF becomes relatively smaller. However, the decrease in the interaction influence on the yawing moment coefficient

of the SUBOFF with respect to the increase in diameter ratio was much less than that for the longitudinal and lateral force coefficients. The yawing moment coefficient is produced by the difference between the clockwise moment and anticlockwise moment about the $CB_{SUBOFF,}$ and thus can remain similar between the three different diameter ratios (see Figure 6.18). This therefore indicates that a change in diameter ratio does not necessarily reduce the susceptibility of the SUBOFF to the adverse effects of the interaction since the manoeuvrability of an AUV is adversely affected by both the external forces and moments acting on it.

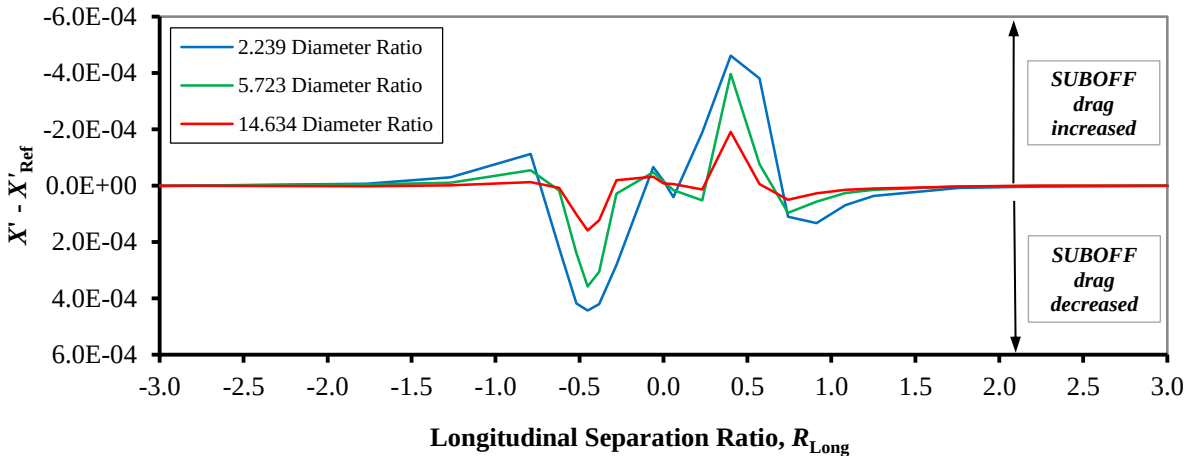

Figure 6.15: Interaction influence on the longitudinal force coefficient ($X' - X'_{Ref}$) vs longitudinal separation ratio R_{Long} for the full-scale diameter ratios of 2.239, 5.723, 14.634 at $Re_{Explorer} = 9.49\times10^7$ and $R_{Lat} = 0.21$.

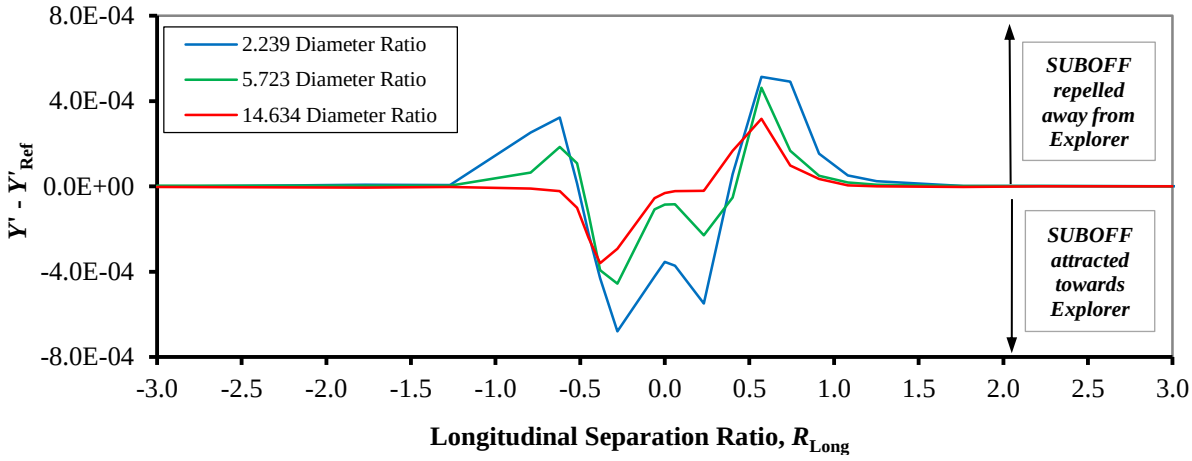

Figure 6.16: Interaction influence on the lateral force coefficient ($Y' - Y'_{Ref}$) vs longitudinal separation ratio R_{Long} for the full-scale diameter ratios of 2.239, 5.723, 14.634 at $Re_{Explorer} = 9.49\times10^7$ and $R_{Lat} = 0.21$.

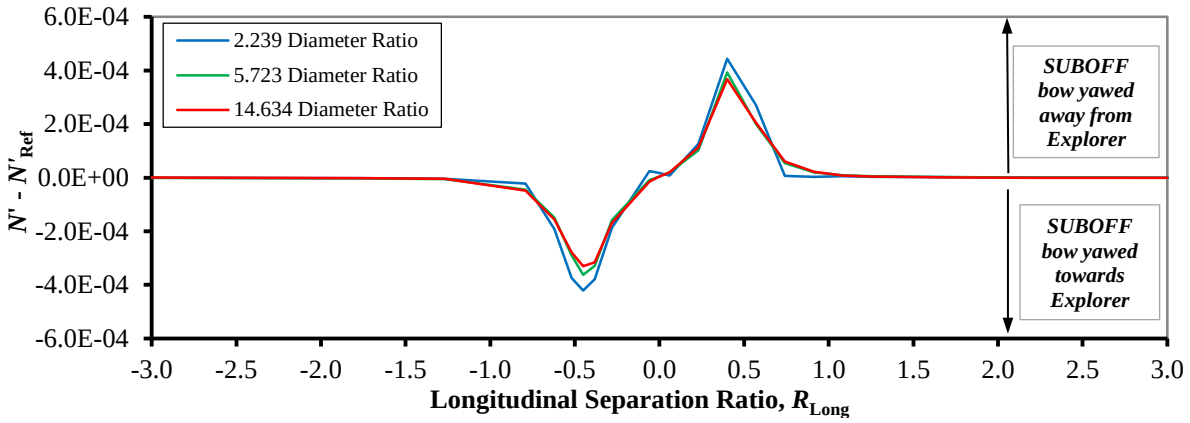

Figure 6.17: Interaction influence on the yawing moment coefficient ($N' - N'_{Ref}$) vs longitudinal separation ratio R_{Long} for the full-scale diameter ratios of 2.239, 5.723, 14.634 at $Re_{Explorer} = 9.49\times10^{7}$ and $R_{Lat} = 0.21$.

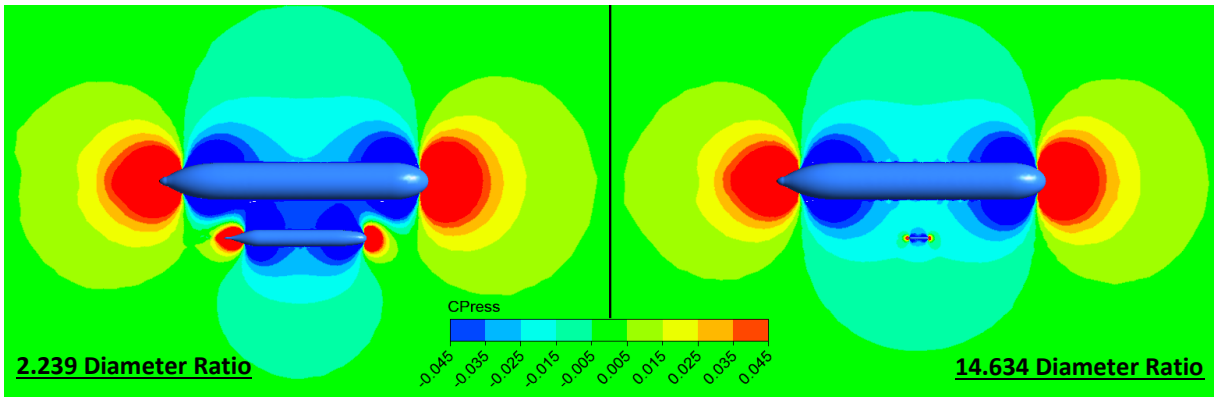

Figure 6.18: Pressure coefficient contours of the flow around the SUBOFF and Explorer models at $Re_{Explorer} = 9.49\times10^{7}$ and $R_{Lat} = 0.21$ for the diameter ratios of 2.239 on the left and 14.634 on the right. The pressure coefficient contour range is clipped at $\pm4.458\times10^{-2}$.

Figures 6.15 and 6.17 show that while the increase in diameter ratio reduces the interaction influence of the Explorer on the longitudinal force and yawing moment coefficient of the SUBOFF, the trends of the two coefficients remain relatively similar between the diameter ratios. The trend of the lateral force coefficient however, differs between the R_{Long} of -0.4 and 0.4 (see Figure 6.16), whereby a noticeable attraction of the SUBOFF to the Explorer is present when the former is around amidships of the latter, i.e. $R_{Long} = 0.0$. The attraction region around the $R_{Long} = 0.0$ is shown to diminish when the diameter ratio increases to 14.634. This behaviour is due to the constriction of the flow between the two vessels at the lower diameter ratios, thus increasing the magnitude and size of the negative pressure field between them (see Figure 6.18).

6.3 Relative Longitudinal Position

Given the large quantity of data representing the interaction effects on the force and moment coefficients of the AUV for different diameter ratios, the following discussion focuses on the data for the diameter ratio of 14.634 as it represents the relative size between a typical conventional submarine and an AUV. In Figure 6.18 it is seen that the interaction effects on the force and moment coefficients of the SUBOFF are due to the pressure differences generated by the Explorer. They change from positive pressure fields around the Explorer's stern and bow tips, to the negative pressure field along the length of the Explorer, which intensifies around where the curved sections of the bow and stern meet with the parallel midsection of the Explorer.

Figures 6.19, 6.20, and 6.21 give the interaction influence on the longitudinal force, lateral force, and yaw moment coefficients respectively of the SUBOFF with respect to different R_{Long} for the full-scale diameter ratio of 14.634 at the forward speed of $\text{Re}_{\text{Explorer}} = 9.49\times10^{7}$, $\text{Re}_{\text{SUBOFF}} = 7.68\times10^{6}$, and $R_{\text{Lat}} = 0.21$.

The longitudinal force interaction influence in Figure 6.19 begins at around R_{Long} of -1.3, when the bow of the SUBOFF enters the positive pressure field aft of the Explorer resulting in a slight increase in the drag coefficient (see Figure 6.22). At around R_{Long} of -0.6, the SUBOFF's bow progresses into the negative pressure field around the stern region of the Explorer, while the SUBOFF's stern remains in the relatively higher pressure field thus significantly reducing its drag coefficient (see Figure 6.19). This reduction peaks at around R_{Long} of -0.45, which then declines and recovers to the base value at around R_{Long} of -0.3. Between the R_{Long} of -0.3 and 0.2, the negative pressure field along the Explorer is relatively uniform longitudinally and thus the interaction has a minimal effect on SUBOFF drag. However, as the SUBOFF's bow progresses into the positive pressure field around the bow of the Explorer (R_{Long} = 0.2), the stern of the SUBOFF is yet within the negative pressure region, resulting in a significantly increase in drag. This peaks at around R_{Long} of 0.4 and then decreases as the whole of the SUBOFF body moves into the forward positive pressure field of the Explorer. The drag further decreases as the bow of the SUBOFF passes through the positive pressure field and returns to the base value as the SUBOFF's stern clears the positive pressure field around R_{Long} of 1.8.

From Figure 6.20 it is seen that at around R_{Long} of -1.0, the SUBOFF starts to experience an attraction force towards the Explorer that increases as the SUBOFF progresses forward due to the relatively lower pressure region between the two vehicles. This attraction force peaks at around R_{Long} of -0.4, and then declines as the SUBOFF moves away from the concentrated negative pressure field located around where the curved section of the Explorer stern meets with the parallel midsection. At R_{Long} between 0.0 and 0.2, the attraction force acting on the SUBOFF is relatively small compared to the attraction force when operating around the stern the Explorer. At R_{Long} of 0.2 onwards, the SUBOFF begins to be repelled away from the Explorer as its bow progresses into the positive pressure field just forward of the Explorer. The repulsion force peaks at around R_{Long} of 0.6, which then declines and diminishes at around R_{Lat} of 1.1 as the SUBOFF clears away from the pressure field of the Explorer.

In Figure 6.21 it is noted that at around R_{Long} of -1.0, the SUBOFF starts to experience a moment that tends to yaw its bow towards the Explorer. The moment increases as the SUBOFF progresses into the negative pressure field at the stern of the Explorer and peaks at around R_{Long} of -0.4. The moment then decreases as negative pressure field around the Explorer becomes uniform, and becomes zero for a small region around R_{Long} of 0.0. Beyond this point, the moment acts to yaw the SUBOFF bow away from the Explorer and peaks at around R_{Long} of 0.4. The moment then decreases to a negligible magnitude around R_{Long} of 1.25, as the SUBOFF moves further forward of the Explorer.

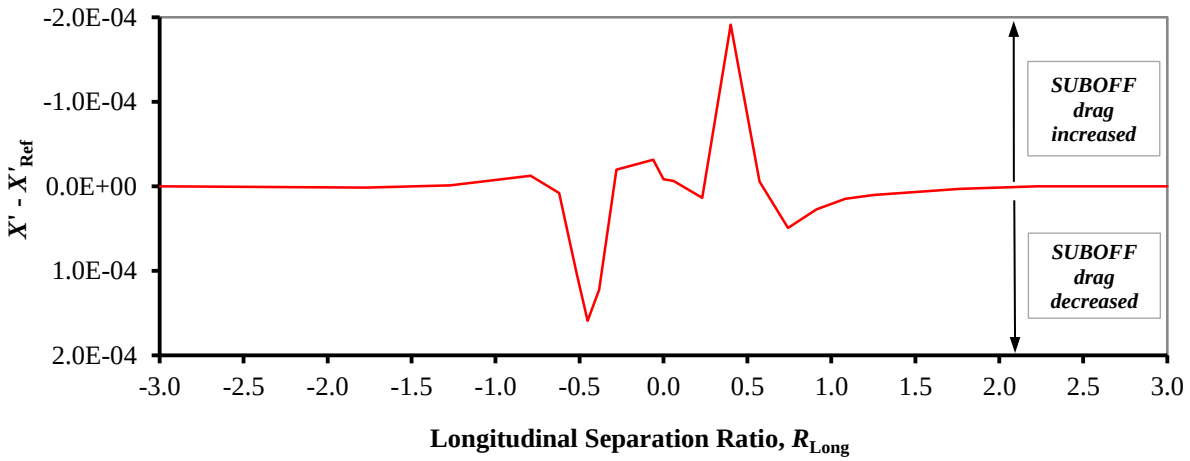

Figure 6.19: Interaction influence on the longitudinal force coefficient ($X' - X'_{Ref}$) vs longitudinal separation ratio R_{Long} for the full-scale diameter ratios of 14.634 at $Re_{Explorer} = 9.49\times10^{7}$, $Re_{SUBOFF} = 7.68\times10^{6}$ and $R_{Lat} = 0.21$.

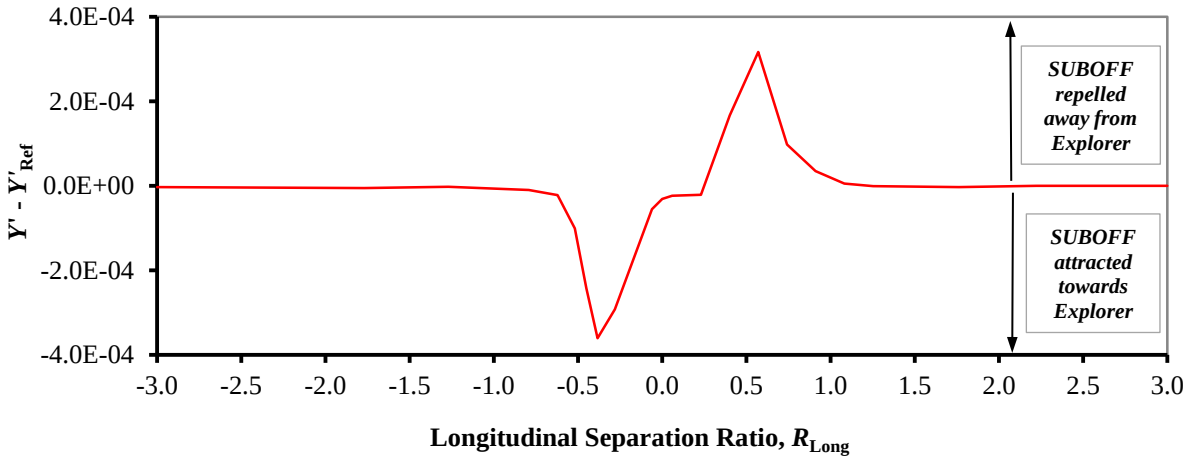

Figure 6.20: Interaction influence on the lateral force coefficient ($Y' - Y'_{Ref}$) vs longitudinal separation ratio R_{Long} for the full-scale diameter ratios of 14.634 at $Re_{Explorer} = 9.49\times10^7$, $Re_{SUBOFF} = 7.68\times10^6$ and $R_{Lat} = 0.21$.

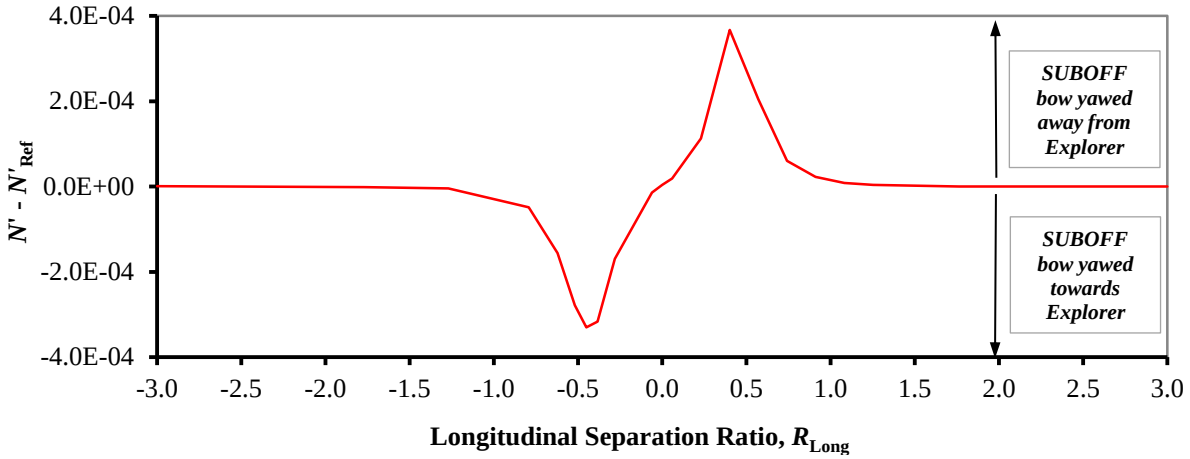

Figure 6.21: Interaction influence on the yawing moment coefficient ($N' - N'_{Ref}$) vs longitudinal separation ratio R_{Long} for the full-scale diameter ratios of 14.634 at $Re_{Explorer} = 9.49\times10^7$, $Re_{SUBOFF} = 7.68\times10^6$ and $R_{Lat} = 0.21$.

Based on the trends in the results presented above, it is undesirable for an AUV to approach the larger moving submarine from the stern of the latter. The pressure field around the stern region of the submarine increases the risk of collision as the interaction forces and moments tend to displace the AUV towards the submarine. The AUV may also encounter difficulty in approaching from the bow of the submarine as the interaction forces and moments tend to repel the AUV away from the submarine in that region.

It was also observed that the interaction forces and moments peak at round R_{Long} of -0.5 and 0.5, with a high gradient of change in the regions adjacent to the peaks. This suggests that the AUV control system will need to have a high rate of response in this region to maintain a safe trajectory. The interaction forces and moments were also found to be minimal around amidships of the submarine (i.e. R_{Long} = 0.0). However, the SUBOFF needs to travel only a small distance adjacent to this region for the direction of yawing moment to change. Thus control systems that are too sensitive may cause undesirable oscillations, as they attempt to overcompensate for the changes.

6.4 Relative Lateral Position

Figures 6.23, 6.24, and 6.25 give the interaction influence on the longitudinal force, lateral force, and yawing moment coefficients respectively acting on the SUBOFF with respect to R_{Long} for the full-scale diameter ratio of 14.634 at different $R_{Lat,}$ and at the forward speed of $Re_{Explorer} = 9.49\times10^{7}$ and $Re_{SUBOFF} = 7.68\times10^{6}$. The interaction force and moment coefficients were found to be minimal at R_{Lat} of 0.63 onwards suggesting that the SUBOFF will be relatively independent of the interaction influence when passing the Explorer at an R_{Lat} above 0.63. Below an R_{Lat} of 0.42, the interaction force and moment coefficients increase at a significant rate as the R_{Lat} decreases (see Figure 6.26). Thus, a quick response of the SUBOFF control system and adequate contribution from its control planes will be required as the vehicle approaches the Explorer with a lateral distance (R_{Lat}) of less than 0.63. The interaction forces and moments coefficients were found to be minimal around amidships of the Explorer at the different R_{Lat} examined. This suggests that the path of minimal interaction for the AUV to approach (see Figure 6.27) or depart the submarine would be laterally around the amidships of the latter.

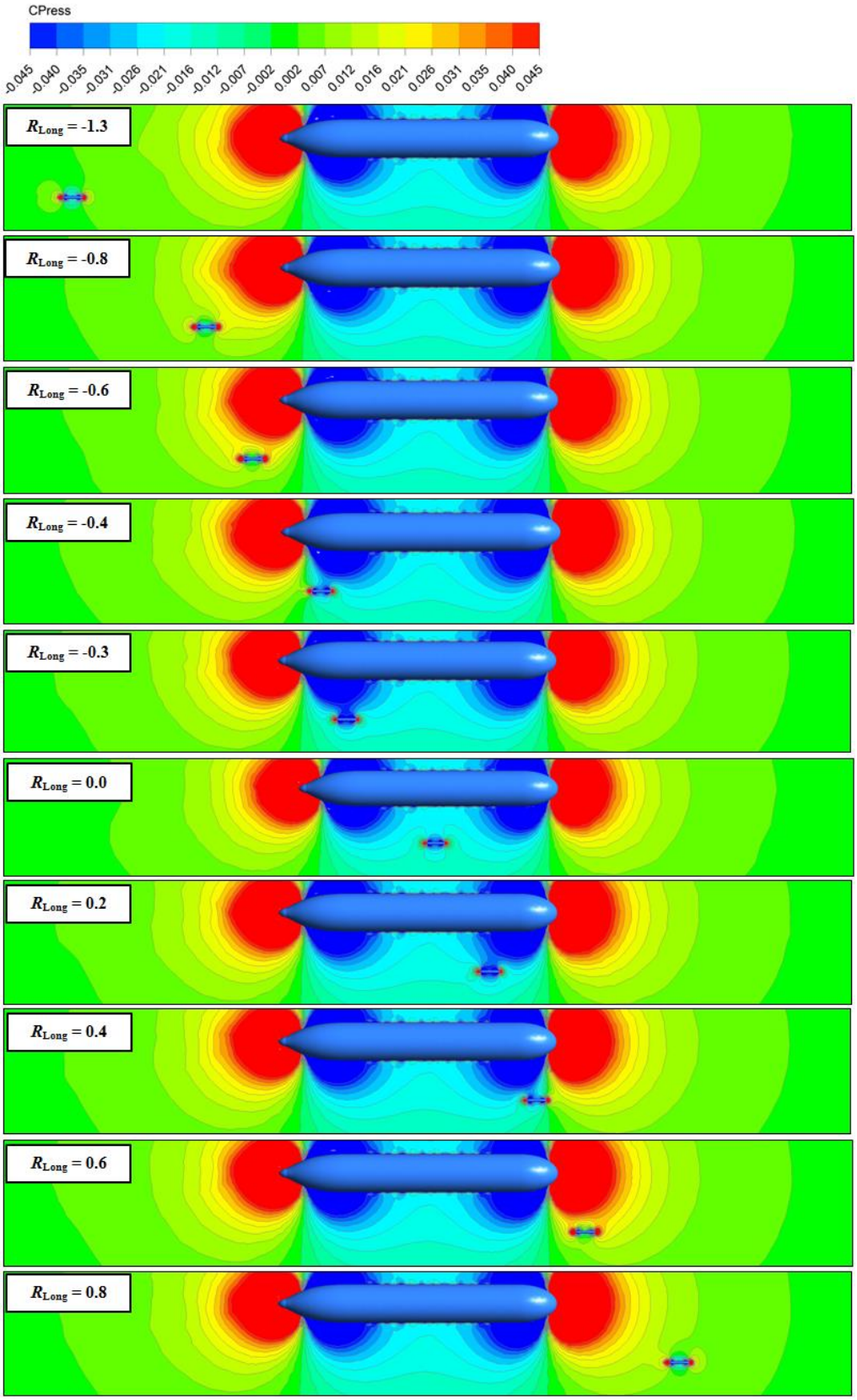

Figure 6.22: Pressure coefficient contour of the flow around the SUBOFF and Explorer at $Re_{Explorer}$ = 9.49×10^{7} and R_{Lat} = 0.21 at different R_{Long} for a diameter ratio of 2.239. The pressure coefficient contour range is clipped at $\pm4.458\times10^{-2}$.

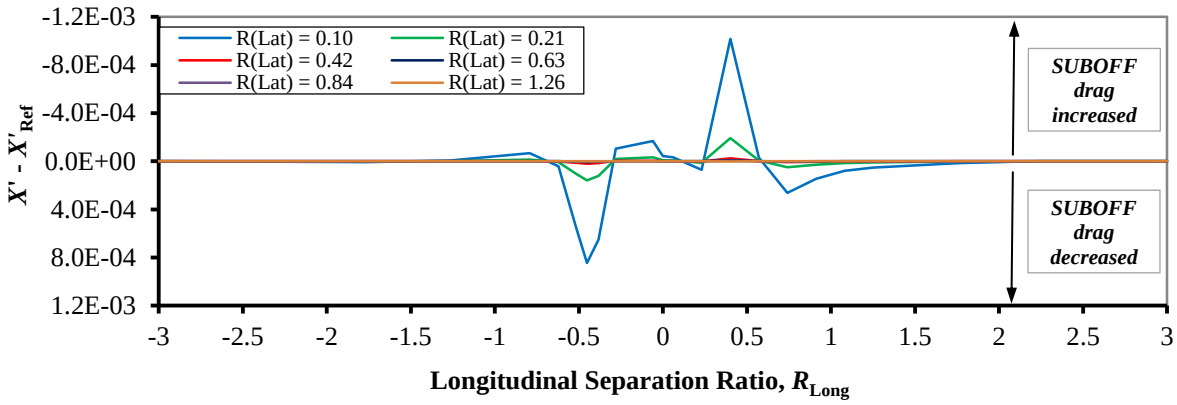

Figure 6.23: Interaction influence on the longitudinal force coefficient ($X' - X'_{Ref}$) vs longitudinal separation ratio R_{Long} at different R_{Lat} for the full-scale diameter ratio of 14.634 at $Re_{Explorer} = 9.49\times10^7$ and $Re_{SUBOFF} = 7.68\times10^6$.

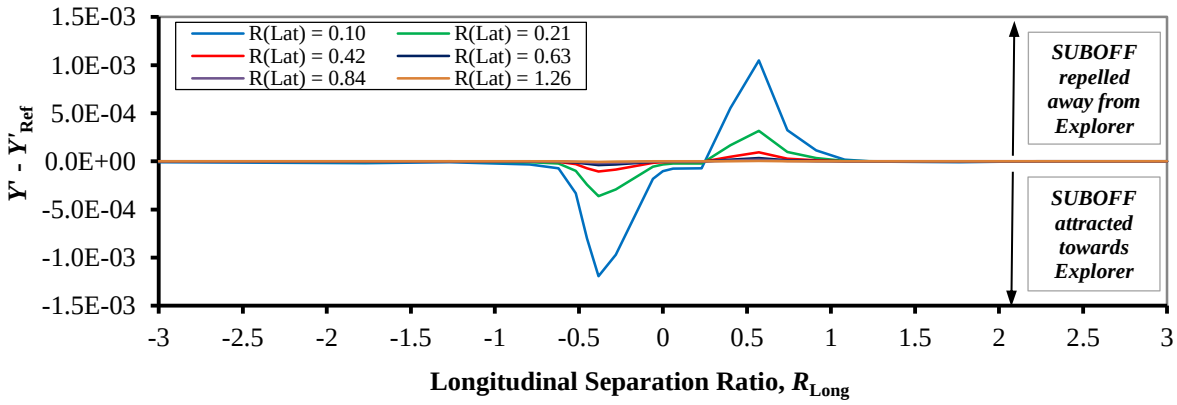

Figure 6.24: Interaction influence on the lateral force coefficient ($Y' - Y'_{Ref}$) vs longitudinal separation ratio R_{Long} at different R_{Lat} for the full-scale diameter ratio of 14.634 at $Re_{Explorer} = 9.49\times10^7$ and $Re_{SUBOFF} = 7.68\times10^6$.

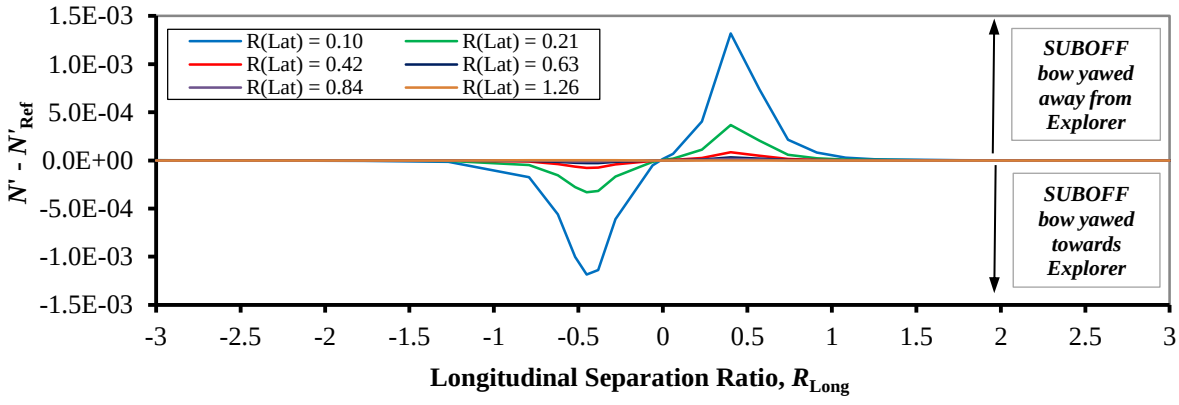

Figure 6.25: Interaction influence on the lateral force coefficient ($Y' - Y'_{Ref}$) vs longitudinal separation ratio R_{Long} at different R_{Lat} for the full-scale diameter ratio of 14.634 at $Re_{Explorer} = 9.49\times10^7$ and $Re_{SUBOFF} = 7.68\times10^6$.

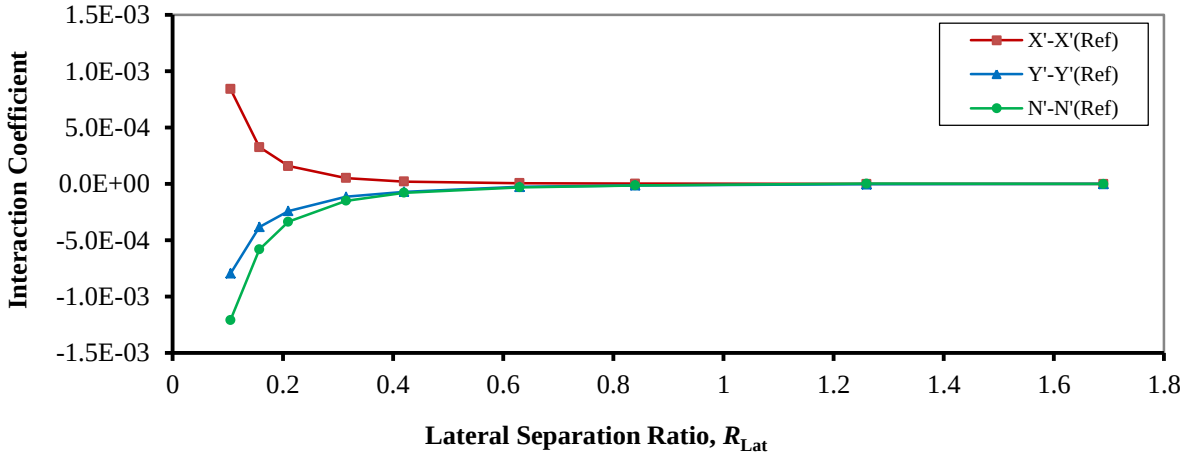

Figure 6.26: Interaction influence on the longitudinal force coefficient ($X' - X'_{Ref}$), lateral force coefficient ($Y' - Y'_{Ref}$), and yawing moment coefficient ($N' - N'_{Ref}$) vs lateral separation ratio R_{Lat} for the full-scale diameter ratio of 14.634 at R_{Long} = -0.45, $Re_{Explorer} = 9.49\times10^{7}$ and $Re_{SUBOFF} = 7.68\times10^{6}$.

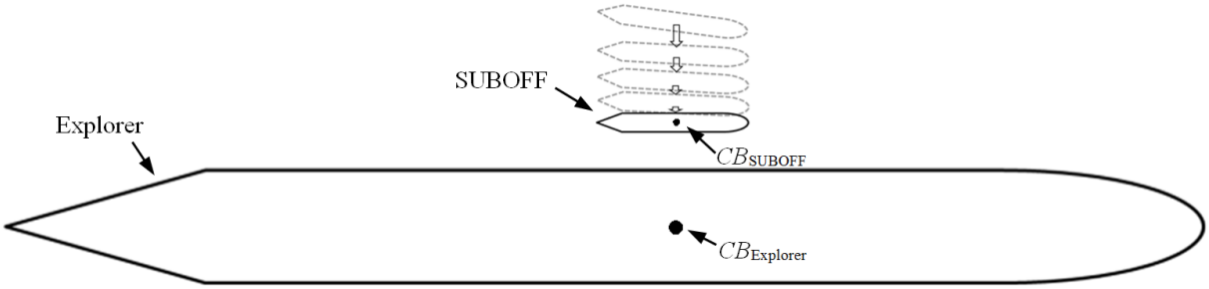

Figure 6.27: Relative path for the SUBOFF AUV to approach the Explorer submarine, where the hydrodynamic interaction is minimal.

6.7 Conclusion

In this study, steady-state CFD analysis was carried to understand and quantify the hydrodynamic interaction effects on an AUV (represented by the SUBOFF geometry) operating in proximity to a larger moving submarine (represented by the Explorer geometry). This included investigating the influence of the hydrodynamic interaction on the longitudinal force, lateral force, and yaw moment acting on the AUV, with respect to the relative lateral and longitudinal positions of the AUV, forward speed, and the relative size between the two vehicles. The CFD models were validated against measurements from model scale experiments conducted at the AMC Towing Tank.

The results showed that the interaction influence on the longitudinal force, lateral force, and yawing moment coefficients of the AUV was independent of Re. This suggests that future investigations at one operational Re would be sufficient to represent the interaction behaviour of the forces and moments acting on the AUV at different positions relative to the submarine. However, it will be of interest in future investigations to establish whether and how the relative speed between the two vehicles influences the behaviour of the interaction.

The influence of interaction was present between the relative longitudinal distance ratios (R_{Long}) of -1.3 and 1.8, and lateral distance ratios (R_{Lat}) below 0.64. The interaction forces and moments peaked around R_{Long} of -0.4 and 0.4, with the gradient steeply increasing and decreasing with respect to R_{Long} adjacent to these peaks. These regions will be a challenge to the AUV's control systems due to the high variation in the interaction forces and moments with respect a small change in relative position. It is important to note that these values will change due to the shape and size of the larger vessel, as it changes the characteristic of the pressure field it generates. Thus, it is important to obtain the interaction influence for different vessels. Nevertheless, it is expected that the observed trend in the behaviour of the interaction to be relatively similar between torpedo-shaped vessels.

The area around the stern of the submarine was identified as a high collision risk region for an AUV travelling through it, as the interaction forces and moments tend to attract the AUV towards the submarine. Similarly, the bow region of the submarine is difficult for an AUV to approach as the interaction forces and moments act to repel the AUV away from the submarine. These interaction effects were found to be minimal around amidships of the submarine ($R_{\text{Long}} = 0$), suggesting a safe path for the AUV to approach or depart the submarine laterally within that region.

[Page intentionally left blank]

Chapter 7 :

Transient Analysis of Hydrodynamic Interaction Effects on an Autonomous Underwater Vehicle in Proximity of a Moving Submarine

---

This chapter has been submitted for publication in 'The Transactions of the Royal Institution of Naval Architects, Part A1 – International Journal of Maritime Engineering' and at the time of writing is under review. The citation for the research article is:

Leong, Z.Q., Ranmuthugala, D., Penesis, I., & Nguyen, H. 2014, 'Transient Analysis of Hydrodynamic Interaction Effects on an Autonomous Underwater Vehicle in Proximity to a Moving Submarine', *Transactions RINA: Part A1- International Journal Maritime Engineering*. [Under review, 2014].

Abstract

When an Autonomous Underwater Vehicle (AUV) is operating close to a moving submarine, the hydrodynamic interaction between the two vehicles can prevent the AUV from maintaining its desired trajectory. This can lead to mission failure and, in extreme cases, collision with the submarine. This paper outlines the transient interaction influence on the hydrodynamic coefficients of an AUV operating in close proximity and in relative motion to a larger moving submarine. The effects of relative motion on the interaction behaviour were investigated via two manoeuvres, i.e. the AUV overtaking and being overtaken by the submarine at different relative forward velocities and lateral distances. The results presented are from a series of Computational Fluid Dynamics (CFD) simulations on axisymmetric AUV and submarine hull forms, with validation of the CFD model carried out through scaled captive model experiments. The results showed that an AUV becomes less susceptible to the interaction influence when overtaking at speeds higher than the submarine. The implications of the interaction influence on the AUV's ability to safely manoeuvre around the submarine are also discussed.

7.1 Introduction

Over the last decade there have been increasing efforts by navies around the world to extend the interoperation capabilities of their submarines with Autonomous Underwater Vehicles (AUVs). This direction in development is driven by the ability of AUVs to operate in hazardous environments for long periods of time with no real-time user intervention, thus mitigating any potential risk away from personnel and high value assets such as submarines and surface ships. These factors are most advantageous for reconnaissance and mine hunting missions. However, for submarine applications such missions often necessitate the AUV and submarine to operate in close proximity in order to launch, recover, and recharge the AUV, in addition to the ability to communicate data between them during operations (Hardy & Barlow 2008; Rodgers et al. 2008; DARPA 2013). This paper focuses on the interaction effects acting an AUV operating close to a moving submarine.

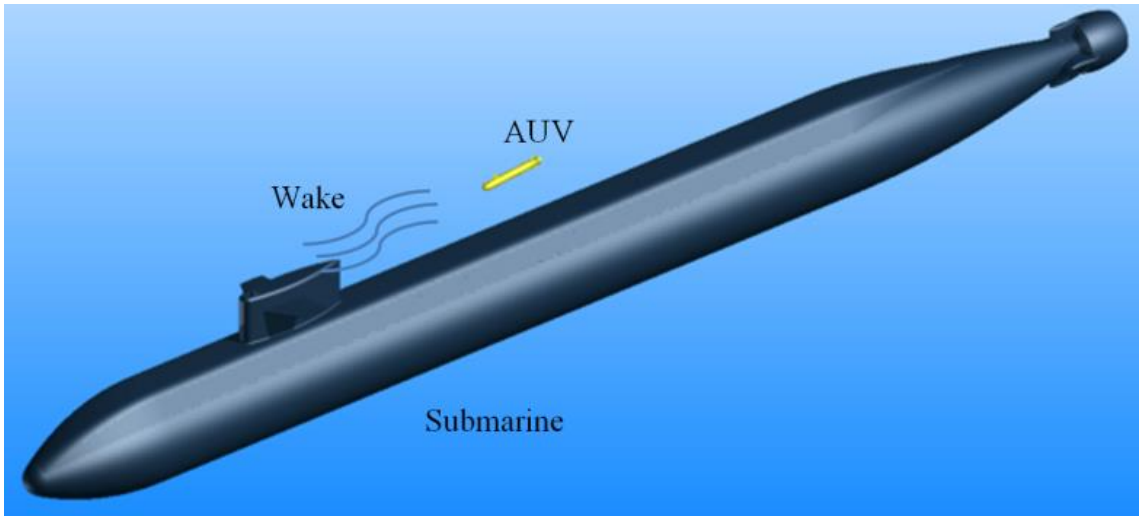

Figure 7.1: An AUV moving in the wake of a submarine.

When an AUV is operating in close proximity to a moving submarine (Figure 7.1), the AUV can experience undesirable changes in its hydrodynamic coefficients due to its interaction with the submarine's wake and pressure fields. These changes can prevent the AUV from maintaining its desired trajectory, which can lead to mission failure and, in extreme cases, collision with the submarine, resulting in damage or destruction of the AUV and possible damage to the submarine appendages or sensors (Bryne 1998). Since AUVs are generally much smaller in size relative to submarines, they would be the principle vehicle adversely affected by the interaction. Thus, designers need to have a good understanding of the

hydrodynamic interaction between the two vehicles in order to develop adequate and robust AUV control systems to ensure vehicle stability and identify operating parameters in which an AUV can effectively and safely manoeuvre near a moving submarine.

For underwater data communication between an AUV and a submarine, acoustic modems can transfer data up to a few kilobits per second over distances well exceeding one thousand meters (Gallimore et al. 2010). Optical modems (i.e. lasers) offer much higher transfer rates of up to a few megabits per second over distances up to a few hundred meters, depending on the turbidity of the water (Scholz 2011). However, due to the restriction on a submarine to remain covert throughout missions, data transfer with AUVs tends to be carried out at shorter distances or ideally after the recovery of the AUV in order to reduce the probability of detection by third parties. Furthermore, the power source of the AUV is likely to need recharging before progressing to the next mission. This has led to a growing interest in the submarine recovering the AUV for both data transfer and power recharge, thus requiring the AUV to safely negotiate the hydrodynamic interaction effects as it approaches the submarine.

Unlike the recovery of an AUV at the surface, underwater recovery via a submarine presents several unique challenges. Both vehicles rely on their propeller and the hydrodynamic contribution of their control planes for manoeuvring and positioning, thus their hydrodynamic control will reduce as the vehicles reduce speed. Furthermore, unless they have additional side thrusters along their body, they have limited ability to adjust their transverse positions. These factors dictate that the AUV must be recovered while the submarine is moving, with the aid of a mechanism to capture the AUV when it is close enough to the submarine hull in order to overcome the transverse positioning limitations. Further considerations in favour of recovering an AUV via a capture mechanism from a moving submarine are discussed in detail by Irani et al. (2014) and Watt et al. (2011).

While several studies have focused on recovery options for AUVs via a submarine (Watt et al. 2011; Currie et al. 2014; Hardy & Barlow 2008; Irani et al. 2014), studies characterising the effects of the hydrodynamic interaction between submerged vessels remain scarce in the public domain. Using steady-state Computational Fluid Dynamics (CFD) simulations, Fedor (2009) investigated the hydrodynamic interaction effects on an AUV near a moving submarine with the aim of establishing a feasible region in which to launch and recover the AUV around the submarine sail. It was found that in the forward region of the sail the

interaction acts to repel the AUV from the submarine, with the repelling force increasing as the AUV gets closer to the submarine. General trends of the forces and moments acting on the AUV were less observable in the regions to the side and astern of the sail due to disturbances from the horseshoe vortices generated by the sail. The results suggest that it is desirable for recovery to be carried out forward of the sail.

Bryne (1998) developed a real-time manoeuvring simulator to evaluate and demonstrate the manoeuvring and control performance of the Phoenix AUV undertaking a docking operation via the torpedo tube of a moving submarine. The hydrodynamic interaction between the two vehicles was modelled by introducing a parabolic flow velocity profile along the submarine hull in order to represent the reduced flow velocity encountered by the AUV as it approached the boundary layer of the submarine. However, this is an over-simplification of the interaction effects, since it did not account for operational issues associated with the more dominant potential field effects generated by a submarine that can either repel or attract the AUV depending on their relative positions.

The studies by Bryne (1998) and Fedor (2009) offered an insight into the interaction effects acting on an AUV operating within the proximity of a larger moving underwater vessel. However, their investigations focused on locations very close to the submarine, thus the parameters surrounding the broader extent of the interaction effects and the means for the AUV to approach the regions were not discussed.

The authors have previous published results from CFD and experimental work showing that the behaviour of the interaction depends on the relative size, longitudinal position, and lateral position between the AUV and the submarine (Leong et al. 2014b). The interaction was found to attract and repel the AUV at the stern and bow regions of the submarine respectively. The magnitude of these attraction and repulsion effects varied greatly with only a small change in the relative longitudinal position, suggesting the need for an accurate and fast response control system for the AUV to adequately maintain its trajectory around the moving submarine. However, these adverse interaction effects were found to be minimal around amidships of the submarine, suggesting a safe path for the AUV to approach or depart the submarine laterally within that region. However, the results are from steady-state numerical and experimental work, i.e. the vehicles are travelling forward at the same speed at

different fixed relative positions. Therefore, the effects of relative speed between the two vehicles on the interaction effects remain to be established.

This study aims to complement the above work by examining the dynamic effects of the interaction acting on an AUV operating in close proximity and in relative motion to a larger moving submarine. The work was carried out using CFD modelling to quantify the surge force, sway force, and yaw moment acting on the AUV at different speeds, longitudinal positions, and lateral positions relative to the submarine in order to identify the behaviour of the AUV operating in the interaction zone. The CFD predictions were validated and supplemented through experimental captive-model tests. The resulting simulation model is intended to be coupled with a control system in a dynamic manoeuvring simulation to evaluate the motion behaviour of the AUV and develop the necessary algorithms to maintain the desired trajectory of the vehicle when in operation near a moving submarine.

7.2 Investigation Programme

The effects of relative motion on the interaction effects were investigated using two manoeuvres, i.e. the AUV overtaking the submarine and being overtaken by the submarine at different constant relative lateral distances and velocities (Figure 7.2). The variables investigated included the length-based coefficients of the drag force, sway force, and the yaw moment acting on the AUV, with the latter calculated at a reference point located at the centre of buoyancy of the vehicle. Table 7.1 summarises the investigation parameters and vehicle dimensions.

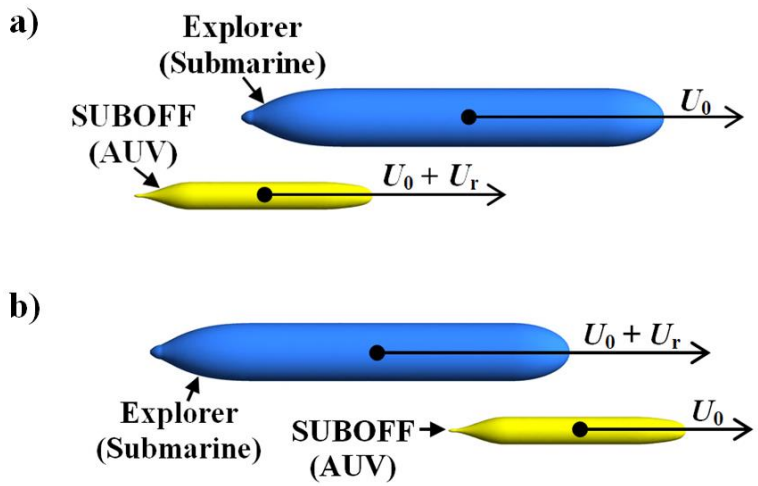

Figure 7.2: (a) AUV overtaking manoeuvre, (b) and submarine overtaking manoeuvre.

The smaller AUV was represented by the axisymmetric SUBOFF hull form (Groves et al. 1989) developed by the Defence Advanced Research Projects Agency (DARPA), while the larger body representing the submarine was a modified geometry based on the International Submarine Engineer Ltd. designed Explorer (ISE 2005). Figure 7.3 shows the two vehicle geometries, with definitions for the principal dimensions, relative longitudinal distance, and relative lateral distance. A diameter ratio (i.e. $D_{\text{Explorer}}/D_{\text{SUBOFF}}$) of 14.634 between the two vehicles was used for the relative motion study as it represents the relative size between a typical AUV and a conventional submarine.

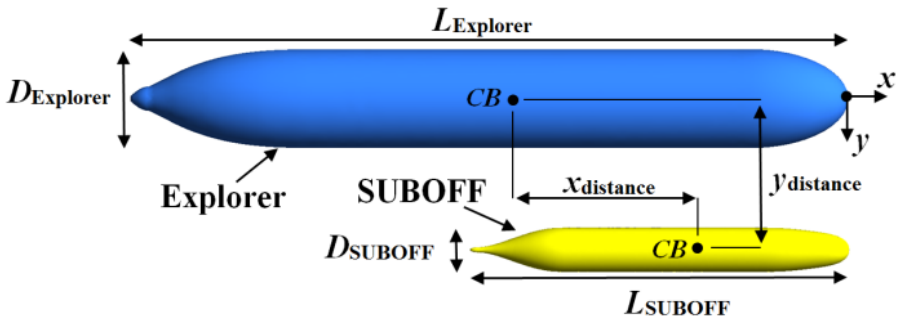

Figure 7.3: Definition of the model parameters.

Table 7.1: Vehicle dimensions and investigation parameters.

Parameter	**SUBOFF**	**Explorer**	
Length, L	4.570	56.495	[m]
Diameter, D	0.533	7.800	[m]
Displacement, ∇	8.075×10^{-1}	2.309×10^{3}	[m^3]
Base forward speed, U_0	1.50	1.50	[m s^{-1}]
Longitudinal distance ratio, R_{Long}	-2.00 to 2.00	[-]	
Lateral distance ratio, R_{Long}	0.15, 0.21, 0.32, 0.43, 0.71, 1.00	[-]	
Relative forward speed ratio, R_{U}	1.00*, 1.33, 1.67, 2.00, 2.33, 2.67	[-]	

*indicates a steady-state approach to the solution

The relative lateral distance x_{distance} and relative longitudinal distance y_{distance} were measured from the centre of buoyancy *CB* of the larger vehicle to that of the smaller vehicle. For x_{distance} a 'positive' distance signifies that the SUBOFF is located in front of the *CB* of the larger vehicles. For the remainder of this paper, the longitudinal and lateral distances, and the

relative forward and lateral speeds are referred to as non-dimensionalised ratios R_{Long}, R_{Lat}, and R_{U} i.e.,

$$R_{\mathrm{Long}} = \frac{x_{\mathrm{distance}}}{L_{\mathrm{Explorer}}} \tag{6.1}$$

$$R_{\mathrm{Lat}} = \frac{y_{\mathrm{distance}}}{L_{\mathrm{Explorer}}} \tag{6.2}$$

$$R_{\mathrm{U}} = \frac{U_0 + U_r}{U_0} \tag{6.3}$$

7.3 Simulation Setup

The simulations were performed using ANSYS CFX, a commercial CFD code. The Reynolds Averaged Navier-Stokes (RANS)-based Baseline Reynolds Stress Model (BSLRSM) was utilised in this analysis. Previous CFD and Experimental Fluid Dynamics (EFD) work by the authors have established that the BSLRSM was more accurate in predicting the forces and moments acting on underwater vessels of similar geometry to the SUBOFF, compared to the RANS-based eddy-viscosity models within CFX (Leong at al. 2014b). This is due to the BSLRSM's more comprehensive modelling of rotational flow, flow separation, and flows that are strongly anisotropic.

The ANSYS Meshing Platform (AMP) remeshing method was used to simulate the relative motion between the two bodies. The essential characteristic of this method is that the mesh in the fluid domain deforms locally around the object as it moves, and re-meshes when the mesh quality is deemed compromised in terms of accuracy and stability. This overcomes the limited motions imposed by using a pure mesh deformation approach, and allows adequate modelling of the boundary layer and rotation of the bodies compared to other dynamic mesh methods within CFX, as discussed by the authors in Leong et al. (2012).

Figure 7.4 shows the computational fluid domain in a fixed frame of reference, with its centre of origin located at the centre of buoyancy of the Explorer (CB_{Explorer}). The far field boundaries were kept six body lengths away from the CB_{Explorer}, with the exception of the outlet, which was kept eight body lengths away. This ensured that boundaries had no

blockage effect on flow around the vehicle geometries, and that the wake due to each vehicle was sufficiently resolved within the domain. The flow at the inlet was prescribed to match the desired vehicle speed, while the outlet was set as an opening with zero relative pressure. The surfaces of the vehicles were prescribed as no-slip walls, while the remaining boundaries were set as free-slip walls.

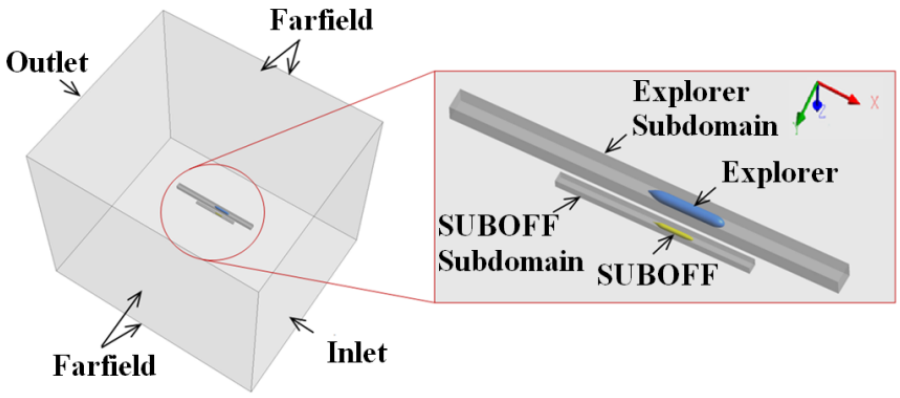

Figure 7.4: Computational fluid domain.

The fluid domain was divided into three parts: two subdomains for each of the regions around the Explorer and SUBOFF, and an outer domain for the remaining region. The division of the domain allowed the mesh of the vehicle sub-domains to be kept rigid during the solver process, while the outer domain underwent mesh deformation and remeshing, thus maintaining mesh quality around the vehicles and reducing the remeshing time. For the discretisation of the fluid domain, an unstructured mesh approach was used, i.e. triangular prismatic inflation layers around the SUBOFF to capture the boundary layer and unstructured tetrahedrons in the far field. The unstructured mesh approach was selected due to its ability to easily accommodate the mesh deformation and remeshing. The unstructured mesh approach, although it requires a higher mesh density, has also been proven to offer the same degree of accuracy in comparison to a structured mesh (Duda 2011).

7.4 Experimental Work

In order to supplement and establish the credibility of the CFD predictions, a series of captive-model experiments were conducted in the Australian Maritime College (AMC) Towing Tank. The experiments involved two testing regimes: transient measurements of the

SUBOFF undergoing pure sway motions, i.e. $y_a\sin(2\pi f)$, adjacent to the Explorer while maintaining a constant R_{Long} (Figure 7.5), and steady-state measurements of the SUBOFF fixed at different R_{Long} to the Explorer while maintaining a constant R_{Lat} (i.e. $y_a = 0$). For both manoeuvres, the two vehicles were travelling at the same constant forward speed. The experimental parameters of the manoeuvres are outlined in Table 7.2.

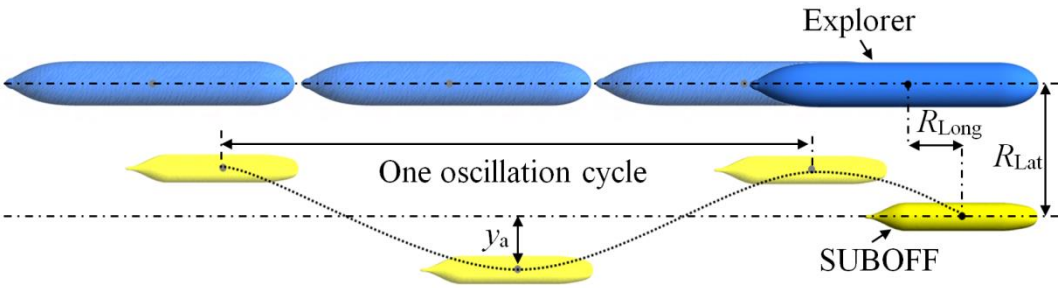

Figure 7.5: SUBOFF undergoing a pure sway manoeuvre at a constant R_{Long} to the Explorer.

Table 7.2: Experimental parameters.

Parameter	**SUBOFF**	**Explorer**	Unit
Length, L	1.552	2.935	[m]
Diameter, D	0.181	0.405	[m]
Displacement, ∇	3.162×10^{-2}	3.237×10^{-1}	[m^3]
Overtaking manoeuvre (steady-state)			
Longitudinal distance ratio, R_{Long}	-0.62 to 0.92	-	[-]
Lateral distance ratio, R_{Lat}	0.21	-	[-]
Base forward speed, U_0	1.50	1.50	[-]
Reynolds Number, Re	2.61×10^6	4.93×10^6	[-]
Pure sway manoeuvre (transient)			
Longitudinal distance ratio, R_{Long}	0.23	-	[-]
Lateral distance ratio, R_{Lat}	0.21	-	[-]
Base forward speed, U_0	1.20	1.20	[m s^{-1}]
Reynolds Number, Re	2.09×10^6	3.95×10^6	[-]
Sway oscillation frequency, f	0.2	-	[Hz]
Sway amplitude, y_a	0.14	-	[m]

7.4.1 Experimental Setup

The 100m×3.5m×1.5m tank is equipped with a manned variable speed carriage and a wave generator, and uses a Horizontal Planar Motion Mechanism (HPMM) capable of generating horizontal motion on the underwater vehicle model, and recording the resulting forces and moments. The SUBOFF model was mounted to the HPMM using a 'sting' arrangement that connects to the model through the aft end, with the forces acting on the SUBOFF model recorded via two 6-Degree of Freedom (6-DOF) load cells located inside the model as shown in Figure 7.6. The Explorer model was mounted directly onto the carriage by means of rigid supports as shown in Figure 7.7, with no forces recorded, as the objective of the work was to investigate the behaviour of the smaller vehicle due to the interaction.

The R_{Lat} between the two models was adjusted by shifting the lateral position of the SUBOFF using the HPMM, while the R_{Long} was adjusted by shifting the longitudinal position of the Explorer along the support beam. Both models were fully flooded and located at mid-depth of the tank.

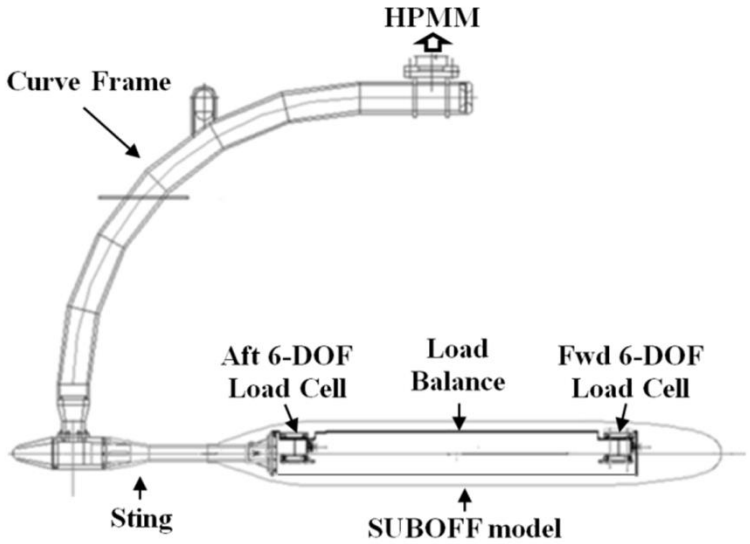

Figure 7.6: SUBOFF support rig.

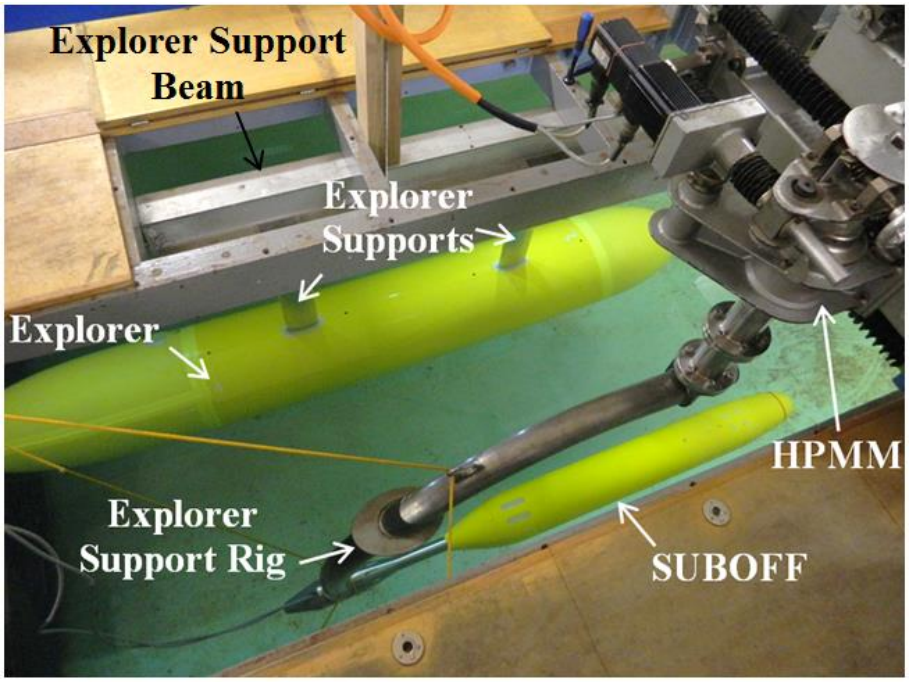

Figure 7.7: Experimental testing rig.

7.5 CFD Verification and Validation

7.5.1 Mesh Independence Study

In order to establish the mesh requirements for the simulations, the effects of the mesh resolution on the predicted interaction forces and moments acting on the SUBOFF model were examined. The mesh study was conducted at a speed of $Re_{Explorer} = 9.545\times10^{7}$, with the SUBOFF fixed at R_{Long} and R_{Lat} of 0.00 and 0.21 respectively. The surface mesh size on the SUBOFF and Explorer was selected as the refinement variable for the mesh study.

An initial mesh model was created based on the following criteria: a maximum Curvature Normal Angle of 9˚ (which creates 10 circumferential divisions along a 90˚ circular arc) in order to provide adequate resolution of the vehicles' curvature and a maximum domain mesh body size equivalent to the diameter of the Explorer. The non-dimensional distance (y^{+}) of the first inflation layer around the SUBOFF and Explorer for the various simulation runs was maintained below one in order to adequately resolve the boundary layer and accurately predict the off-axis hydrodynamic forces and moments on the vehicles using the BSLRSM simulation (Leong at al. 2014b). In order to account for the effects of the vehicle's curvature on the boundary layer thickness, the total thickness of the inflation layers around the vehicles

was matched to two times Prandtl's theoretical estimate of turbulent boundary layer thickness over a flat plate, i.e. $2\times0.16L_S/\mathrm{Re}_{L_S}^{1/7}$, where L_S is the surface length of the vehicle. The authors have found from previous CFD work (Leong et al. 2014a) that underprescribing the total thickness of the inflation layers below 1.5 times the theoretical estimate results in higher longitudinal force predictions and lower lateral force predictions. Over-prescribing the total thickness of the inflation layers has no noticeable effect on the predictions.

Figure 7.8 shows the percentage difference of the predicted longitudinal force, lateral force, and yawing moment for the finest mesh solution as a function of mesh element density for the diameter ratios investigated. For the 2.239 diameter ratio, it is seen that at 3.9 million elements and above, the forces and moment predictions for both the model scale and full-scale were within 2% of the finest mesh investigated. For the diameter ratio of 14.634, the forces and moment predictions were within 2% of the finest mesh investigated at around 4.9 million elements. The increase in mesh density requirement for mesh independence as the diameter ratio increases is due to the decrease in the displacement of the SUBOFF. As a conservative measure the 4.9 and 6.0 million elements mesh model configurations were used to represent the 2.239 and 14.634 diameter ratio simulations respectively, as they were well within 1% of the forces and moment predictions of the finest mesh investigated and thus deemed to provide a mesh independent solution.

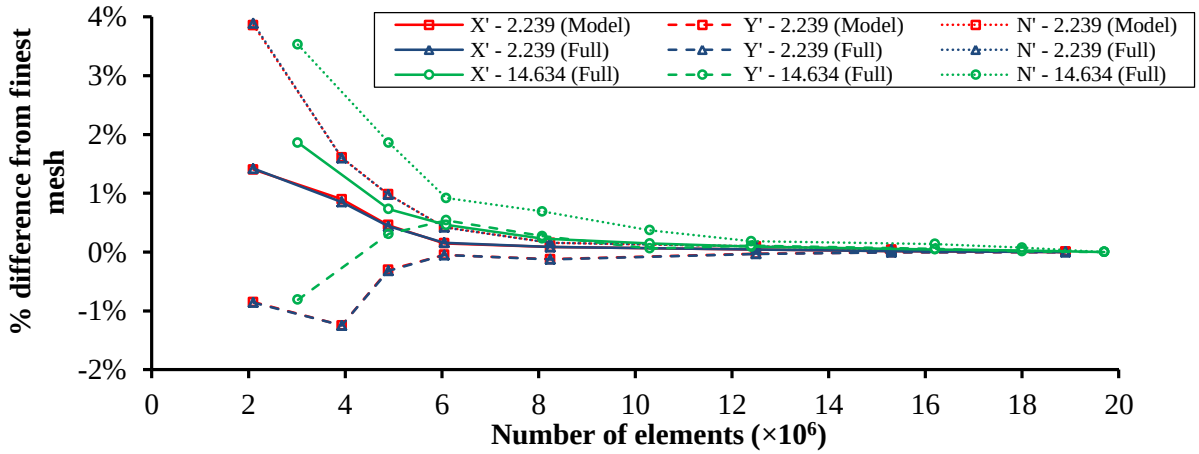

Figure 7.8: Percentage difference of the longitudinal force coefficient *X'*, lateral force coefficient *Y'*, and yawing moment coefficient *N'* predictions against the finest mesh solution as a function of number of mesh elements for the model scale and full-scale diameter ratios investigated.

7.5.2 Validation against Experiments

In order to assist with the validation, the CFD model was made to replicate the experimental setup. The free surface of the water and the experimental rig used to support the vehicles were included in the simulation model (Figure 7.9) in order to account for their effects on the interaction forces and moments acting on the SUBOFF. The computational fluid domain was given the same dimensions as the AMC towing tank except for the domain length, which was reduced from 100m to 40m in order to reduce the computational requirement while ensuring that the pressure and wake fields generated by the vehicles were well resolved within the numerical domain.

To account for the inertia forces associated with the accelerative motions in the pure sway manoeuvre, the water entrained within the SUBOFF model was also modelled (Figure 7.10). The inertia contribution of the SUBOFF shell and mounting was modelled based on Newton's second law of motion, i.e. $F=ma_y$, where F is the inertia force, m is the mass (7.4kg), and a_y is the acceleration of the sway motion

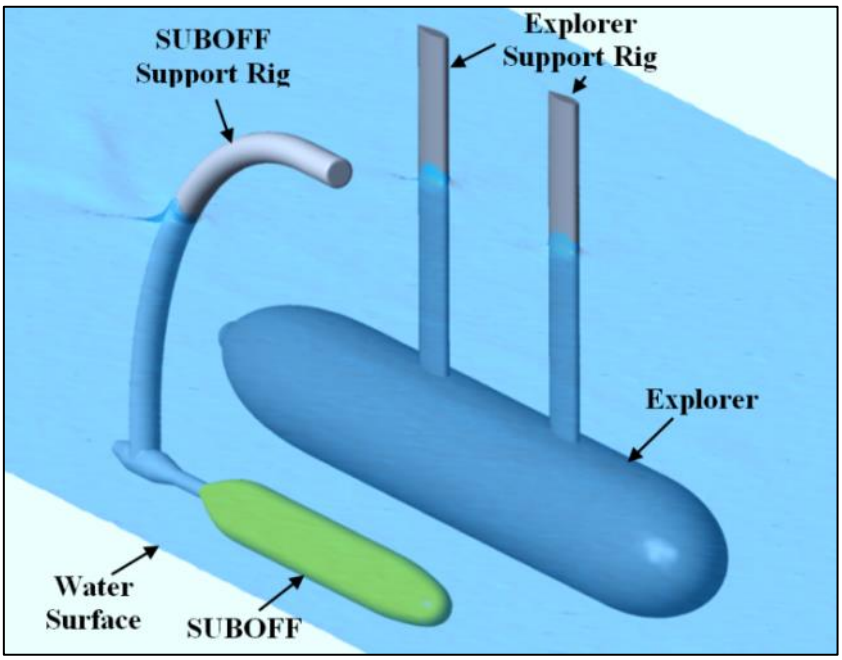

Figure 7.9: CFD model of the experimental setup, including the free surface and support rigs.

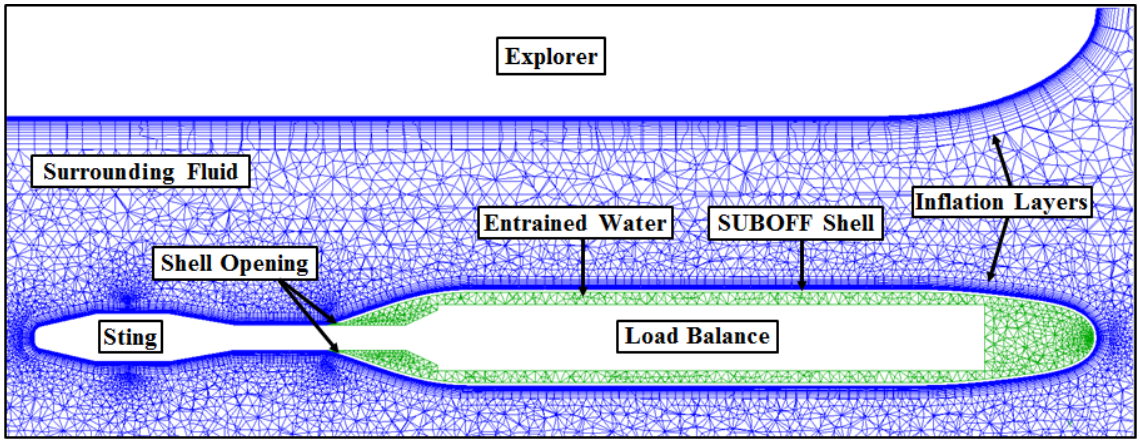

Figure 7.10: Mesh model of the experimental setup with the entrained water within the SUBOFF shell modelled to account for its inertia effects.

7.5.2.1 Overtaking Manoeuvre (Steady-State)

Figure 7.11 shows the CFD predicted longitudinal force, lateral force, and yawing moment coefficients acting on the SUBOFF at different R_{Long} in comparison with the experimental measurements for the diameter ratio of 2.239 at model scale. The figures show good agreement between the CFD and experimental results throughout the R_{Long} range, with the difference being less than the experimental uncertainty as determined using the recommended analysis procedure outlined in ITTC (2002), i.e. 2.252×10^{-4} for the force coefficients and 1.446×10^{-4} for the moment coefficients.

Figure 7.11 also shows the CFD model scale and full-scale predictions with and without towing blockage and free surface effects on the flow around the vehicles. The latter was achieved by extending the domain boundaries six $L_{Explorer}$ away from the $CB_{Explorer}$, with the exception of the outlet which was kept eight body lengths away. The model scale predictions with the extended boundaries indicated substantial blockage effect in the EFD measurements, particularly in the longitudinal force coefficient when the SUBOFF was located at the stern region of the Explorer, i.e. $R_{Long}<0.00$. Thus, the extended domain was used for the remainder of the study, with the reduced domain used only for validation purposes. The model scale and full-scale predictions with the extended boundaries were found to be in close agreement, demonstrating that the Re scaling based on the $L_{Explorer}$ was appropriate for maintaining dynamic similarity between the two scales and thus providing sufficient validation for the CFD model to be extended to the full-scale cases investigated.

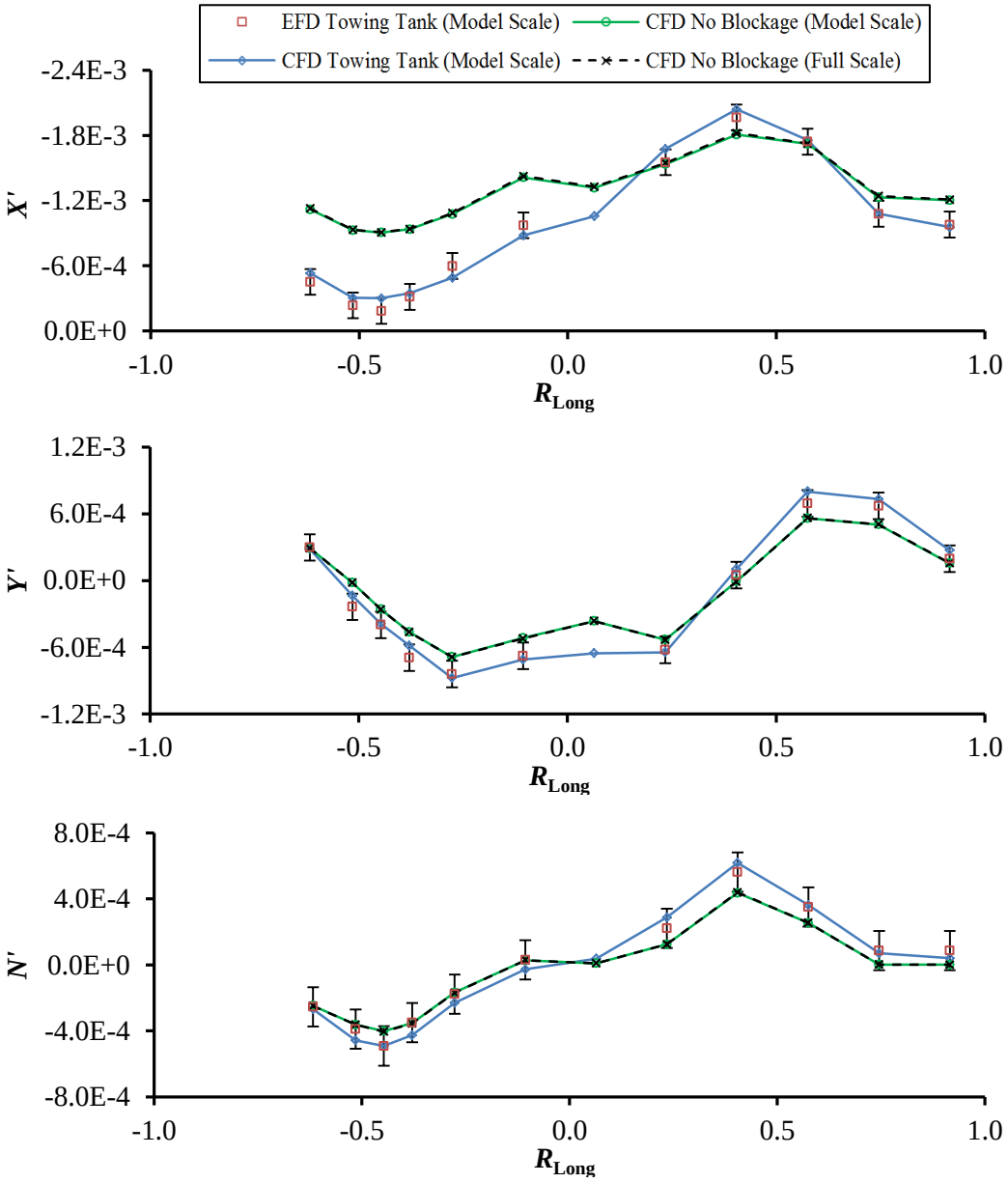

Figure 7.11: CFD and experimental results of the longitudinal force coefficient *X'* (top), lateral force coefficient *Y*' (middle), and yawing moment coefficient *N*' (bottom) on the SUBOFF as a function of longitudinal separation ratio R_{Long} for the diameter ratio of 2.239 at $Re_{SUBOFF} = 2.61\times10^{6}$, $Re_{Explorer} = 4.93\times10^{6}$, and $R_{Lat} = 1.70$. The error bars indicate the experimental uncertainty, i.e. 2.252×10^{-4} for the force coefficients and 1.446×10^{-4} for the moment coefficients.

7.5.2.2 Pure Sway Manoeuvre

Figure 7.12 shows the CFD predicted longitudinal and lateral force coefficients acting on the SUBOFF as a function of time in comparison with the experimental measurements for the

pure sway manoeuvre test case obtained using the HPMM. The figure shows good agreement between the CFD and experimental results, with the differences well within the experimental force and moment coefficient uncertainty, and time and phase differences of less than 0.1s and 8˚ respectively. The time step used for the CFD simulation was 0.02s as the phase and magnitude of the predictions were found to be well within a 1% error margin of the predictions using a time step of 0.005s.

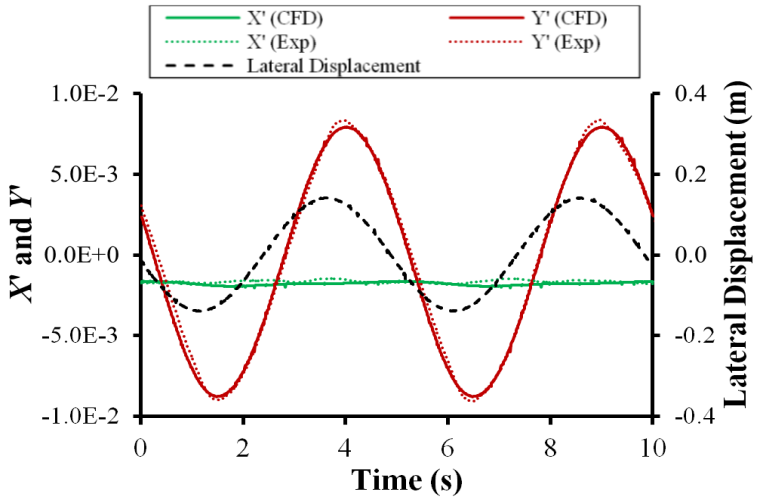

Figure 7.12: CFD and experimental time traces of the longitudinal force coefficient *X'* and lateral force coefficient *Y*' on the SUBOFF for the 0.2Hz pure sway manoeuvre; Re_{SUBOFF} = 2.09×10^6, $Re_{Explorer}$ = 3.95×10^6, and diameter ratio = 2.239.

7.6 Results and Discussion

The following discussion focuses on the influence of the interaction on the SUBOFF's hydrodynamic coefficients for the following two manoeuvres: SUBOFF overtaking the Explorer, and SUBOFF overtaken by the Explorer. The magnitudes of the interaction influence were obtained by subtracting the baseline SUBOFF's hydrodynamic coefficients (at R_{Long} = -2.0) from the results for the range of parameters outlined in Table 7.1. The results are presented as a function of the relative longitudinal position between the two vehicles.

7.6.1 AUV Overtaking Manoeuvre

7.6.1.1 Effect of relative longitudinal position

Figure 7.13 shows the interaction influence on the longitudinal force, lateral force, and yawing moment coefficients of the SUBOFF as it overtakes the Explorer at a constant R_{Lat} of 0.21. As the SUBOFF approaches the Explorer, the stern pressure field of the latter acts to reduce the SUBOFF's longitudinal force coefficient, laterally attracts the SUBOFF, and yaws the SUBOFF bow towards the Explorer. The influence of these interaction effects increases as the SUBOFF progresses forward and peaks at around R_{Long} of -0.4. Thus, the stern region of the submarine presents a high risk of collision for an AUV to operate within, for an AUV maintaining a straight-line overtaking trajectory with no additional control under the influence of the interaction. In the event of collision it is possible for the AUV to lose forward speed and be drawn into the submarine's propeller. The combination of these adverse effects and implications makes it undesirable for an AUV to approach the submarine from the stern.

As the SUBOFF progresses onwards from R_{Long} of -0.4, the interaction influence declines and recovers to the base value at around R_{Long} of 0.0. At R_{Long} of 0.2 onwards, the forward pressure field of the Explorer acts to increase the SUBOFF's longitudinal force coefficient, laterally repel the SUBOFF, and yaw the SUBOFF bow away from the Explorer. The influence of these interaction effects peaks at around R_{Long} of 0.4, and then declines and diminishes at around R_{Long} of 1.5 as the SUBOFF clears away from the pressure field of the Explorer. The trends suggest that an AUV will encounter difficultly in approaching the bow of the submarine as the influence of the interaction acts to repel the AUV as it passes within that region. The interaction influence was found to be minimal around the amidships of the submarine, where its negative pressure field is fairly uniform (see Figure 7.14), thus suggesting a safe region for the AUV to manoeuvre within.

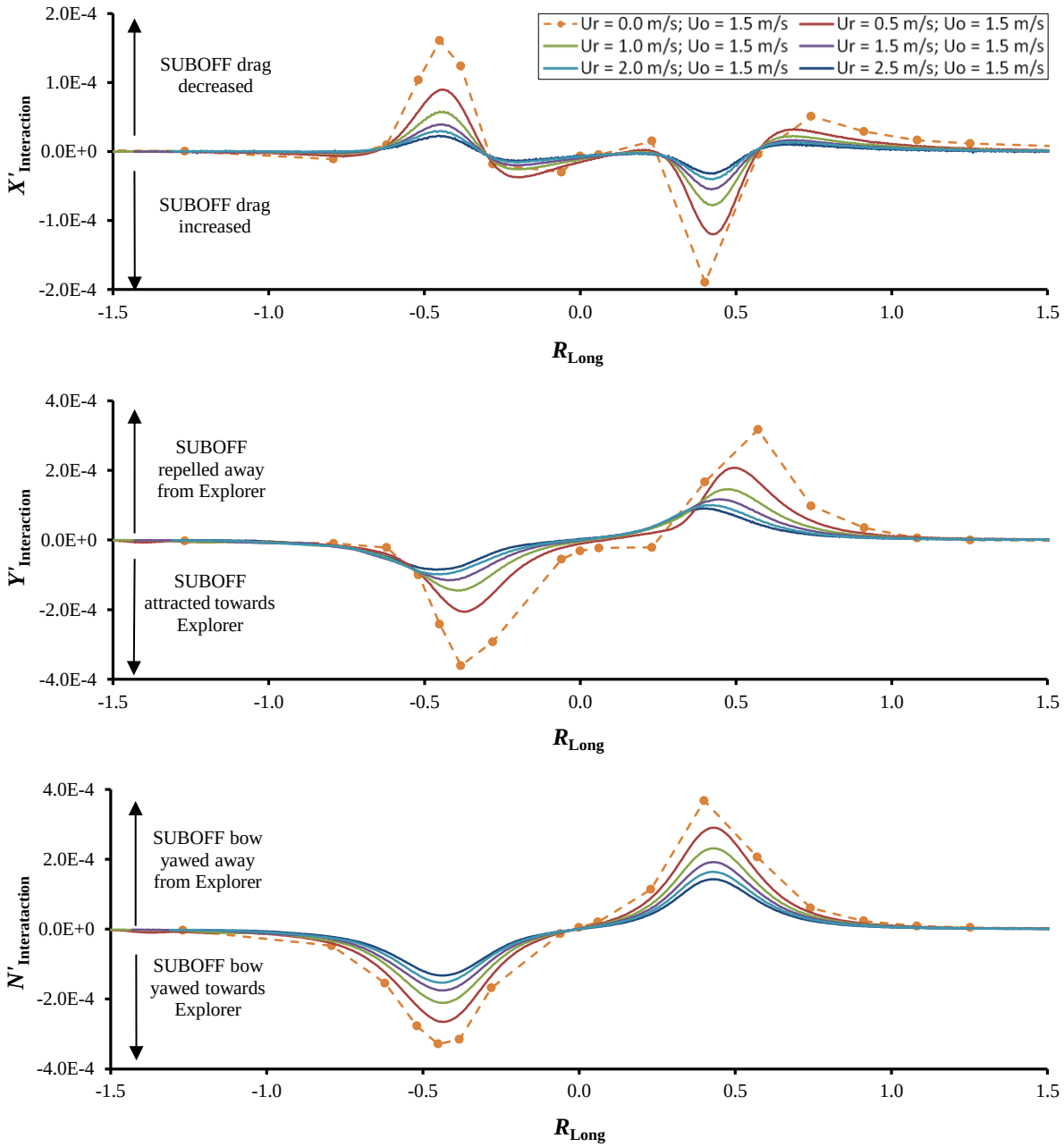

Figure 7.13: Interaction influence on the SUBOFF's longitudinal force coefficient ($X'_{Interaction}$), lateral force coefficient ($Y'_{Interaction}$), and yawing moment coefficients ($N'_{Interaction}$) vs relative longitudinal position (R_{Long}) for the AUV overtaking the submarine at different relative speeds.

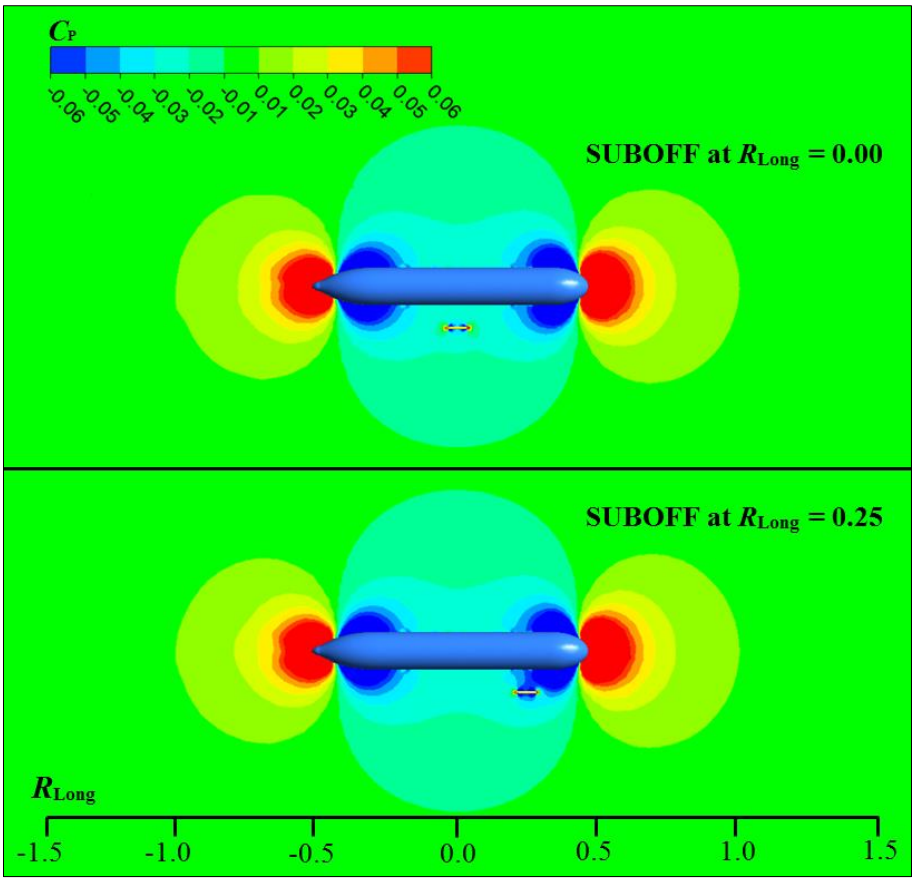

Figure 7.14: Pressure coefficient (C_P) contours of the flow around the SUBOFF and Explorer models at R_{Long} = 0.00 (top) and R_{Long} = 0.25 (bottom); R_{Lat} = 0.15. The pressure coefficient contour range is clipped at ±0.06.

7.6.1.2 Effect of relative speed

Five overtaking velocities were evaluated and compared with the steady-state results at a constant R_{Lat} of 0.21 (see Figure 7.13). The magnitude of the interaction influence reduces as the SUBOFF overtakes at higher relative velocities to the Explorer. This is due to an increase in the SUBOFF pressure field intensity at higher overtaking speeds, thus reducing the pressure difference between the SUBOFF and the Explorer. This suggests that an AUV becomes less susceptible to the interaction influence when overtaking at speeds higher than the submarine. The general trends of interaction influence with respect to R_{Long} at the different overtaking speeds were similar to the findings discussed in Section 6.1(a).

Since an AUV relies on its control planes and propeller for trajectory control, the hydrodynamic coefficients of the fully appended SUBOFF (see Roddy 1990) is used as an

indication of the ability of an AUV to effectively manoeuvre under the influence of the interaction. The following discussion is based on the SUBOFF's yawing moment coefficient, as this determines the tendency of the vehicle to adjust its angle of attack given known control forces. The resultant change in angle of attack then acts to generate the directional thrust and lateral forces required to effectively manoeuvre.

From Figure 7.13, the interaction influence on the SUBOFF yawing moment coefficients in positive and negative directions were found to be at their highest when the SUBOFF maintains its position (U_R = 0 m/s) at R_{Lat} of -0.4 and 0.4; i.e. $N'_{Interaction}$ of -3.3 x 10^{-4} and 3.7 x 10^{-4} respectively. Based on the SUBOFF's hydrodynamic coefficients measured by Roddy (1990), the $N'_{Interaction}$ values are within the maximum yawing moment contribution of the SUBOFF stern rudders (which is approximately 7.0 x 10^{-4} at the maximum rudder angle of 15 degrees). However, the manoeuvrability of the SUBOFF will be extremely limited at these points considering that the maximum angle of attack that can be maintain by the SUBOFF is 2 degrees bow towards and away from the Explorer at R_{Lat} of -0.4 and 0.4 respectively. Above these thresholds, the SUBOFF bow will be increasingly yawed towards the Explorer at the R_{Lat} of -0.4 and in the opposite direction at the R_{Lat} of 0.4 due to the combination of the interaction influence and the hydrodynamic contribution of the SUBOFF barehull. This suggests that it is unlikely for an AUV to safely negotiate the interaction effects around the stern and bow regions of a moving submarine, especially in the case of a recovery operation within these regions.

7.6.1.3 Effect of lateral distance

Figure 7.15 gives the interaction influence on the longitudinal force, lateral force, and yawing moment coefficients of the SUBOFF as it overtakes the Explorer at different R_{Lat}. The forward speeds of the SUBOFF and Explorer are 3.0 m/s and 1.5 m/s respectively (i.e. U_0 = 1.5 m/s, U_r = 1.5 m/s).

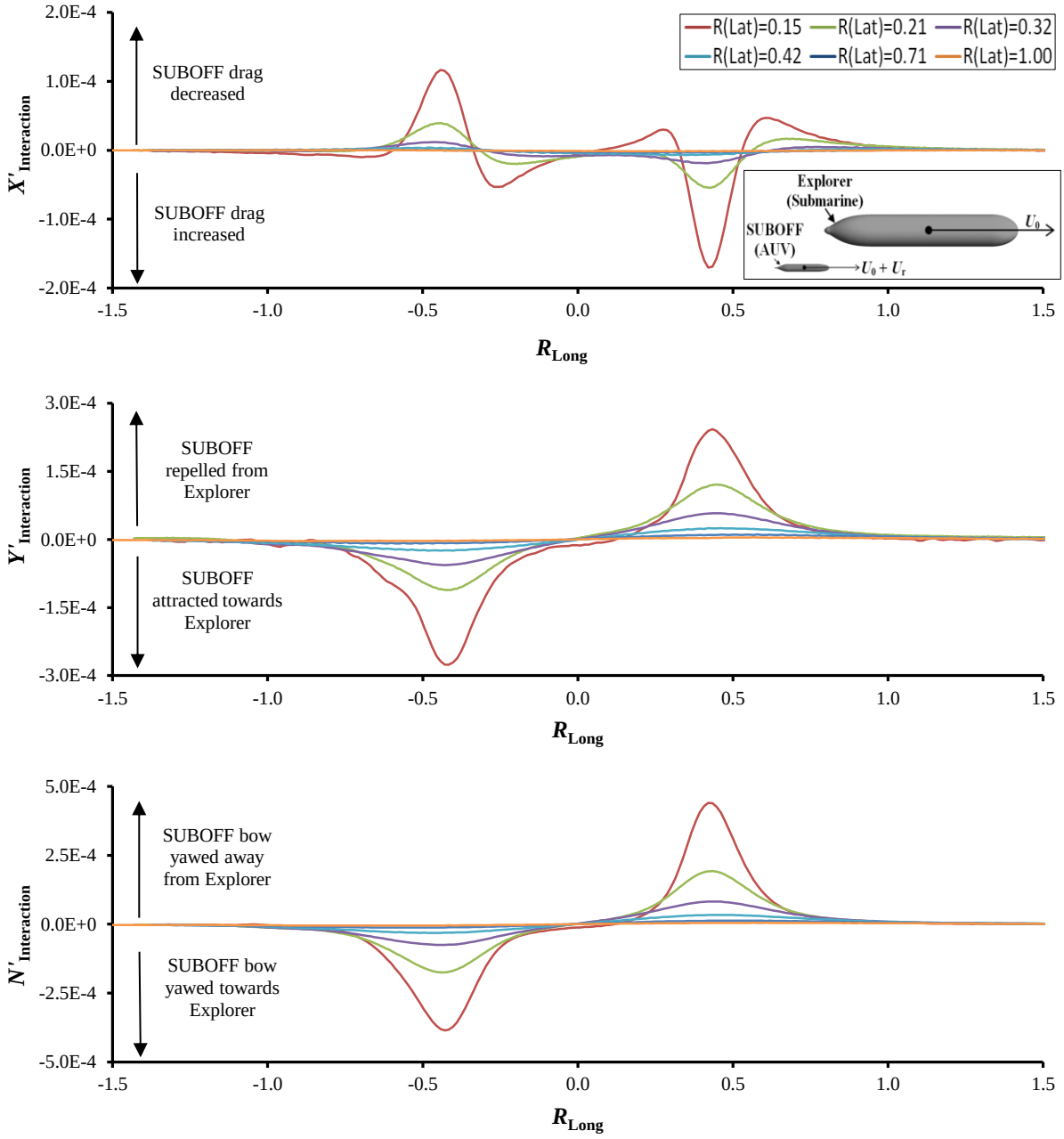

Figure 7.15: Interaction influence on the SUBOFF's longitudinal force coefficient ($X'_{Interaction}$), lateral force coefficient ($Y'_{Interaction}$), and yawing moment coefficients ($N'_{Interaction}$) vs relative longitudinal position (R_{Long}) for the AUV overtaking the submarine at different R_{Lat}. The forward speeds of the SUBOFF and Explorer are 3.0 m/s and 1.5 m/s respectively (i.e. U_0 = 1.5 m/s, U_r = 1.5 m/s).

The interaction influence on the SUBOFF's hydrodynamic coefficients were found to be negligible at R_{Lat} of 1.00, with magnitudes less than 1 x 10^{-5}. As the lateral distance between the vehicles decreased, the interaction influence gradually increased, with the trends against R_{Long} similar to those discussed in Section 6.1(a). The exception are that the peak and trough

of the interaction influence on the SUBOFF's longitudinal force coefficients become more prominent between the R_{Long} of -0.3 and 0.3, as the R_{Lat} reduced from 0.21 to 0.15 (which is approximately 8.0m and 4.5m away from the Explorer hull, respectively). Figure 7.14 shows that the positive and negative pressure fields of the Explorer propagating from the stern and bow, thus the pressure gradient in which the SUBOFF manoeuvres is much greater longitudinally at R_{Lat} of 0.15 alongside the Explorer. Therefore, it is desirable that the recovery operation of an AUV via a capture mechanism to be designed with these changes in mind, either by extending the capture mechanism outside the region adversely affected by the longitudinal force changes, or an AUV control system that is capable of responding sufficiently quickly to the changes in its longitudinal force coefficient in order to maintain its relative position.

Further examination of Figure 7.15 revealed that the increase in the interaction influence on the SUBOFF's lateral force and yawing moment coefficients as R_{Lat} is decreased can be idealised by empirical equations obtained through power regression analysis of the data (see Figure 7.16). However, the general trend of interaction influence on the SUBOFF's drag coefficient as a function of both R_{Lat} and R_{Long} (as discussed earlier) was less observable, thus necessitating that the evaluation of close proximity manoeuvres of such vehicles be carried out through virtual, experimental, or real world testing rather than through empirical models in order to realistically represent the nature of such operations.

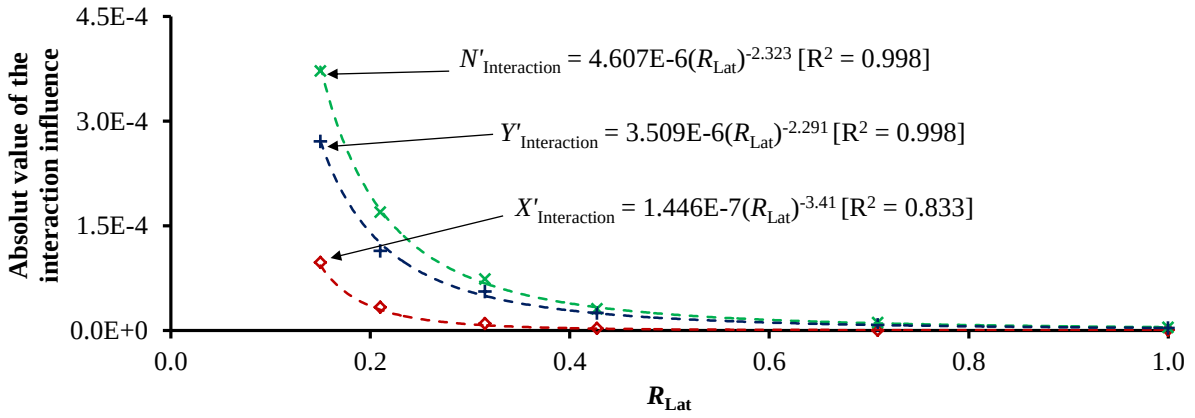

Figure 7.16: Power regression analysis of the interaction influence on the SUBOFF's longitudinal force coefficient ($X'_{Interaction}$), lateral force coefficient ($Y'_{Interaction}$), and yawing moment coefficients ($N'_{Interaction}$) as a function of R_{Lat} for the AUV overtaking the submarine at the R_{Long} of 0.4. The forward speeds of the SUBOFF and Explorer are 3.0 m/s and 1.5 m/s respectively (i.e. U_0 = 1.5 m/s, U_r = 1.5 m/s).

7.6.2 Submarine Overtaking Manoeuvre

7.6.2.1 Effect of relative longitudinal position

Figure 7.17 shows the interaction influence on the longitudinal force, lateral force, and yawing moment coefficients of the SUBOFF as it overtaken by the Explorer at a constant R_{Lat} of 0.21.

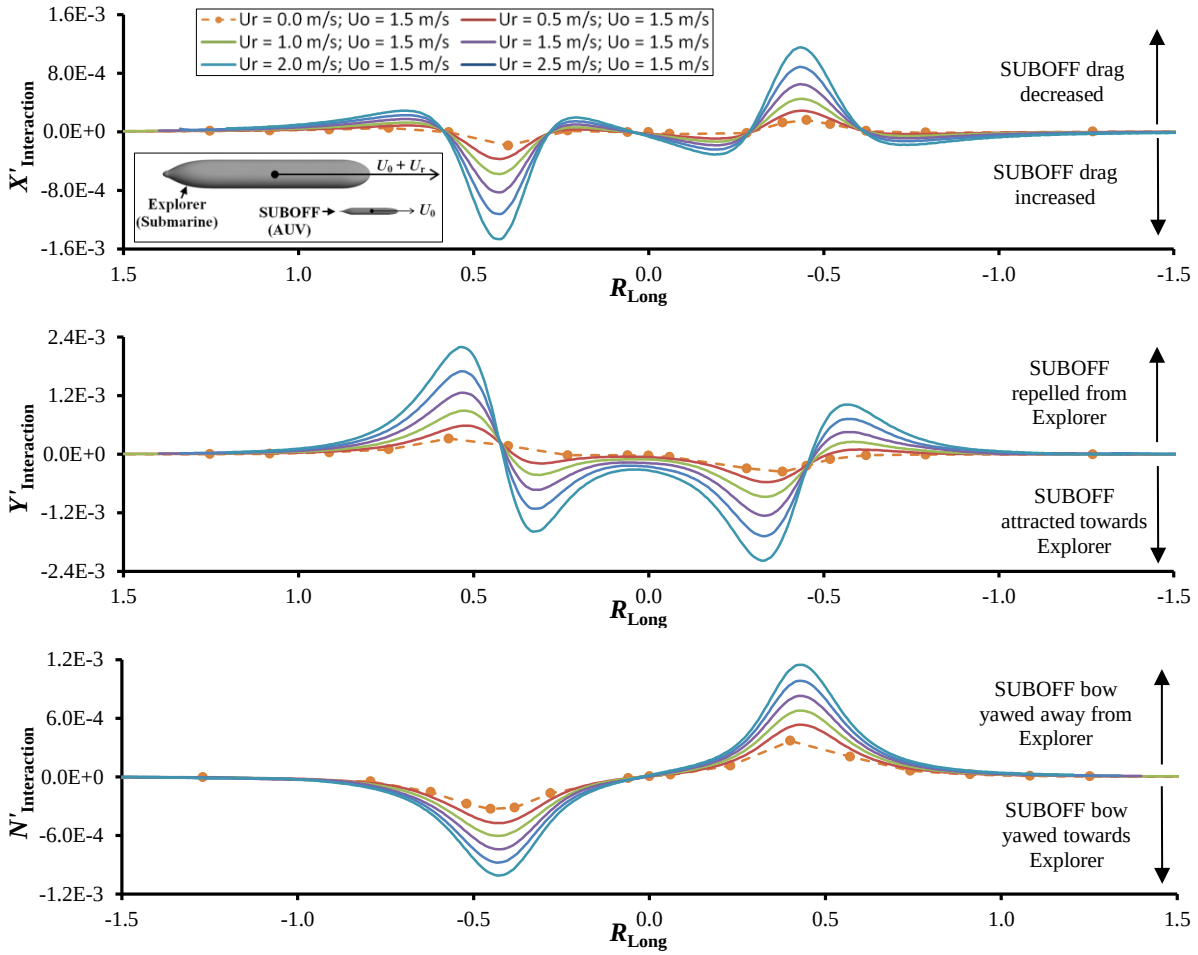

Figure 7.17: Interaction influence on the SUBOFF's longitudinal force coefficient ($X'_{Interaction}$), lateral force coefficient ($Y'_{Interaction}$), and yawing moment coefficients ($N'_{Interaction}$) vs relative longitudinal position (R_{Long}) for the submarine overtaking the AUV at different relative speeds.

As the Explorer approaches the SUBOFF, the interaction influence on the latter is observable at around R_{Long} of 1.6, as it enters the positive bow pressure field of the Explorer resulting in a decrease in its drag coefficient (see Figure 7.14). At around R_{Long} of 0.6, the interaction acts

to increase the SUBOFF drag. This is due the negative pressure field around the bow region of the Explorer progressing onto the SUBOFF's stern, while the bow of the latter remains in the positive pressure field. The increase in drag peaks at around R_{Long} of 0.4, and then declines and recovers to the base value at around R_{Long} of 0.3. Between the R_{Long} 0.3 and 0.0, the SUBOFF experiences a drag reduction due its stern moving into a relatively higher pressure field. At R_{Long} of 0.0, the Explorer pressure field in which the SUBOFF resides is relatively uniform longitudinally and thus the interaction has a minimal effect on the SUBOFF drag. As the Explorer progresses forward, the SUBOFF experiences an increase in drag up to R_{Long} of -0.3, from which point onwards the interaction influence acts to reduce the SUBOFF drag. The drag reduction reaches its maximum value at around R_{Long} of 0.4 and then declines. At R_{Long} of -0.6 onwards the SUBOFF begins to experience an increase in drag which gradually recovers to the base value at an R_{Long} of -1.3 as the Explorer's pressure field clears away from the SUBOFF.

With regards to the interaction influence on the lateral coefficient, the Explorer acts to repel the SUBOFF as it approaches at around R_{Long} of 1.3. The repulsion increases to its maximum value at around R_{Long} of 0.6, before steeply declining to the base value at around R_{Long} of 0.5. Between R_{Long} of 0.5 and -0.5, the interaction acts to attract the SUBOFF. Two prominent troughs of the attraction occur at 0.3 and -0.3. As the Explorer progresses from R_{Long} of 0.4, the interaction acts to repel the SUBOFF from the Explorer, increasing to its maximum value at around R_{Long} of -0.6 and then declines to a negligible magnitude at around R_{Long} of 1.3.

The trend of the interaction influence on the SUBOFF's yawing moment coefficient was found to be similar to that for the AUV overtaking the submarine (see Section 6.1), with the Explorer acting to yaw the SUBOFF bow away and towards the former at the Explorer bow and stern regions respectively.

7.6.2.2 Effect of relative velocity

The interaction influence on the SUBOFF's hydrodynamic coefficients when overtaken by the Explorer at five different relative velocities were evaluated and compared with the steady-state results at a constant R_{Lat} of 0.21 (see Figure 7.17).

The magnitude of the interaction influences is shown to increase as the Explorer overtakes at higher relative velocities to the SUBOFF. While the general trends of the interaction influence were similar to the AUV overtaking the submarine (see Section 6.1), the magnitudes of interaction influence for the submarine overtaking the AUV were much more pronounced. These magnitudes were much more than the steady-state results and exceeded the hydrodynamic contribution of the SUBOFF control planes significantly. This suggests that it is unlikely that an AUV will be able to negotiate the interaction influence or maintain its trajectory when overtaken by a submarine at close proximity without larger control planes, which in turn may create additional interaction issues.

7.7 Conclusion

The paper presents a study conducted to quantify the behaviour of an AUV operating in close proximity to a larger moving submarine at different relative velocities. The investigation utilised CFD and EFD techniques to quantify the longitudinal force, lateral force, and yawing moment coefficients of the AUV with respect to the different relative longitudinal positions between the two vehicles in order to characterise the behaviour of the AUV under the influence of the interaction.

The EFD results from captive model tests were used to validate the CFD model and showed good agreement, thus enabling the latter to be used for further analysis of the interaction under full-scale conditions. The effects of relative velocities on the interaction behaviour were investigated via two manoeuvres: the AUV overtaking the submarine and vice versa, both at a constant relative lateral distance. The effects of lateral distance (R_{Lat}) on the interaction were also investigated for the AUV overtaking the submarine.

The results showed that an AUV becomes less susceptible to the interaction influence when overtaking at speeds higher than the submarine. The general trend of the results showed that the submarine's stern presents a high collision risk region for an AUV to travel within, as the interaction forces and moments tend to attract the AUV towards the submarine. Similarly, the bow region of the submarine is difficult for an AUV to approach as the interaction forces and moments act to repel the AUV away from the submarine. The adverse interaction effects were found to be minimal around amidships of the submarine throughout the different

relative velocities examined, suggesting a safe path for the AUV to approach or depart the submarine laterally around this region.

The interaction influence of the submarine's bow and stern regions on the AUV's lateral force and yawing moment coefficients were found to vary as a power of R_{Lat}, with the two coefficients increasing as the R_{Lat} decreases. General trends of the effects of R_{Lat} on the interaction influence on the AUV's longitudinal force coefficient as a function of R_{Long} were less observable. Therefore, it is desirable that the evaluation of manoeuvres involving close proximity between an AUV and a submarine to be carried out through virtual, experimental, or real world testing of the vehicles rather than through empirical models in order to realistically represent the behaviour of the vehicles.

In the case of the submarine overtaking the AUV, the interaction influence on the latter's hydrodynamic coefficients were found to exceed the ability of the AUV's control planes to compensate. Therefore, it is unlikely that the AUV will be able to maintain its trajectory when approached by a submarine, without larger control planes on the AUV. The larger planes may however cause additional interaction affects.

Further work is being undertaken to extend the current assessment of the interaction behaviour for fully appended models of the AUV and the submarine, in order to identify the interaction influence of the submarine's propeller and sail, and the AUV's appendages. These fully appended vehicle models are to be used in a dynamic manoeuvring simulation to evaluate the operating parameters in which an AUV can safely approach a submarine for recovery, and develop the necessary control algorithms for the AUV to successfully negotiate the manoeuvres.

[Page intentionally left blank]

Chapter 8 :
Summary, Conclusions and Further Work

This chapter provides an overall summary of the thesis and brings together the findings of the individual chapters. It also concludes the findings and outcomes, and discusses the implications of the findings, the limitations, and the recommendations for further research.

8.1 Summary

The focus of this thesis was to investigate the hydrodynamic interaction effects on an unappended Autonomous Underwater Vehicle (AUV) operating in the proximity of a larger moving submarine. In this Chapter, an overall evaluation is made of the results and findings, and their contributions to the research field. Limitations of the study are also discussed and used to provide guidance for future research to increase the understanding of hydrodynamic interaction between underwater vehicles and their impact on AUV-submarine inter-operations.

In addressing the main research question, *What are the hydrodynamic interaction effects on an AUV manoeuvring in the proximity of a larger moving underwater vehicle?*, a review of literature was carried out on operations involving underwater vehicles in proximity and under the influence of the hydrodynamic interaction between the vehicles. While there are investigations linked to technologies and operational considerations for the recovery of an AUV by a moving submarine, the effects of the hydrodynamic interaction between the vehicles has yet to be extensively investigated. Depending on the relative speed and position between the vehicles, the hydrodynamic interaction can cause the AUV to undergo uncontrollable motions which can result in mission failure. Thus, it is important to have a good understanding of the hydrodynamic interaction between the two vehicles in order to develop AUV control systems that can ensure vehicle stability and identify operating parameters in which an AUV can effectively manoeuvre near a submarine.

This thesis focuses only on the unappended configuration of the vehicles. This has allowed the hydrodynamic interaction between the barehulls of the vehicles to be the focal point of the study, thus enabling the investigation of the effects of relative size, position, and velocity between the two vehicles on the interaction behaviour to be unadulterated. The AUV and submarine are represented by the SUBOFF and Explorer geometries respectively.

As there are limited studies on quantifying and characterising the hydrodynamic interaction effects between underwater vehicles in relative motion, an incremental build-up approach to the Computational Fluid Dynamics (CFD) capabilities and analysis was undertaken. These consisted of the steady-state CFD analysis of a single AUV (Chapter 2), verification of the

dynamic meshing methods for CFD modelling of multiple underwater bodies in relative motion (Chapter 3), steady-state analysis of the hydrodynamic interaction effects on an AUV operating in the proximity of a submarine (Chapter 4, 5 & 6), and finally the transient analysis of the hydrodynamic interaction effects on a AUV operating in relative motion and in the proximity of a submarine (Chapter 7). The experimental work carried out to validate and supplement the CFD results are discussed within the respective chapters.

8.2 Conclusions

As a result of the study described in this thesis, the following main conclusions are drawn:

8.2.1 Behaviour of the Hydrodynamic Interaction

Relative longitudinal position: The submarine's stern presents a high collision risk region for an AUV to travel within, as the interaction forces and moments tend to attract the AUV towards the submarine. Similarly, the bow region of the submarine is difficult for an AUV to approach as the interaction forces and moments act to repel the AUV away from the submarine. The bow and stern regions of the submarine also present a challenge to the AUV's control systems due to the steep change in the magnitude of the interaction forces and moments with respect to a small change in relative longitudinal position. The adverse interaction effects were found to be minimal around amidships of the submarine, suggesting a safer path for the AUV would be to approach or depart laterally within that region. These findings are consistent throughout the thesis under model-scale conditions (Chapter 4) and full-scale conditions (Chapters 5, 6 and 7), and for the different diameter and length ratios examined within the respective chapters.

- **Relative lateral position:** The increase in the interaction influence on the AUV's lateral force and yawing moment coefficients was found to follow a power-law relation with the decrease in lateral distance to the submarine. However, a general trend in the increase of the interaction influence on the AUV's drag coefficient as the lateral distance to the submarine decreased was less observable.
- **Extent of the submarine interaction influence on the AUV:** The interaction influence of the submarine on the AUV was found to be unperceivable beyond the

relative distance of one submarine length from the submarine's centre of buoyancy; both laterally and longitudinal.

- **Relative size:** The interaction influence on the longitudinal and lateral force coefficients of the AUV was found to decrease when the size of the submarine was increased while maintaining the same lateral distance ratio (i.e. relative lateral position/submarine length) and length to diameter ratio of the two vehicles. However, the interaction on the yawing moment coefficient remained relatively unchanged thus suggesting that change in the size of the submarine does not necessarily reduce the susceptibility of the AUV to the adverse effects of the interaction.
- **Relative length:** The influence of the hydrodynamic interaction on the AUV as a function of the ratio of the relative longitudinal position to the submarine length was very similar in both magnitude and trend when the AUV operates in the proximity of submarines of different lengths with the same diameter. While a change in the length of the submarine does not reduce the interaction influence on the AUV, the interaction influence evolves over a larger longitudinal distance with an increase in the submarine length and thus allowing more time for the AUV to respond to the change in the interaction influence.
- **Relative motion:** The speed at which the AUV overtakes the submarine from behind was found to have a significant effect on the magnitude of the interaction forces and moments experienced by the AUV. As the overtaking speed of the AUV was increased the interaction influence reduced. Thus, an AUV becomes less susceptible to the interaction influence when overtaking at higher speeds. In the case of the submarine overtaking the AUV, the interaction influence on the AUV's hydrodynamic coefficients was found to exceed the ability of the AUV's control planes to compensate. Therefore, it is unlikely that the AUV will be able to maintain its trajectory when approached from astern by a submarine.
- **Limits of the AUV to manoeuvre under hydrodynamic interaction:** The ability for the AUV's control planes to compensate against the interaction influence at the bow and stern regions of the submarine was found to be extremely limited when the AUV is maintaining the same speed as the submarine. This suggests that it is unlikely for an AUV to safely negotiate the interaction effects around the stern and bow regions of a moving submarine, especially in the case of a recovery operation within these regions.

8.2.2 CFD, Experiments, and Modelling

- **Flow modelling with CFD:** CFD has proven to be a reliable and accurate tool to capture the hydrodynamic characteristics of underwater vehicles (Chapter 2) and the hydrodynamic interaction between them (Chapters 4 to 7), with consistent good agreement against experimental measurements. CFD has also shown to be especially useful to overcome the restrictions of physical experiments (e.g. full-scale investigations, removal of the experimental blockage and mounting strut effects, and overcoming motion restrictions such as overtaking manoeuvres), thus allowing a more extensive investigation of the problem to be conducted. A greater understanding of the hydrodynamic interaction behaviour was also achieved using CFD flow visualisation, showing that the pressure field generated by the vehicles is the dominant mechanism behind the interaction behaviour. However, given the number of variables that can affect the quality of the CFD predictions, it is paramount that the CFD predictions are validated through experimental or trial data. It is also desirable that CFD and experimental work are carried out in conjunction as CFD was also used in this thesis to assist with the design of the experiment. This included predicting the hydrodynamic load on the models which defines the required structural support, measuring equipment, and limits of the experiment. The CFD predictions also provided confidence in the experimental measurements as they are taken.
- **RANS-based turbulence models:** Chapter 2 showed that with a sufficiently fine mesh, appropriate mesh treatment, and simulation conditions matching the experiments, the BSLRSM predictions of the AUV's hydrodynamic coefficients under translation and rotational flow conditions were in good agreement with published experimental measurements. Although the SSTCC predictions were agreeable with the longitudinal force coefficient, they fall outside the experimental uncertainty for both the lateral force and yawing moment coefficients. This suggests the need for BSLRSM when cross-flow separation is present on an underwater vehicle. The superior ability of the BSLRSM over SSTCC to predict the hydrodynamic coefficients of a bluff body in Chapter 2 are also supported by Chapter 3, showing that the BSLRSM predictions of the drag on a sphere over a wide range of Reynolds numbers were consistently closer to published experimental data compared to the SSTCC predictions.

- **Dynamic meshing for bodies in relative motion**: Of the two dynamic meshing methods evaluated in Chapter 3, i.e. ANSYS Meshing Platform (AMP) Remeshing and Immersed Solids Method (ISM), the performance of the AMP Remeshing was found to be far superior for modelling bodies undergoing large positional displacement compared to the Immersed Solid technique in both accuracy and computational effort. The difference in the accuracy performance is due to the capability of the AMP Remeshing to resolve the boundary layer around the bodies. Although the ISM does not require remeshing or a mesh to resolve the boundary layer around each body, it still requires a fine mesh in the fluid domain regions where the body travels. This fine mesh increases substantially with the motion range, and as a result increases the computational time, whereas the AMP Remeshing allows the mesh refinement to be maintained locally around the bodies.
- **Computational Time**: The BSLRSM simulations required 20 percent extra computational time compared to the equivalent SST model, which was considered reasonable in light of the improved results the former provided. The average computing resources used to perform the computations were 8 CPU cores, with a total RAM of 8GB. Both the cluster and standalone PCs were used, with the former primarily employed for steady-state simulations. A standalone PC was used for the transient simulations that involved remeshing in order to reduce the computational time (up to 50% compared to the cluster). The average time for steady-state simulations were 3 to 6 hours while the transient cases took around one week.
- **Experiments:** The experimental work (Chapters 4 to 7) has provided valuable data to validate the CFD predictions and insight into the characteristics of the hydrodynamic interaction between the two vehicles. While the experiments required higher cost and preparation compared to simulations, the experiments required shorter run time and the physics are fully captured as opposed to the CFD predictions where the physics may not have been fundamentally resolved correctly. The co-agreement between CFD and experimental results provides the necessary confidence in simulation models, which in turn substantially reduces the development time of simulation models.
- **Scaling effects:** The investigation of the scaling effects on the hydrodynamic interaction presented in Chapter 5 showed that the hydrodynamic coefficients of the model scale results are identical to the full-scale results based on Reynolds scaling, given that the blockage and mounting strut effects in the experimental setup are

accounted for (in this case through CFD). This provided confidence in the CFD predictions of the hydrodynamic interaction behaviour under full-scale conditions in Chapters 6 and 7.

8.3 Implications of the Research

In this thesis, CFD and experimental work were conducted to investigate the hydrodynamic interaction between the unappended configurations of an AUV operating in close proximity to a moving submarine. This has allowed the hydrodynamic interaction between the barehulls of the vehicles to be the focal point of the study, thus enabling the investigation of the effects of relative size, position, and velocity between the two vehicles on the interaction behaviour to be unadulterated by the influence of the appendages. The results presented not only help designers to develop a deeper insight into the hydrodynamic interaction between underwater vehicles but also as a guide to improve the operations involving multiple underwater vehicles manoeuvring in close proximity and the design of AUV launch and recovery systems on submarines.

There has also been much developmental work done on the methodology and the capabilities of the CFD models to investigate the interaction behaviour. The CFD work explored the effects of y^+ in the near-wall mesh, total thickness of the inflation layers, and model boundary conditions on the CFD predictions to accurately represent the hydrodynamic characteristics of the underwater vehicles. This area has been surprisingly neglected as the majority of CFD studies on torpedo-shaped underwater vehicles (such as the SUBOFF geometry) have focused on methodologies to validate the CFD predictions with very limited discussion on the modelling factors that can affect the predictions.

The CFD work also evaluated the performance of two dynamic meshing methods within ANSYS CFX (i.e. AMP Remeshing and ISM) in modelling underwater bodies in relative motion. Although the algorithms behind the methods have undergone substantial development in recent years, there are currently no existing studies demonstrating their capabilities in modelling multiple bodies in relative motion, let alone their performance in terms of accuracy. Furthermore, the AMP Remeshing method is a beta feature in ANSYS

CFX that has yet to be fully integrated into the software, and thus guiding principles in utilising the method is also discussed (see also Appendix III).

In addition to the innovations in the CFD work, the experimental results are of significant value as there are very few experimental-based studies in the public domain characterising the behaviour of the interaction between such vehicles.

These efforts have resulted in an increase in data quality, overall confidence in the data, reduction in analysis time, and greater understanding of the interaction behaviour that will form the basis and support for further work on fully-appended configurations of the underwater vehicles.

8.4 Further Work

Direct extension of this thesis could lead to the following.

1. Extend the investigation into the interaction behaviour for fully-appended models of the vehicles, enabling comparison against the unappended data in this study in order to identify the interaction influence of the submarine's propeller, sail, and control surface, and the AUV's appendages. The addition of the appendages will make the CFD computations more challenging and require greater computational resource. While the methodology to develop a CFD model of an appended hull is subjected to the same scrutiny as an unappended hull, the former requires the following:
    - mesh and turbulence model sensitivity studies to be carried out independently for each of the appendages (e.g. sail and stern control surfaces) and the hull to ensure that the model is able to capture their individual hydrodynamic characteristics prior to their integration; and
    - mesh and turbulence model sensitivity studies to be carried out for the appended hull as they will affect the interaction between the appendages and hull, and also the development of the sail wake which affects the performance of the stern control surfaces downstream.
2. Investigate the interaction behaviour of the AUV at different incidence angles in proximity to the submarine.

3. Investigate the interaction behaviour of the AUV in the proximity of submarines of different diameters with the same length. The current results and findings are acknowledged as being insufficient to form generalised conclusions about the effects of the change in diameter on the interaction behaviour.
4. Extend the experimental setup for testing of underwater vehicles undergoing longitudinal relative motion. This will allow a more extensive validation study of the CFD prediction of the overtaking manoeuvres between the vehicles.
5. Investigate the performance of emerging mesh-free CFD solutions such as Particle-based method and Finite Pointset method in modelling underwater vehicles in relative motion and the hydrodynamic interaction between them. The mesh density required for adequate accuracy in the predictions for the test cases investigated in this thesis was found to be the main factor in determining the total time of the simulations. Thus, mesh-free solutions may reduce the simulation time considerably while offering similar accuracy.
6. Further develop and trial the ANSYS CFX-MATLAB interface presented in Appendix III for manoeuvring simulations of multiple vehicles in relative motion.

The long term objective of the work will be a dynamic manoeuvring simulation environment that would realistically represent the nature of close proximity operations between underwater vehicles. The work in this thesis provides the foundation to reach this objective.

[This page intentionally left blank]

Bibliography

Ackermann, S., Ranmuthugala, S.D., Widjaja, R., & Anderson, B. 2008, 'Computational Fluid Dynamics of Suboff Submarine with Sail and Stern Appendages', *Proceedings of the Pacific Underwater Defence Technology Conference*, Sydney, Australia.

Acosta, G., Ibanez, O., Curti, H., & Rozenfeld, A. 2007, 'Low-cost autonomous underwater vehicle for pipeline and cable inspections', *Underwater Technology and Workshop on Scientific Use of Submarine Cables and Related Technologies*, pp. 331-336.

Alin, N., Bensow, R. E., Fureby, C., Huuva, T., & Svennberg, U. 2010, 'Current Capabilities of DES and LES for submarines at straight course', *Journal of Ship Research*, vol. 54, pp. 184-196.

ANSYS 2011, *ANSYS CFX 15.0 User Guide*, ANSYS Inc., Pennsylvania.

Beratlis, N., Squires, K. & Balaras, E. 2012, 'Numerical investigation of Magnus effect on dimpled spheres', *Journal of Turbulence*, vol. 13, pp. 1-15.

Bertram, V. 2000, *Practical Ship Hydrodynamics*, Butterworth Heinemann, Oxford.

Blidberg, D.R. 2001, 'The Development of Autonomous Underwater Vehicles (AUV); A Brief Summary', *Proceeding of the IEEE International Conference on Robotics and Automation*, Seoul, Korea.

Brutzman, D.P. 1994, *A Virtual World for an Autonomous Underwater Vehicle*, Naval Postgraduate School, California, USA.

Bryne, K.M. 1998, *Real-Time Modelling of Cross-Body Flow for Torpedo Tube Recovery of The Phoenix Autonomous Underwater Vehicle (AUV)*, Naval Postgraduate School, California, USA.

Currie, J., Gillis, C.B., Carretero, J.A., Dubay, R., Jeans, T., & Watt, G.D. 2014, 'Dynamics of Two Active Autonomous Dock Mechanisms for AUV Recovery', *Transactions of the Canadian Society for Mechanical Engineering*, vol. 38, no. 2, pp. 213-226.

Dajka, S., Godin, P., & Gerber, A. 2007, *Software Design Documentation for a Six-DOF Unsteady Simulation Capability in ANSYS-CFX*, Defence Research and Development Canada, Ottawa.

DARPA 2013, *Hydra Proposers' Day*, Defence Advanced Research Projects Agency, Virginia, USA.

Duda, B.M., Menter, F.R., Hansen, T., & Esteve, M-J. 2011, 'Scale-adaptive simulation of a hot jet in cross flow', *Journal of Physics: Conference Series*, vol. 318, pp. 1-6.

Fedor, R. 2009, *Simulation of a Launch and Recovery of an UUV to a Submarine*, KTH Royal Institute of Technology, Sweden.

Feldmand, J. 1979, *DTNSRDC Revised Standard Submarine Equations of Motion*. David Taylor Naval Ship Research and Development Center, Maryland.

Fell, B. 2009, *Structured Mesh Optimisation of the Fully Appended DARPA SUBOFF Model*, BEng Thesis, Australian Maritime College, Tasmania.

Gallimore, E., Partan, J., Vaughn, I., Singh, S., Shusta, J., & Freitag, L. 2010, 'The WHOI Micromodem-2: A Scalable System for Acoustic Communcations and Networking', *Proceedings of the IEEE Oceans Conference*, Seattle.

Gertler, M. 1950, *Resistance Experiments on a Systematic Series of Streamlined Bodies of Revolution - For Application to the Design of High-Speed Submarines*, DTMB Report C-297, Naval Ship Research and Development Centre, Washington D.C..

Groves, N., Huang, T., & Chang, M. 1989, *Geometric Characteristics of DARPA SUBOFF Models (DTRC Models Nos. 5470 and 5471)*, David Taylor Research Center, Maryland.

Hardy, T., & Barlow, G. 2008, 'Unmanned Underwater Vehicle (UUV) deployment and retrieval considerations for submarines', *Proceedings of the 11th International Naval Engineering Conference*, Hamburg, Germany.

Irani, R.A., Kehoe, D., Spencer, W.W., Watt, G.D., Gillis, C., Carretero, J.A., & Dubay, R. 2014, 'Towards a UUV and Recovery System on a Slowly Moving Submarine', *Proceedings of the Warship 2014: Naval Submarines & UUV*, 18-19 June 2014, Bath, United Kingdom, pp. 93-103.

ISE 2005, *Explorer Autonomous Underwater Vehicle Datasheet*, International Submarine Engineering Ltd., Canada.

ITTC 2002. Testing and Extrapolation Methods: Resistance- Uncertainty Analysis, Example for Resistance Test. 23rd International Towing Tank Conference, Venice, Italy, ITTC Recommended Procedures and Guidelines, Procedure 7.5-0.2-0.2-0.2, Rev.01.

ITTC 2011a, *Practical Guidelines for Ship CFD Applications*, International Towing Tank Conference, Denmark.

ITTC 2011b, *ITTC Symbols and Terminology List*, International Towing Tank Conference, Denmark.

Jayarathne B.N., Ranmuthugala D., Chai S., & Fei J., 2014, 'Accuracy of Potential Flow Methods to Solve Real-time Ship-Tug Interaction Effects within Ship Handling Simulators', *TransNav, the International Journal on Marine Navigation and Safety of Sea Transportation*, Vol. 8, No. 4, pp. 497-504.

Jones, D.A. & Clarke, D.B. 2008, *Simulation of Flow past a Sphere using the Fluent Code*, Defence Science and Technology Organisation.

Joubert, P.N. 2006, *Some Aspects of Submarine Design: Part 2. Shape of a Submarine 2026*, DSTO Report DSTO-TR-1920, Defence Science and Technology Organisation, Melbourne, Australia.

Kadri, U. & Weihs, D. 2014, 'Higher order hydrodynamic interaction between two slender bodies in potential flow', *Journal of Marine Science and Technology*, pp. 1-8.

Kim, S.E., Rhee, B.J., & Miller, R.W. 2013, 'Anatomy of turbulent flow around DARPA SUBOFF body in a turning manoeuvre using high-fidelity RANS computations', *International Ship Building Progress*, vol. 60, pp. 207-231.

Kimball, P., & Rock, S.M. 2011, 'Sonar-based iceberg-relative navigation for autonomous underwater vehicles', *Deep Sea Research Part II: Topical Studies in Oceanography*, vol. 58, no. 11, pp. 1301-1310.

Kriebel, D. 2007. Mooring loads due to parallel passing ships. Naval Facilities Engineering Service Center, Annapolis, Maryland, USA.

Krishnankutty, P., Varyani, K.S. 2004. Force on the mooring lines of a ship due to the hydrodynamic interaction effects of a passing ship. Journal of International Shipbuilding Progress. 51, 194–101.

Lataire, E., Vantorre, M., Delefortrie, G. 2009. Captive model testing for ship to ship operations. Proceedings of the MARSIM '09 Conference, Panama City, Panama.

Leong, Z.Q., Ranmuthugala, D., Penesis, I., and Nguyen, H. 2012, Numerical Simulation of Spheres in Relative Motion Using Dynamic Meshing Techniques, *Proceedings of the 18th Australasian Fluid Mechanics Conference*, Launceston, Australia.

Leong, Z.Q., & Ranmuthugala, D.S. 2012, *Evaluation of The Turbulence Models (BSLRSM, SST, k-ω) Forces and Moments Predictions for Translation and Rotational Motion of The DAPRA SUBOFF*, Australian Maritime College, Tasmania.

Leong, Z.Q., Ranmuthugala, D.S., Penesis, I., & Nguyen, H.D. 2014a 'RANS-based CFD Prediction of the Hydrodynamic Coefficients of DARPA SUBOFF Geometry in Straight-Line and Rotating Arm Manoeuvres', *The Transactions of the Royal Institution of Naval Architects, Part A International Journal of Maritime Engineering*. [Accepted for Publication, 20 September 2014]

Leong, Z.Q., Ranmuthugala, D., Penesis, I., and Nguyen, H. 2014b, 'Scaling and Relative Size Effects on the Hydrodynamic Interaction on an UUV operating close to a

Submarine,' *Proceedings of the Warship 2014: Naval Submarines & UUV*, 18-19 June 2014, Bath, United Kingdom, pp. 105-114.

Leong, Z.Q., Saad, K.A.M, Ranmuthugala, D.S., & Duffy, J. 2013, 'Investigation into the Hydrodynamic Interaction Effects of an AUV Operating Close to a Submarine', *Proceedings of the Pacific 2013 International Maritime Conference*, Sydney, Australia.

Mackay, M. 2013, *Estimation of Submarine Near-Bottom Hydrodynamic Loads and Squat*, Defence Research and Development Canada, Ottawa.

Marshallsay, P.G., & Eriksson, A.M. 2012, 'Use of computational fluid dynamics as a tool to assess the hydrodynamic performance of a submarine', *Proceedings of the 18th Australasian Fluid Mechanics Conference*, Australia, pp. 1-4.

Mawby, A., Wilson, P., Bole, M., Fiddes, S.P., & Duncan, J. 2010, *Manoeuvring Simulation of Multiple Underwater Vehicles in Close Proximity*, SEA (Group) Ltd, United Kingdom.

Menter, F.R. 2009, 'Trends and challenges in modelling complex turbulent flows', *Proceedings of the 14th International Conference on Fluid Flow Technologies*, Hungary, pp. 1-10.

Menter, F.R. 2012, *Turbulence Modelling for Engineering Flows*, ANSYS Inc., Pennsylvania.

Morrison, F.A. 2010, *Data Correlation for Drag Coefficient for Sphere*, Michigan Technology University, Michigan.

Newman, J.N. 1965, *The force and moment on a slender body of revolution moving near a wall*, David Taylor Basin, USA.

Phillips, A.B., Turncock, S.R., & Furlong, M. 2010, 'Influence of turbulence closure models on the vortical flow field around a submarine body undergoing steady drift', *Journal of Marine Science and Technology*, vol. 15, pp. 201-217.

Quick, H., Widjaja, R., Anderson, B., Woodyatt, B., Snowden, A.D., & Lam, S. 2012, *Phase 1 Experimental Testing of a Generic Submarine Model in the DSTO Low Speed Wind Tunnel*, Defence Science and Technology Organisation, Australia.

Remery, G.F.M. 1974, 'Mooring forces induced by passing ships', *Offshore Technology Conference*, Dallas, vol. 2066, pp. 1–20.

Roddy, R.F. 1990, *Investigation of the Stability and Control Characteristics of Several Configurations of the DARPA SUBOFF Model (DTRC Model 5470) from Captive-Model Experiments*, David Taylor Research Center, Maryland.

Rodgers, J., Wharington, J., Tynan, A., & Coxhead, M. 2008, 'A concept for the deployment of unmanned maritime systems from submarines: MURULA integration, impact

modelling and results', *Proceedings of the Undersea Defence Technology Conference*, Sydney, Australia.

Park, J.Y., Jun, B.H, Lee, P.M & Oh, J., 'Development of test-bed AUV ISiMI and underwater experiments on free running and vision guided docking', *Underwater Vehicles*, InTech, Croatia.

Schlichting, H. 1979, *Boundary-Layer Theory*, McGraw-Hill, New York.

Scholz, T. 2011, 'Using Laser Communication Above Water and Underwater', *Sea Technology*, Compass Publications Inc., California, USA.

Smirnov, P.E., & Menter, F.R. 2009, 'Sensitization of the SST Turbulence Model to Rotation and Curvature by Applying the Spalart-Shur Correction Term', *Journal of Turbomachinary*, vol. 131, pp. 1-8.

Sun, J.L. 2006, *Three-Dimensional Thick Boundary Layer Calculation of a Submarine and a Research for Two-Dimensional Free Surface Wave*, Huazhong University of Science and Technology, China.

Taylor, DW. 1909, 'Some model experiments on suction of vessels', *Transaction of the Society of Naval Architects and Marine Engineers*, no. 17, pp. 2–22.

Toxopeus, S. 2008, 'Viscous-flow calculations for bare hull DARPA SUBOFF submarine at incidence', *International Shipbuilding Progress*, vol. 55, pp. 227-251.

Toxopeus S., Atsavapranee, P., Wolf, E., Daum, S., Pattenden, R., Widjaja, R., Zhang, J.T., & Gerber, A. 2012, 'Collaborative CFD exercise for a submarine in a steady turn', *Proceedings of ASME 31st International Conference on Ocean, Offshore and Arctic Engineering*, Brazil, pp. 761-772.

Vaz, G., Toxopeus, S., and Holmes, S. 2010, 'Calculation of manoeuvring forces on submarines using two viscous-flow solvers', *Proceedings of ASME 29st International Conference on Ocean, Offshore and Arctic Engineering*, China, pp. 1-13.

Watt, G.D., Baker, C.R., and Gerber, A.G. 2006, *ANSYS CFX-10 RANS normal force predictions for the series model 4621 unappended axisymmetric submarine hull in translation*, Defence Research and Development Canada, Ottawa.

Watt, G.D., Carretero, J.A., Dubay, R., Mackenzie, M.R. 2011, 'Towards an Automated Active UUV Dock on a Slowly Moving Submarine', *Proceedings of the Warship 2014: Naval Submarines & UUV*, 18-19 June 2014, Bath, United Kingdom, pp. 93-103.

White, F.M. 2003, *Fluid Mechanics*, 5th Ed, McGraw-Hill, New York.

Xie, S., Li, Q., Wu, P., Luo, J., Li, F., & Gu, J. 2014, 'Hydrodynamic Coefficients Identification and Experimental Investigation for an Underwater Vehicle', *Sensors & Transducers*, vol. 164, no. 2, pp. 288-294.

Yoon, H.K., & Rhee, K.P. 2003), 'Identification of hydrodynamic coefficients in ship manoeuvring equations of motion by estimation-before-modeling technique', *Ocean Engineering*, vol. 30, pp. 2379-2404.

Zeng, G.H., & Zhu, J. 2010, 'Study on key techniques of submarine manoeuvring hydrodynamics prediction using numerical method', *Proceedings of Second International Conference on Computer Modeling and Simulation,* China, pp. 83-87.

Zhang, J.T., Maxwell, J.A., Gerber, A.G., Holloway, A.G.L., & Watt, G.D. 2013, 'Simulation of the flow over axisymmetric submarine hulls in steady turning', *Ocean Engineering*, vol. 57, pp. 180-196.

Appendix I:

Uncertainty Analysis of the Experimental Data

The principle values for the uncertainty analysis of the experimental data are presented here. The uncertainty analysis was conducted in accordance with the ITTC guidelines (ITTC 2002), and has been adapted for underwater vehicles.

Model Particulars			
Definition	Symbol	Value	Units
Length between perpendiculars	L_{PP}	1.556	m
Length on waterline	L_{WL}	1.556	m
Length overall submerged	L_{OS}	1.556	m
Diameter of hull	D	0.181	m
Draft even keel	T	0.181	m
Wetted Surface Area - total	S	0.763	m^2
Wetted Surface Area - hull	S_{BH}	0.763	m^2
Wetted Surface Area- appendages	S_{APP}	0.000	m^2
Area Waterplane	A_{WP}	0.240	m^2
Displacement	∇	0.03185	m^3
Block Coefficient	C_B	0.625	-
Waterplane Area Coefficient	C_W	0.852	-
Wetted Surface Coefficient	C_S	3.427	-

Constant			
Gravity	g	9.81	m/s^2
Density - reference	ρ_{ref}	998.6	kg/m^3
Water Temp - test	t	18	deg
Water Density - test	ρ	998.6	kg/m^3
Pulse count	c	600	-
Time based circuitry	Δt	0.1	s
Carriage wheel diameter	D_{CWheel}	0.555	m

Multiple Run Data Set					
Run No.	U (m/s)	Rx (g)	Rx (N)	Cd	$(C\text{d}-C\text{d}_{mean})^2$
1	1.5	346.156	3.396	0.00125	2.71E-12
2	1.5	334.182	3.278	0.00121	1.73E-09

3	1.5	335.185	3.288	0.00121	1.44E-09
4	1.5	367.278	3.603	0.00133	6.08E-09
Mean	1.5	345.700	3.391	0.00125	
Standard deviation					5.55E-05

Single Run Data Set

Run No.	*U* (m/s)	*R*x (g)	*R*x (N)	*Cd*
1	1.5	346.156	3.396	0.00125

Measurement Accuracy and Bias			
Definition	Symbol	Accuracy	Bias Limit
Model Geometry			
Model Length	B_L	1.00E-03	2.00E-03
Carriage Speed			
Pulse Count	B_C	-	2.36E+00
Optical Encoder	B_{C1}	1.00E+00	1.00E+00
AD Converter 1	B_{C2}	1.50E+00	1.50E+00
AD Converter 2	B_{C3}	1.50E+00	1.50E+00
Voltage to Frequency Converter	B_{C4}	2.50E-01	2.50E-01
Wheel diameter	B_D	1.00E-03	1.00E-03
Time Base	$B_{\Delta t}$	1.03E-05	1.03E-05
Velocity	B_U	-	5.65E-03
Tank Water Temperature and Density			
Thermometer reading	B_T	5.00E-01	5.00E-01
Temp-density relationship	B_{P1}	9.20E-02	9.20E-02
Convert temp to density	B_{P2}	7.00E-02	7.00E-02
ITTC density assumption	B_{P3}	3.00E+00	3.00E+00
Density	B_P	-	3.00E+00
Resistance Measurement			
Accuracy of Calibration Weights	B_{RX1}	5.00E-05	5.66E-05
Mass/Voltage relationship SEE	B_{RX2}	3.07E-02	3.07E-02
Load cell misalignment	B_{RX3}	2.50E-01	1.08E-05
AD Converter	B_{RX4}	0.00E+00	0.00E+00
Inclination of model due to speed	B_{RX5}	2.50E-01	1.08E-05
Resistance	B_{RX}	-	3.07E-02
Coefficinet of Total Resistance	B_{CT}	-	4.31E-05
Partial Derivatives			
Partial Derivative - Resistance Coefficient		Symbol	Value
		$\frac{\partial C_T}{\partial L}$	-1.25E-03

	$\frac{\partial C_T}{\partial U}$	-1.67E-03
	$\frac{\partial C_T}{\partial \rho}$	-1.25E-06
	$\frac{\partial C_T}{\partial R_x}$	3.68E-04
Partial Derivative - Velocity		
	$\frac{\partial U}{\partial c}$	7.11E-04
	$\frac{\partial U}{\partial D_W}$	2.36E+00
	$\frac{\partial U}{\partial \Delta t}$	-4.26E+00
Partial Derivative - Density		
	$\left\lvert\frac{\partial \rho}{\partial t}\right\rvert$	1.83E-01

Precision Limit (95% Confidence)		
Precision Limit	Symbol	Value
Multiple Sample Precision Limit	P_{CTM}	5.55E-05
Single Sample Precision Limit	P_{CTS}	1.11E-04

Total Uncertainty - Resistance Coefficient (95% Confidence)			
Uncertainty	Symbol	Value	%Cd
Multiple Sample Total Uncertainty	U_{CTM}	7.03E-05	5.63
Multiple Sample Total Uncertainty	U_{CTS}	1.19E-04	9.54

[Page intentionally left blank]

Appendix II :
Setup of the ANSYS Meshing Platform (AMP) Remeshing Method for Vehicles in Motion

AII.1 Introduction

This appendix outlines the basic concepts of setting and running a simulation of vehicles in motion using the ANSYS Meshing Platform (AMP) Remeshing method in ANSYS CFX. The capability of the AMP Remeshing method is demonstrated through two test cases, i.e.:

- simulation of an AUV undergoing a prescribed motion relative to a larger vehicle, and;
- simulation of an AUV undergoing a motion in response to an external force.

The capability of the AMP Remeshing method is demonstrated through two test cases, i.e.:

- simulation of an AUV undergoing a prescribed motion relative to a larger vehicle, and;

AII.2 Overview of the AMP Remeshing Method

The essential aspect of the AMP Remeshing method is that the mesh in the fluid domain deforms locally around the body as it moves, and re-meshes when the mesh quality is deemed poor. The simulation information from the previous mesh is interpolated into the new mesh. The re-mesh process is summarized in the flowchart given in Figure AII.1.

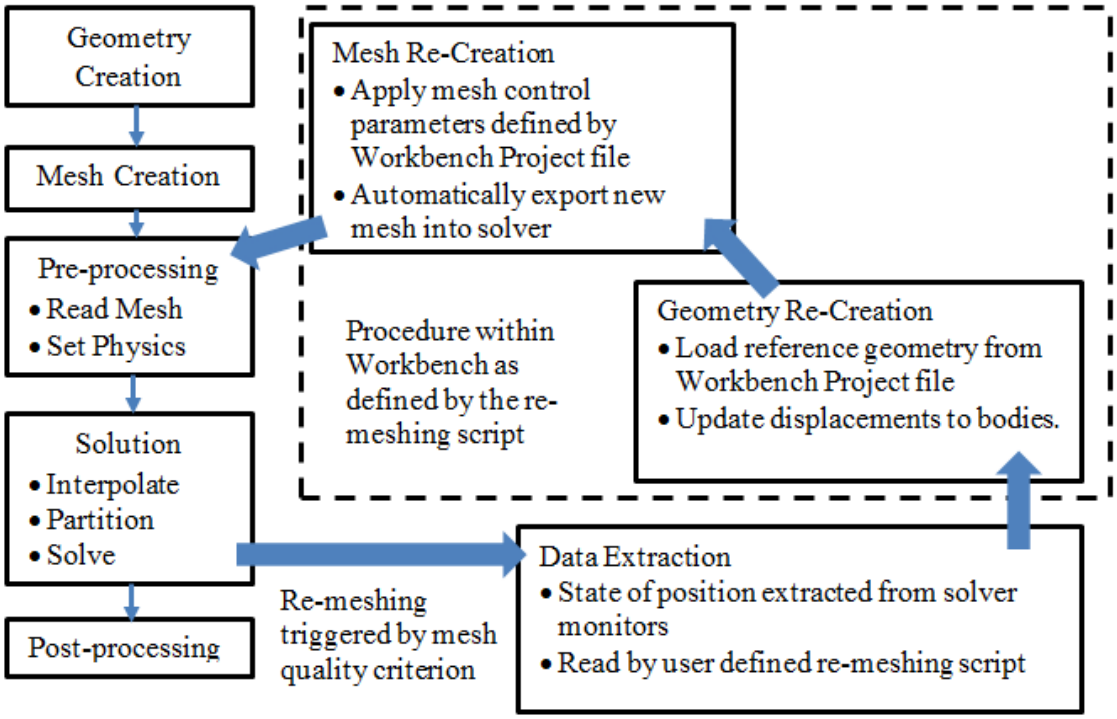

Figure AII.1: Flowchart of the re-mesh method process.

The interrupt conditions, e.g. mesh quality below a predetermined threshold, to initiate remeshing script is defined in the solver control. The process of the remeshing script is summarized into five main parts:

- Part 1: Opens ANSYS WorkBench (WB) project component.
- Part 2: Extract monitor data from current the time step.
- Part 3: Override values of WB parameters for the geometry and mesh based on monitor data.
- Part 4: Recreate geometry and mesh.
- Part 5: Replace mesh, interpolate solution on new mesh, continue solver run.

AII.3 Overview of the Physics Models

The following offers an overview of the governing equations for the physic models used in the simulation architecture.

AII.3.1 Fluid Dynamics Model

The governing equations for the simulation of the flow fluid are based on an *Arbitrary Lagrangian-Eulerian* (ALE) form of the *Navier-Stokes* equations to accommodate the deformation in the mesh, a

feature that is required due to the relative motion between multiple vehicles. The ALE formulation allows the mesh motion to be defined independent of the motion of the fluid being analysed. For the present CFD analysis, the fluid is assumed isothermic, and hence does not consider the thermodynamic equations within the solution algorithm. The conservation equations for mass and momentum are as follows where u_i and u_{mj} represent the velocity field relative to a local coordinate system and the boundary movement of the vehicle respectively (ANSYS 2012; and Dajka & Gerber 2007):

Mass conservation:

$$\frac{\partial \rho}{\partial t} + \frac{\partial \rho \left(u_j - u_{mj} \right)}{\partial x_j} = 0$$

Momentum:

$$\frac{\partial \rho u_i}{\partial t} + \frac{\partial \rho u_i \left(u_j - u_{mj} \right)}{\partial x_j} = F_s + F_b$$

where stable forces on the body F_s is

$$F_s = \frac{\partial p}{\partial x_i} + \frac{\partial}{\partial x_j}\left(\mu \frac{\partial u_i}{\partial x_j} \right)$$

and the apparent body force F_b is

$$F_b = -\rho \frac{d_o^2 R}{dt^2}$$

An additional set of mesh displacement Laplace equations must be added to solve the ALE formulation, and that is the Laplace solutions which diffuse the motion of vehicle's boundary into the interior of the fluid domain. The resulting solution, obtained by integrating over the time interval, allows for the extraction of the mesh velocity u_{mj}. The set of Laplace equations have the form:

Mesh displacement equations:

$$\frac{\partial \rho}{\partial x_j}\left(\Gamma \frac{\partial x_i'}{\partial x_j} \right) = 0$$

where

$$x_i' = x_i - x_i^0$$

The displacement diffusion coefficient Γ can be a function of near wall distance, or mesh volume size.

AII.3.2 Rigid Body Dynamics Model

The equations of motions to predict the motion response of the vehicle are based on a translating-rotating coordinate system fixed to the vehicle. The general equations of motion as follows:

Sum of forces:

$$\sum F = m\dot{u}_G$$

Acceleration of the centre of gravity,

$$\dot{u}_G = \left(\dot{u}_O\right)_{xyz} + \omega u_O + \dot{\omega} r_G + \omega\left(\omega r_G\right)$$

Applied moments around about a point *O* on the body gives,

$$\sum M_O = \left(\left[I\right]\alpha\right)_{xyz} + \left(\left[I\right]\omega\right)\omega + + r_G m\dot{u}_G$$

where

$$[I] = \begin{bmatrix} I_{xx} & -I_{xy} & -I_{xz} \\ -I_{yx} & I_{yy} & -I_{yz} \\ -I_{zx} & -I_{zy} & I_{zz} \end{bmatrix}$$

The product of inertia, [*I*] is evaluated at the centre of gravity of the body.

The system of equations to be solved to track the motion of the body based on the axial (*x*-axis), lateral (*y*-axis), and normal (*z*-axis) forces are as follows,

$$m\left[\dot{u} - x_G\left(q^2 + r^2\right) + y_G\left(pq - \dot{r}\right) + z_G\left(pr + \dot{q}\right)\right] = X_{CFD} + X_S + X_P$$
$$m\left[\dot{v} - y_G\left(r^2 + p^2\right) + z_G\left(qr - \dot{p}\right) + x_G\left(qp + \dot{r}\right)\right] = Y_{CFD} + Y_S + Y_P$$
$$m\left[\dot{w} - z_G\left(p^2 + q^2\right) + x_G\left(rp - \dot{q}\right) + y_G\left(rq + \dot{p}\right)\right] = Z_{CFD} + Z_S + Z_P$$

Similarly, the system of equations based on the rolling (*x*-axis), pitching (*y*-axis) and yawing (*z*-axis) moments are,

$$I_x\dot{p} - I_{zx}\dot{r} - I_{xy}\dot{q} - \dot{I}_x p - \dot{I}_{zx} r - \dot{I}_{xy} q + m\left[y_G\dot{w} - Z_G\dot{v}\right] = K_{CFD} + K_S + K_P$$
$$I_y\dot{q} - I_{xy}\dot{p} - I_{yz}\dot{r} + \dot{I}_y q - \dot{I}_{xy} p - \dot{I}_{yz} r + m\left[z_G\dot{u} - x_G\dot{w}\right] = M_{CFD} + M_S + M_P$$
$$I_z\dot{r} - I_{yz}\dot{q} - I_{zx}\dot{p} + \dot{I}_z r - \dot{I}_{yz} q - \dot{I}_{zx} p + m\left[x_G\dot{v} - y_G\dot{u}\right] = N_{CFD} + N_S + N_P$$

This results in a matrix system:

$$\begin{bmatrix} m & 0 & 0 & 0 & mz_G & -my_G \\ 0 & m & 0 & -mz_G & 0 & mx_G \\ 0 & 0 & m & my_G & -mx_G & 0 \\ 0 & -mZ_G & my_G & I_x & -I_{xy} & -I_{zx} \\ mz_G & 0 & -mx_G & -I_{xy} & I_y & -I_{yz} \\ -my_G & mx_G & 0 & -I_{zx} & -I_{yz} & I_z \end{bmatrix} \begin{bmatrix} \dot{u} \\ \dot{v} \\ \dot{w} \\ \dot{p} \\ \dot{q} \\ \dot{r} \end{bmatrix} = \begin{bmatrix} X_{RHS} - X_{LHS} \\ Y_{RHS} - Y_{LHS} \\ Z_{RHS} - Z_{LHS} \\ K_{RHS} - K_{LHS} \\ M_{RHS} - M_{LHS} \\ N_{RHS} - N_{LHS} \end{bmatrix}$$

The solution of the matrix system results in estimates at the new time level of accelerations ($\dot{u}, \dot{v}, \dot{w}, \dot{p}, \dot{q}, \dot{r}$), which in turn with the time step known allow for calculation of velocities (*u, v, w, p, q, r*). Finally, the auxiliary derivatives in the inertial frame ($\dot{x}_O, \dot{y}_O, \dot{z}_O, \dot{u}_O, \dot{v}_O, \dot{w}_O, \dot{\phi}, \dot{\theta}, \dot{\psi}$) is then integrated to obtain the new position and angular movement ($x_O, y_O, z_O, \phi, \theta, \psi$).

AII.4 Geometry Creation

AII.4.1 Defining the *projectname*

First, a *projectname* is specified for the WorkBench project archive, i.e. *projectname.*wbpj.
The *projectname* becomes the first part of the name for the files the simulation creates and is needed as a reference link between the WorkBench module and the ANSYS CFX solver for the remeshing option to work.

When defining the *projectname*, the following points must be followed due to the characteristics of the Linux operating system and the MATLAB scripts used in the AMI:

- The *projectname* is case-sensitive hence references to it must be identical.
- The first letter must be alphabetical and not be a numeral digit, special character or space.
- The *projectname* must not contain space or special character including '_'.

AII.4.2 Workbench Setup

The ANSYS Workbench is used to define the geometry and mesh model. For this, the *Geometry and Mesh* module (see Figure AII.2) is used which consists of the DesignModeler and ANSYS Meshing Platform (AMP). The *Geometry and Mesh* module must be the only module existing within the Workbench and must be the first module referenced, i.e. 'A' for the remeshing option to work.

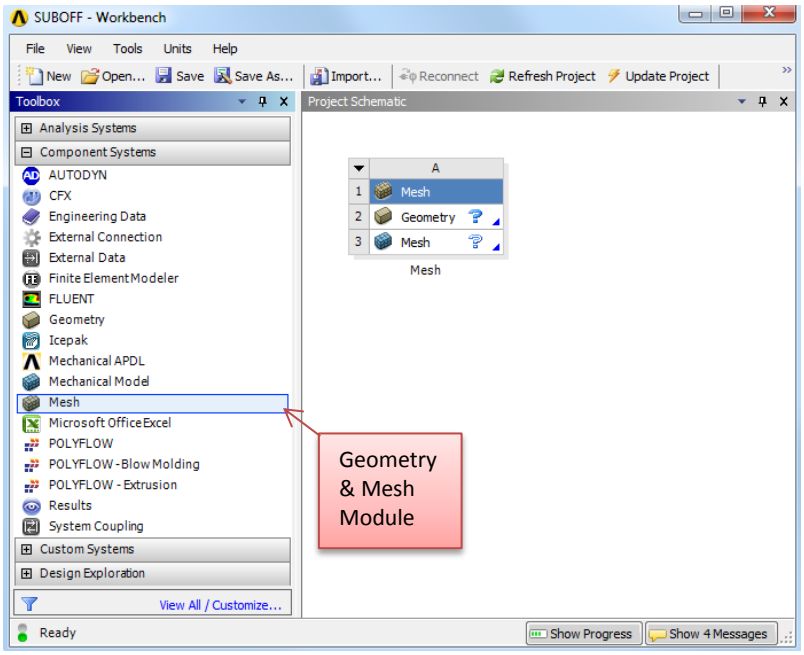

Figure AII.2: Workbench layout with the geometry and mesh module

AII.4.3 Defining the Geometry Model using DesignModeler

Importing Geometry of the Vehicle

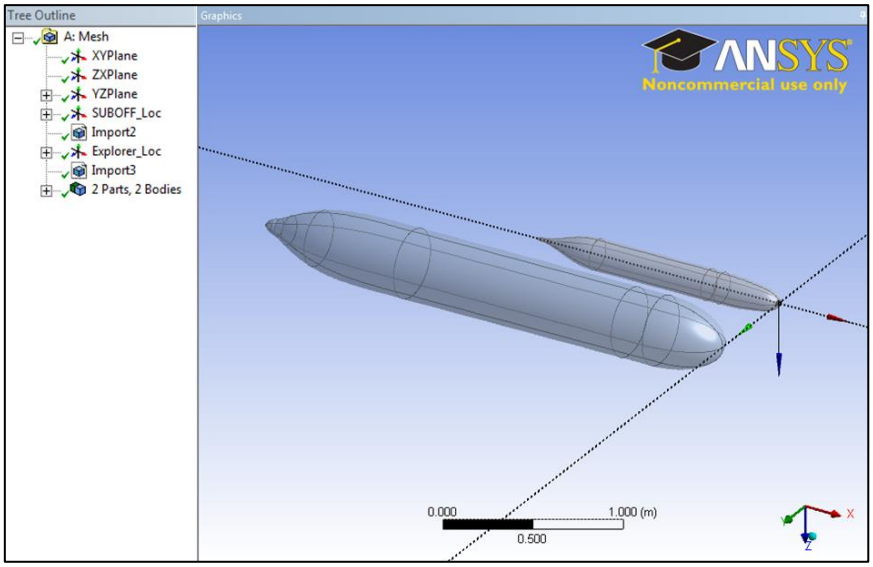

Figure AII.3: Vehicles at their respective base plane

An independent plane for each of the vehicle must first be created to allow them to move independently of each other during simulation. The geometries of the vehicles are then imported onto their respective plane (see Figure AII.3). For the geometries of the vehicles, it recommended that:

- The geometries are imported as 'Frozen'.
- The import functions, 'clean bodies' and 'heal bodies', are disabled to avoid unexpected changes to the geometry, e.g surfaces. Imported geometries should always be checked for consistency with the original geometry.
- The surface of the vehicle geometry should be divided into sub-faces as oppose to a single surface. This substantially reduces the meshing time as the sub-faces guide the meshing algorithm in resolving the geometry.
- The *STEP* (.stp) format is recommended for the imported geometries as the format retains a higher degree of information and quality compared to the other formats supported. Alternatively, if the geometries were created using DesignModeller, ANSYS's proprietary format, *ANSYS Geometry Database* (.agdb) offers equal quality.
- The geometry quality should be as high as possible and also realistic in shape. If needed, DesignModeler does have repair tools for geometry and works reasonably well. However, they should be avoided and if used, care is advised as they can cause undesired changes to the geometry.

<u>Parameterising the Geometry for Remeshing</u>

The parameterising process consists of these general steps (see Figure AII.4):

i. Click the box next to the parameterisable variable of the geometry. The box will be denoted with the 'D' symbol which indicates that parameterisation of the variable is enabled.
ii. In the prompt, specify the parameter name.
iii. The parameters can then be checked, modified and renamed as necessary within the Parameter Manager interface as shown in Figure AII.5.

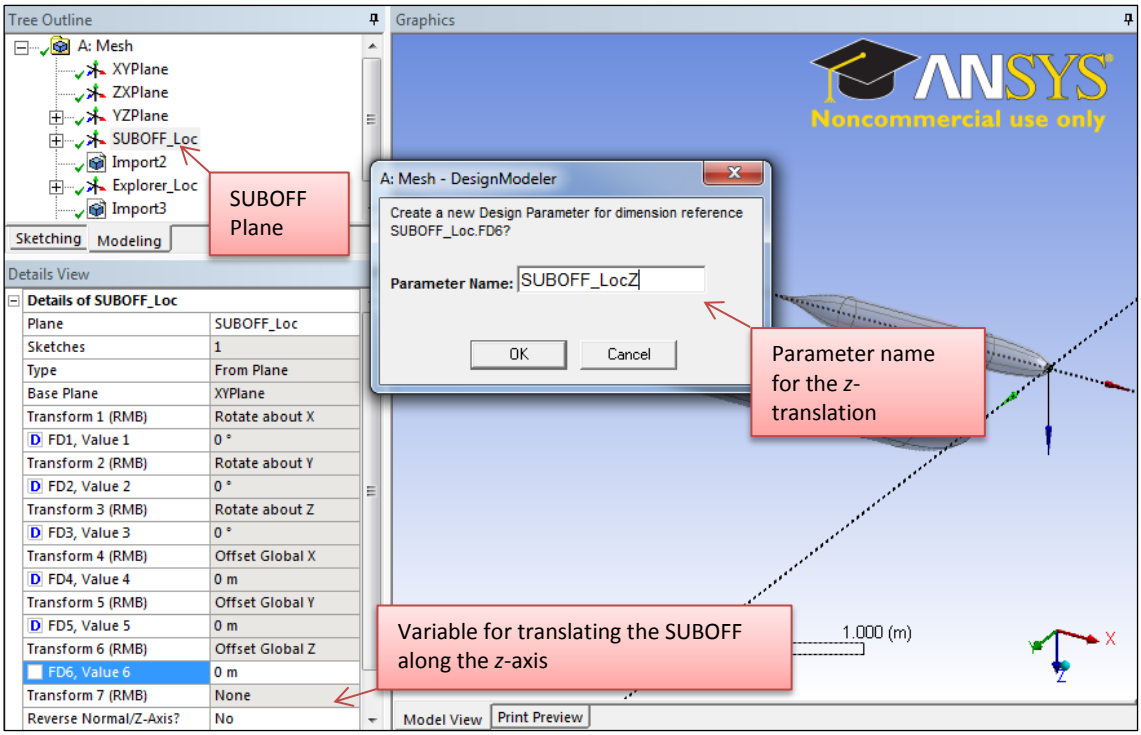

Figure AII.4: Parameterisation of the geometry variables

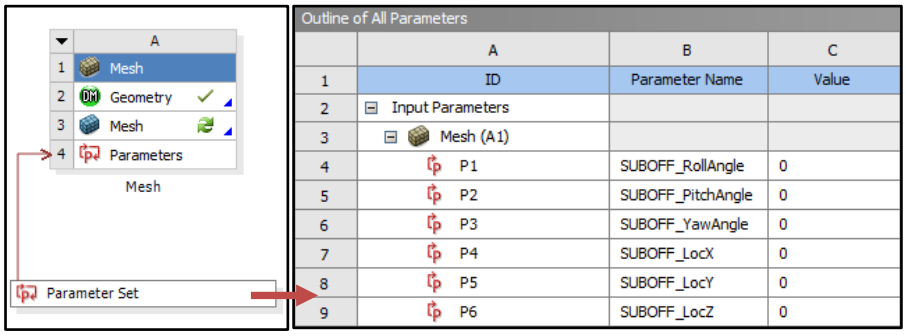

Figure AII.5: Parameter set of the geometry model

Parameterising allows the geometry components to undergo transformation (e.g. translation and rotation) during simulation. While parameterising the model, special attention must be given to the parameter names where the names of the parameters must be identical to the names of the solver monitor data. This creates the necessary reference links between the geometry components and the solver as required by the remeshing process. It is noted that:

- parameter values transferred do not taken into account the units, and
- the same steps to parameterise the geometry model can be used to parameterise the mesh model.

<u>Creating the Fluid Domain</u>

The profile for the fluid domain is created and then extruded as a frozen body (see Figure AII.6). Unless the fluid domain size is made to replicate a physical dimension, it is advisable that the fluid domain boundaries should be sufficiently far away from the vehicles to:

- Avoid boundary effects on the fluid and pressure fields of the vehicles.
- Allow the mesh deformation, due to the vehicle motions, to be absorbed by the larger mesh elements away from the vehicle. This substantially reduces the number of remeshing events required during simulation.

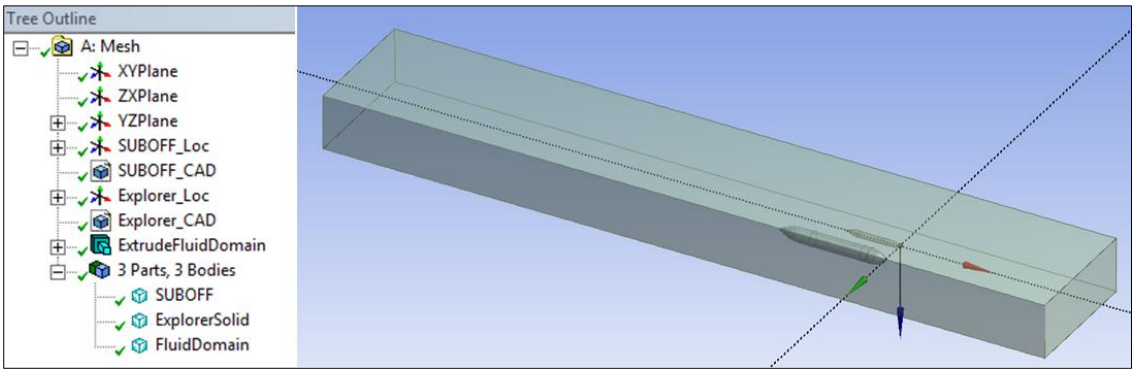

Figure AII.6: Extruded fluid domain

Subdividing the Fluid Domain to Aid the Remeshing Process

For the stability and efficiency of the remeshing process, it highly recommended that the fluid domain be subdivided into the regions around the vehicles and the main fluid domain, especially when inflation layers are used around the vehicles. This allows:

- The mesh within the vehicle subdomains to be rigid, i.e. no deformation occurs, thus maintaining the mesh quality around the vehicles and preventing the inflation layers and surrounding mesh, which are small in volume, from skewing or collapsing into negative volume elements while the vehicles are in motion.
- The majority of the mesh deformation to be absorbed by the mesh in the main fluid domain. Since the larger elements away from the vehicle regions are able to absorb more deformation, this allows a higher degree of vehicle motion before mesh quality is compromised, thus substantially reducing the number remeshing event for the simulation.

The subdividing process of the fluid domain consists of these general steps:

i. Create the sketch profile of the subdomain around a vehicle, e.g. a box-shaped domain as shown in Figure AII.7.
ii. Extrude the sketch as Frozen to form a body.
iii. Subtract the subdomain from fluid domain with Preserve Tool Bodies-Yes.
iv. Subtract the vehicle from the subdomain with Preserve Tool Bodies-No.

For CFD simulations, only the fluid around the vehicles is of interest. The subtract steps above are to remove the solid volume of the vehicles from the fluid domain.

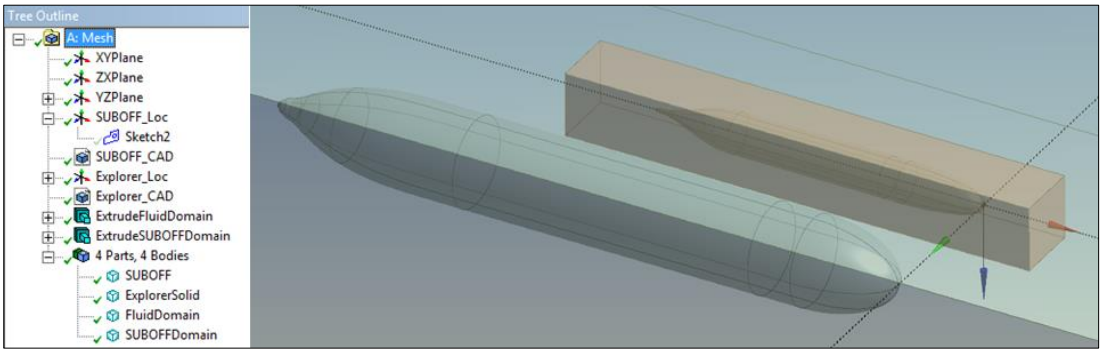

Figure AII.7: Extruded SUBOFF subdomain

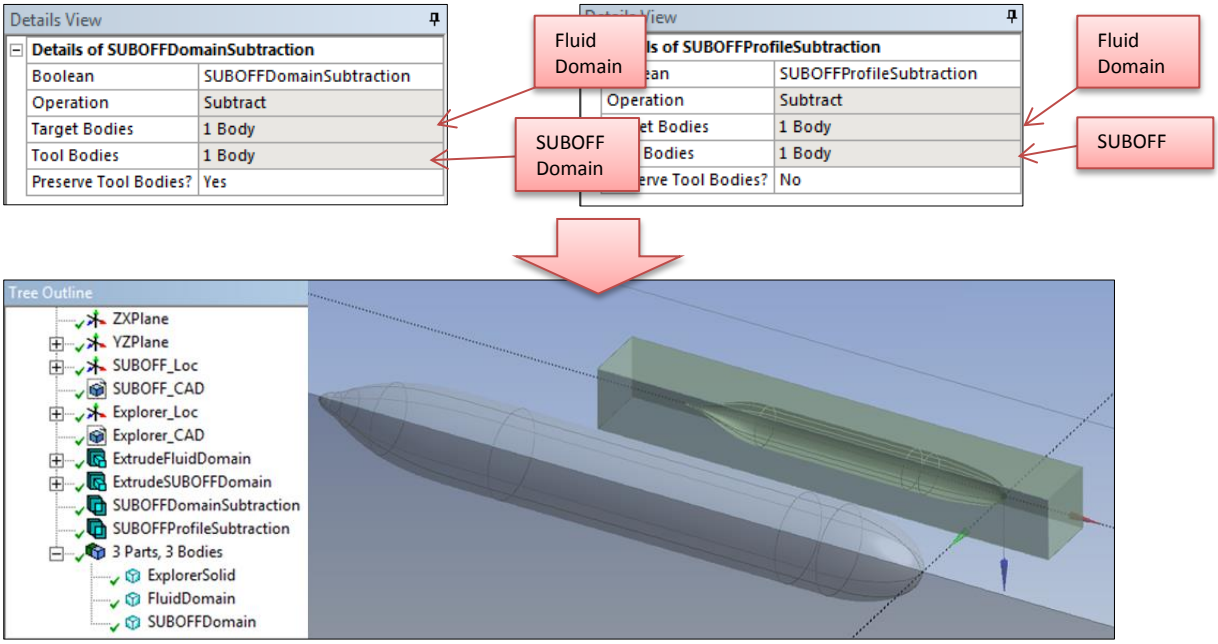

Figure AII.8: Subdivision of the fluid domain for the SUBOFF subdomain

The subdividing domain process for the SUBOFF is repeated for the Explorer. Figure AII.9 shows the final geometry model.

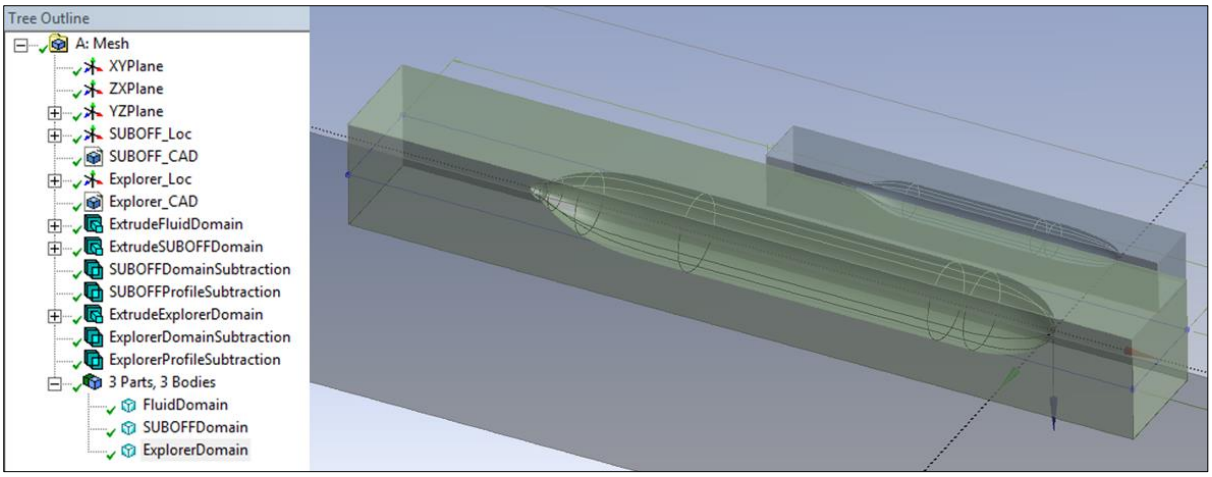

Figure AII.9: Completed geometry model of the SUBOFF and Explorer

A box is preferred for the subdomain shape over a shape with curvature, e.g. cylinder. With the box subdomain, the *Advanced Size Function – Proximity* to be used without the *Curvature* option. This takes half the remeshing time compared to when *Curvature* is used. Even though the actual remeshing time has been substantially reduced to less than a minute by the option to remesh only the fluid domain while leaving the subdomains unchanged during a remeshing event, reducing the remeshing time further by half is desired as the total remeshing time is compounded by the number of remeshing events in a simulation.

As for the size of the subdomain, its boundaries should be at least a body diameter away from the vehicles to allow sufficient inflation layers and mesh elements to reside within the subdomain.

Naming the Geometry Features

The last step to the geometry model is to define the names for the features of the geometry using the named selection option, e.g. the surfaces of the geometry, the boundaries of the fluid domain, and the interfaces of the subdomains. Naming the features is optional but it does substantially simplify the mesh generation process and simulation setup by allowing the geometry features to be referenced by the specified names.

AII.5 Creating the Mesh Model using ANSYS Meshing Platform (AMP)

AII.5.1 General

In order to reduce the remeshing time and the interpolation error caused by a remeshing event, only the main fluid domain is remeshed leaving the mesh inside the subdomains untouched. The general process in creating the mesh model consists of creating the mesh of the subdomains independently and lastly leaving only the meshing setup of main fluid domain within WorkBench for the remeshing event.

Prior to creating the mesh, the following change is recommended in order to speed up the meshing process:

- Open the AMP module and go to *Tools>Options>Meshing>Meshing>Number of CPUs>* 7, if the PC has 8 cores available.

The recommended number of CPUs should be 1 or 2 less than the available cores on a PC. This is to allow at least 1 core available for the operating system and background applications in order to prevent a bottleneck of performance. The solver needs to sync all partitions for each solution loop hence the computational speed limited by the slowest partition; i.e. a partition will take longer to solve if it shares a CPU with the operating system and if the combined load on the CPU is close to 100%.

AII.5.2 Creating the Mesh

SUBOFF Subdomain

i. Suppress the main fluid domain and Explorer subdomain, leaving only the SUBOFF subdomain active.
ii. General mesh settings (unless specified, default used):
    - Solver preference > CFX
    - Advanced Size Function > On: Curvature
    - Smoothing > High (Improves mesh angle quality)
    - Minimum Size > 0.005m (Optimal value for the SUBOFF shape without compromising force predictions. Smaller value will increase mesh density substantially)
iii. Specify the face sizing for the SUBOFF surface. One tenth of the vehicle diameter gives reasonably good prediction without creating excessive mesh elements. The curvature advanced function will automatically refine the mesh around surfaces with high curvature up to 18^0 accuracy of the geometry or up to the min size limit of 0.005m as specified in the general mesh settings.
iv. Specify the inflation prism layers for the SUBOFF surface (e.g. see Figure AII.10):
    - Use total thickness option for more uniform prism layers

- Specify total thickness equivalent to the boundary layer (BL) thickness. For a good estimate of the thickness, use 0.16(*VehicleLength*)/ $Re_{Length}^{1/7}$ which is an estimate of the thickness for a turbulent BL on a flat plate. The prescribed total thickness should never be less the estimated thickness as this will 'squash' the predicted boundary layer and produce spurious results.
- For an emphasis on computational speed with reasonable accurate predictions, there should be at least 15 layers in the boundary layer and the y^+ of the first layer thickness should be well within the log layer, e.g. around 30. For example, Re_{Length} at $2.1x10^6$ with a prism growth rate of 1.2 gives a maximum thickness of 0.04m and 15 prism layers for the SUBOFF. The settings are shown in Figure AII.11.

v. Specify the face sizing for the surfaces of the subdomain that will interface with the surfaces of the fluid domain. The face size for the interface is determined by meshing the subdomain with the settings above and measuring the length of the smallest element on the surface. This ensures a uniform element face size on the interface.

vi. Specify the body sizing for the subdomain. The body size is recommended to be same as the face size determine in step v.

vii. Generate mesh.

viii. Export mesh as *SUBOFFDomain.meshdat*

Details of "Inflation" - Inflation	
Scope	
Scoping Method	Geometry Selection
Geometry	1 Body
Definition	
Suppressed	No
Boundary Scoping Method	Named Selections
Boundary	SUBOFF
Inflation Option	Total Thickness
Number of Layers	15
Growth Rate	1.2
Maximum Thickness	4.e-002 m
Inflation Algorithm	Pre

Figure AII.10: Inflation prism layers settings

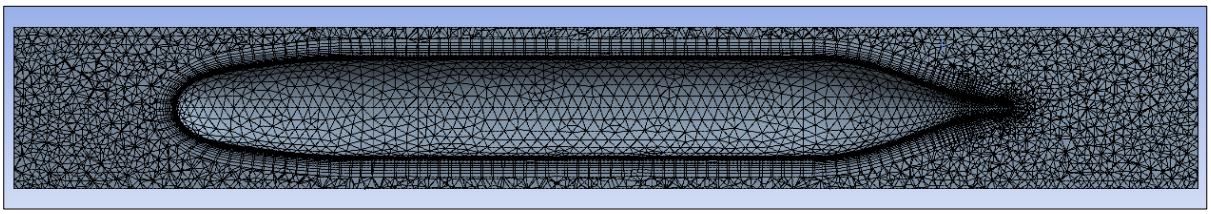

Figure AII.11: SUBOFF subdomain mesh

Explorer Subdomain

i. Clear generated mesh.

ii. Suppress the main fluid domain and SUBOFF subdomain, leaving only the Explorer subdomain active.

iii. Create the Explorer mesh using steps ii-vii from the instructions for creating the SUBOFF mesh.

iv. Export mesh as *ExplorerDomain.meshdat*

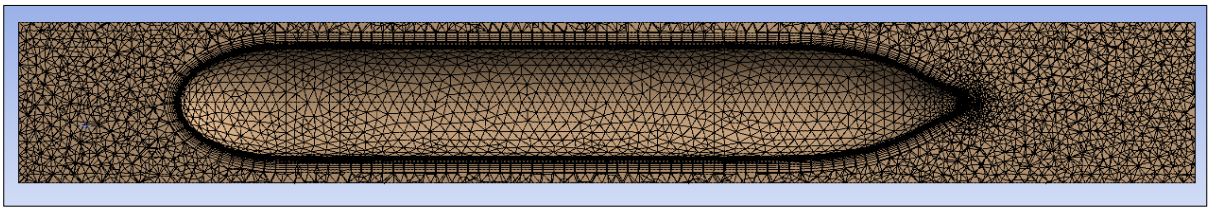

Figure AII.12: Explorer subdomain mesh

Fluid Domain

i. Reset only the mesh module under the WorkBench project schematic.

ii. Suppress the SUBOFF and Explorer subdomain, leaving only the fluid domain active.

iii. General mesh settings (unless specified, default used):

- Solver preference > CFX
- Advanced Size Function > On: Proximity
- Smoothing > High
- Proximity accuracy > 0.2
- Nums Cells Across Gap > 10
- Proximity Min Size > 0.02 (Same as the face size for the SUBOFF interface)
- Max face size > 0.5m
- Max size > 0.5m

iv. Specify the same face sizing for the surfaces interfacing between the fluid domain and SUBOFF subdomain, and the surfaces interfacing between the fluid domain and the Explorer domain.

v. Generate mesh.

vi. Save changes to project file.

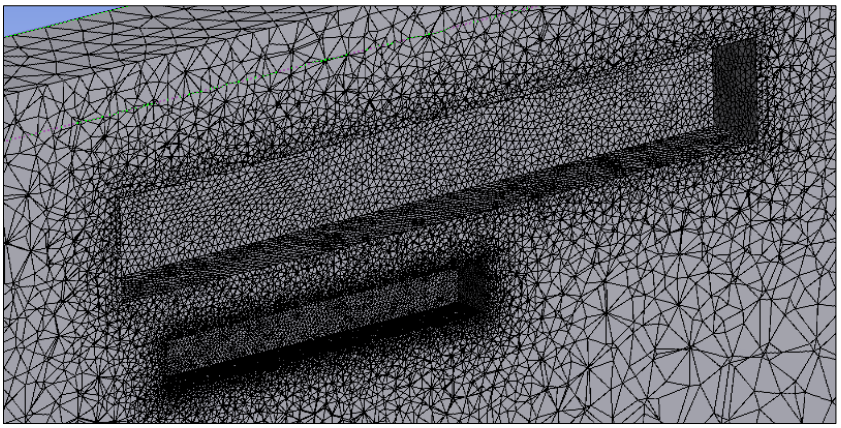

Figure AII.13: Fluid Domain mesh

AII.6 Prescribed Motion Test Case

AII.6.1 Geometry

The AUV and larger vehicle are represented by the Explorer and SUBOFF respectively. The dimension of the fluid domain is 20m long, 3.55m wide and 1.5m high in order replicate the dimensions of the AMC Towing Tank. It is noted the towing tank length of 100m was shortened to 20m as two vehicles are fixed in the longitudinal direction, whereby their forward motions were modelled by prescribed an equivalent flow speed in the opposite direction.

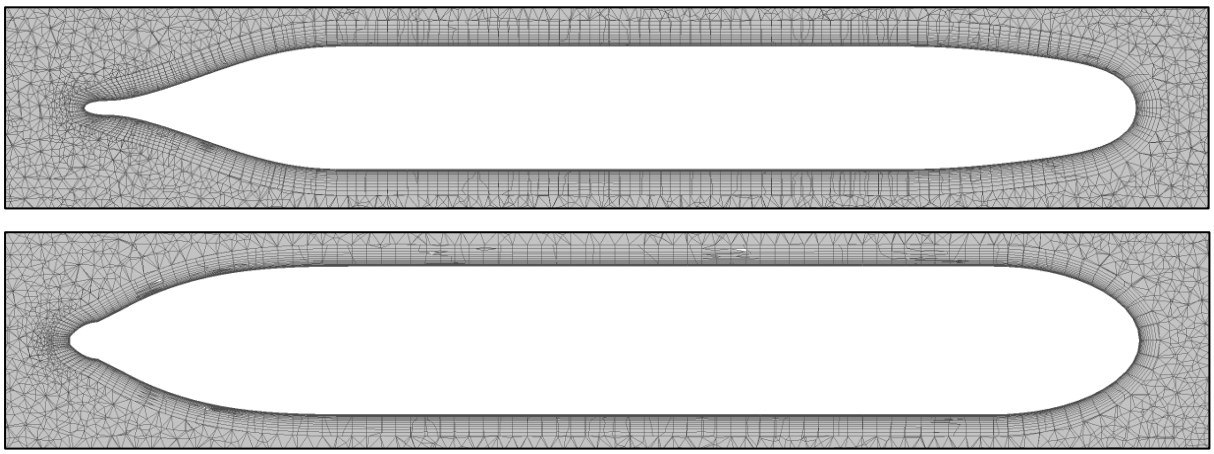

Figure AII.14: Mesh model of the SUBOFF and Explorer

AII.6.2 Test Case Condition

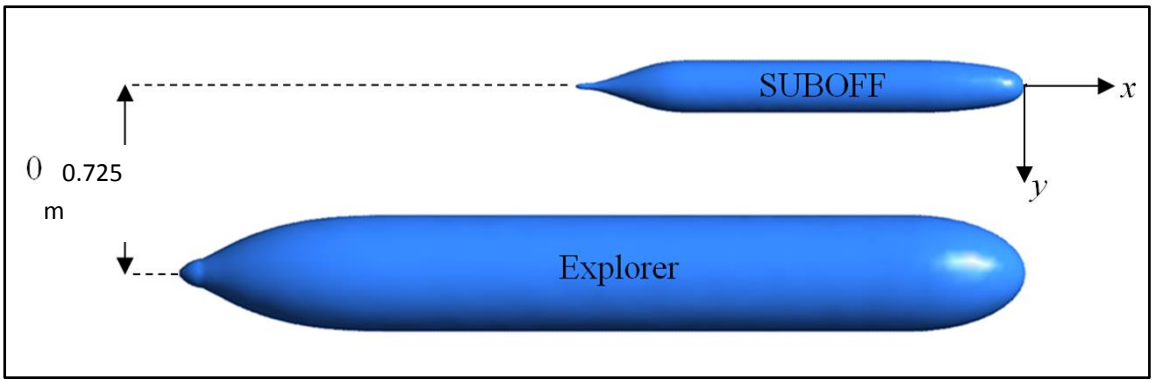

Figure AII.15: Initial location of the two vehicles

The global coordinate centre of origin is located at the nosetip of the SUBOFF. The Explorer nosetip is initially located 0.725m laterally and 0m longitudinally with respect to the SUBOFF nosetip as shown in Figure AII.15. Both vehicles are fully submerged in water with a depth of 0.75m along their nosetip and are located 5m aft the Inlet fluid domain boundary. Both vehicles travel forward at a speed of 1.2m/s while the SUBOFF undergoes an additional oscillatory transverse motion. A summary of the test conditions are given in Table AII.1.

Table AII.1: Prescribed motion test case parameters

Parameter	**SUBOFF**	**Explorer**
Initial nosetip coordinate [x, y, z]	0m, 0m, 0.75m	0m, 0.725m, 0.75m
Forward speed, U_0	1.2m/s	1.2m/s
Re_{Length}	2.10×10^6	3.96×10^6
Transverse displacement amplitude, a	0.14m	-
Transverse oscillation frequency, f	0.2Hz	-
Angle of incidence, θ	0°	0°
Water density, ρ	997 kg/m^3	
Water dynamic viscosity, μ	8.899×10^{-4} kg/ms	

AII.6.3 Test Case Simulation: CFX-Pre Setup

Note: Red font = expression

General

i. Create the mesh models of the fluid domain and the vehicle subdomains at their initial locations following the instructions in Section 3.

ii. Open CFX-Pre.

iii. Go to Edit>Options> CFX-Pre>General> Auto Generation and disable Automatic Default Interfaces

iv. Create a new General Case and save as "SUBOFFExplorer.cfx" in working directory

v. Import the subdomain meshs - Right click on Mesh tree > Import Mesh > ANSYS Meshing. Change file filter to all files to find the *.meshdat files

vi. Import the outer domain mesh from workbench project archive, e.g. [working directory]/SUBOFFExplorer_files/dp0/MECH/SYS.mshdb

vii. Simulation>Flow Analysis 1> Analysis Type>

- Option> Transient
- Time Duration> Option> Total Time
    - Total Time > CSimTime
- Time Steps>
    - Option > Timesteps
    - Timesteps > CSimTimeStep
- Initial Time>
    - Option > Automatic with Value
    - Time > 0 [s]

<u>Fluid Domain</u>

i. Rename ' Default Domain' to 'FluidDomain'

ii. FluidDomain > Basic Settings >

- Location and Type >
    - Location > ….. (Select all three mesh)
    - Domain Type > Fluid Domain
    - Fluid 1 > Option > Material > Water
    - Domain Models > Pressure > Reference Pressure > 1 [atm]
    - Buoyancy Model > Non-Buoyant
    - Domain Motion > Stationary
    - Mesh Deformation>
        - Option > Regions of Motion Specified
        - Mesh Motion Model > Option > Displacement diffusion
        - Mesh stiffness >
            - Option > Increase near Boundaries

- Model Exponent > 10

Vehicle Subdomain

i. Right click on FluidDomain and insert Subdomain 1 for the SUBOFF subdomain
ii. Subdomain: Subdomain 1 >
    - Basic Settings > Location > [Select SUBOFF subdomain]
    - Mesh Motion > Mesh Motion >
        - Option > Specified Displacement
        - Displacement >
            - Option > Cartesian Components
            - X Component > 0 [m]
            - Y Component > SUBOFFDisplaceY
            - Z Component > 0 [m]
iii. Right click on FluidDomain and insert Subdomain 2 for the Explorer subdomain
iv. Subdomain: Subdomain 2 >
    - Basic Settings > Location > [Select Explorer subdomain]
    - Mesh Motion > Mesh Motion >
        - Option > Specified Displacement
        - Displacement > Option > Stationary

Note: This allows the mesh within the subdomains to be rigid, allowing deformation to occur only in the main fluid domain.

Subdomain Interface

i. Right click on FluidDomain and insert Domain Interface 1 for SUBOFF subdomain. Note: This will also create boundaries 'Domain Interface 1 Side 1' and 'Domain Interface 1 Side 2'
ii. Domain Interface 1>
    - Basic Settings >
        - Interface Type > Fluid Fluid
        - Interface Side 1
            - Domain (Filter) > FluidDomain
            - Region List > SUBOFFInnerInterface
        - Interface Side 2

- Domain (Filter) > FluidDomain
- Region List > SUBOFFOuterInterface

- Additional Interface Models >
  - Mass and Momentum > Conservative Interface Flux
- Mesh Connection Method >
  - Mesh Connection > GGI

iii. Fluid Domain>

- Domain Interface: Domain Interface 1 Side 1 > Boundary Details >
  - Mesh Motion >
    - Option > Specified Displacement
      - Displacement >
        - Option > Cartesian Components
        - X Component > 0 [m]
        - Y Component > SUBOFFDisplaceY
        - Z Component > 0 [m]
- Domain Interface: Domain Interface 1 Side 2 > Boundary Details >
  - Mesh Motion >
    - Option > Specified Displacement
      - Displacement >
        - Option > Cartesian Components
        - X Component > 0 [m]
        - Y Component > SUBOFFDisplaceY
        - Z Component > 0 [m]

iv. Right click on FluidDomain and insert Domain Interface 2 for Explorer subdomain. Note: This will also create boundaries ‘Domain Interface 2 Side 1’ and ‘Domain Interface 2 Side 2’

v. Domain Interface 2>

- Basic Settings >
  - Interface Type > Fluid Fluid
  - Interface Side 1
    - Domain (Filter) > FluidDomain
    - Region List > ExplorerInnerInterface

- Interface Side 2
    - Domain (Filter) > FluidDomain
    - Region List > ExplorerOuterInterface
- Additional Interface Models >
    - Mass and Momentum > Conservative Interface Flux
- Mesh Connection Method >
    - Mesh Connection > GGI

vi. Fluid Domain>

- Domain Interface: Domain Interface 2 Side 1 > Boundary Details >
    - Mesh Motion >
        - Option > Stationary
- Domain Interface: Domain Interface 2 Side 2 > Boundary Details >
    - Mesh Motion >
        - Option > Stationary

<u>Domain Boundaries</u>

i. Inlet:

i. Right click on Fluid Domain and insert boundary 'Inlet'

ii. Fluid Domain > Boundary: Inlet >

- Basic Settings >
    - Boundary Type > Inlet
    - Location > Inlet
- Boundary Details >
    - Mass and Momentum >
        - Option > Cart. Vel. Components
        - U > DomainFlowSpeedU
        - V > 0 [m s^-1]
        - W > 0 [m s^-1]

ii. Outlet:

i. Right click on Fluid Domain and insert boundary 'Outlet'

ii. Fluid Domain > Boundary: Outlet >

- Basic Settings >

- Boundary Type > Opening
- Location > Outlet

- Boundary Details >
  - Mass and Momentum >
    - Option > Opening Pres. And Dirn
    - Relative Pressure > 0 [Pa]

iii. Wall:

i. Right click on Fluid Domain and insert boundary ‘Wall’

ii. Fluid Domain > Boundary: Wall >

- Basic Settings >
  - Boundary Type > Wall
  - Location > Wall
- Boundary Details >
  - Mass and Momentum >
    - Option > Free Slip Wall

iv. SUBOFF:

v. Right click on Fluid Domain and insert boundary ‘SUBOFF’

vi. Fluid Domain > Boundary: SUBOFF >

- Basic Settings >
  - Boundary Type > Wall
  - Location > SUBOFF
- Boundary Details >
  - Mesh Motion >
    - Option > Specified Displacement
    - Displacement >
      - Option > Cartesian Components
      - X Component > 0 [m]
      - Y Component > SUBOFFDisplaceY
      - Z Component > 0 [m]
  - Mass and Momentum >
    - Option > No Slip Wall

vii. *Explorer:*

i. Right click on Fluid Domain and insert boundary 'Explorer'

ii. Fluid Domain > Boundary: Explorer >

- Basic Settings >
  - Boundary Type > Wall
  - Location > Explorer
- Boundary Details >
  - Mesh Motion > Option > Stationary
  - Mass and Momentum > Option > No Slip Wall

Domain Initialization

i. FluidDomain > Initialization

- Domain Initialization > Initial Conditions >
  - Cartesian Velocity Components >
    - Option > Automatic with Value
    - U > DomainInletFlowSpeed
    - V > 0 [m s^-1]
    - W > 0 [m s^-1]
  - Static Pressure >
    - Option > Automatic with Value
    - Relative Pressure > 0 [Pa]

viii. Solver

i. Solver Control > Basic Settings >

- Advection Scheme > High Resolution
- Transient Scheme >
  - Option > Second Order Backward Euler
  - Timestep Initialization > Automatic
- Turbulence Numerics > Option > First Order
- Convergence Control >
  - Min. Coeff. Loops > 1
  - Max. Coeff. Loops > 3

- Interrupt Control > Interrupt Control Conditions >
    - Insert ‘Interrupt Condition 1’
    - Interrupt Condition 1 >
        - Option > Logical Expression
        - Logical Expression > MeshOrthoAngle < 10

ii. Right click on Solver and insert ‘Expert Parameters’

- Expert Parameters > Discretisation > meshdisp diffusion scheme > value > 3

  (Note: This improves the diffusion of the mesh deformation thus extending the mesh deformation allowed before compromising the mesh quality)
- Expert Parameters > Convergence Control > Memory Control >
    - Enable ‘topology estimate factor’
    - Value = 1.2

  (Note: This prevents memory issues as the preallocated memory is fixed during simulation)

iii. Output Control >

- Trn Results > Transient Results >
    - Insert ‘Transient Results 1’
    - Transient Results 1 >
        - Output Frequency >
            - Option > None
- Monitor > Monitor Points and Expressions >
    - Insert the monitor points below. Note that it is essential that the names of the monitor points tracking the position of the SUBOFF be identical to the names of their respective parameters in WorkBench for the remeshing process.
        - Monitor Point Name > SUBOFF_LocX
            - Expression Value >

              ave(Total Centroid Displacement X)@SUBOFF
        - Monitor Point Name > SUBOFF_LocY
            - Expression Value >

              ave(Total Centroid Displacement Y)@SUBOFF
        - Monitor Point Name > SUBOFF_LocZ
            - Expression Value >

ave(Total Centroid Displacement Z)@SUBOFF

- Monitor Point Name > SUBOFF_Fx
  - Expression Value > force_x()@SUBOFF
- Monitor Point Name > SUBOFF_Fy
  - Expression Value > force_y()@SUBOFF
- Monitor Point Name > SUBOFF_Fz
  - Expression Value > force_z()@SUBOFF
- Monitor Point Name > Explorer_Fx
  - Expression Value > force_x()@Explorer
- Monitor Point Name > Explorer_Fy
  - Expression Value > force_y()@Explorer
- Monitor Point Name > Explorer_Fz
  - Expression Value > force_z()@Explorer
- Monitor Point Name > MeshAngleQuality
  - Expression Value > MeshOrthoAngle

ix. <u>Expressions</u>

i. Insert the following expressions:

- Expression Name > CSimTime
  - Definition > 20 [s]
- Expression Name > CSimTimeSteps
  - Definition > 0.01 [s]
- Expression Name > DomainFlowSpeedU
  - Definition > -1.2 [m s^-1]
- Expression Name > MeshOrthoAngle
  - Definition >

180/pi*minVal(Orthogonality Angle Minimum)@REGION:B40

(Note: B40 is the reference ID of the main FluidDomain mesh. To insert, right click on the definition window for the expression, Mesh Locator > 3D > [select the FluidDomain ref. ID]. To check if the reference ID is correct, extend the Mesh tree.

- Expression Name > SUBOFFDisplaceY
    - Definition > DesiredSUBOFFDisplaceY - ReinitialSUBOFFDisplaceY
- Expression Name > DesiredSUBOFFDisplaceY
    - Definition > 0.14[m]*sin(2*pi*0.2*t/1[s])
- Expression Name > ReinitialSUBOFFDisplaceY
    - Definition > 0.14[m]*sin(2*pi*0.2*Mesh Initialisation Time/1[s])

(Note: The *Total Centroid Displacement* variable tracks the displacement of each boundary's centroid since the beginning of the analysis (that is, relative to the original mesh). The specified displacement based mesh motion is relative to the initial mesh and must therefore include an offset to account for mesh re-initialization. The *Mesh Initialisation Time* variable corresponds to the time at which mesh re-initialization last occurred. This is essential for prescribed motion simulations that utilise the remeshing option.)

x. Execution Control

i. Right on Simulation Control and insert 'Execution Control'

- Execution Control >
    - Run Definition >
        - Solver Input File > [working directory]/SUBOFFExplorer.def
    - Parallel Environment
        - Run Mode > Platform MPI Local Parallel
        - Number of Processes > 7

          (Note: Select the parallel run mode available on the operating system. The number of processes specified should be at least one core processer less than the total available processers on the computer)
    - Partitioner >
        - Partitioning Detail >

- Partitioner Type > Optimised R.C.B.
- Partitioning Weighting > Automatic

- Partitioner Memory >
  - Memory Alloc Factor > 1.4

- Solver >
  - Solver Memory >
    - Memory Alloc Factor > 1.4

(Note: The Memory Alloc Factor of 1.4 for both the Partitioner prevents the 'insufficient memory error' encountered with the default options)

xi.

xii. Remeshing Configuration

i. Right click on Configuration and insert 'Configuration 1'

- Configuration 1 >
  - General Settings >
    - Insert 'Activation Condition 1'
      - Activation Condition 1 >
        - Option > Start of Simulation
  - Remeshing >
    - Under Remesh Definitions, insert 'Remesh 1'
    - Remesh 1 >
      - Option > User Defined
      - Activation Condition(s) > Interrupt Condition 1
      - Location > B40
        (Note: Specify the FluidDomain reference ID)
      - External Command >

/ansys_inc/v140/Framework/bin/Linux64/runwb2 -B –R /[working directory]/WB_Remesh.wbjn

- Replacement File >

/[working directory]/SUBOFFExplorer_files/dp0/MECH/SYS.mshdb

(Note: The WB_Remesh.wbjn is the user-defined remeshing script developed by ANSYS and is in the example files provided)

xiii. Finalising the CFX-Pre Setup

i. Check if there are any error messages in the message box and amend them before proceeding further.

ii. Write the solver definition file

- Right click on Simulation Control and select 'Write Solver Input File'

iii. Simulation is ready to be initialised using the solver definition file, SUBOFFExplorer.def.

AII.6.4 Prescribed Motion Results

The simulation was performed with:

- the SUBOFF and Explorer undergoing a forward speed of 1.2m/s;
- the SUBOFF undergoing a oscillatory motion in the transverse (*y*) direction with amplitude of 0.14m and a frequency of 0.2Hz; and
- the SUBOFF nosetip at an initial position of 0.75m laterally and 0m longitudinally relative to the Explorer nosetip.

Figures AII.16 and AII.17 show the simulation predictions of the longitudinal force and lateral force acting on the SUBOFF, respectively. The simulations were carried out using the BSLRSM turbulence model and a time step of 0.01s.

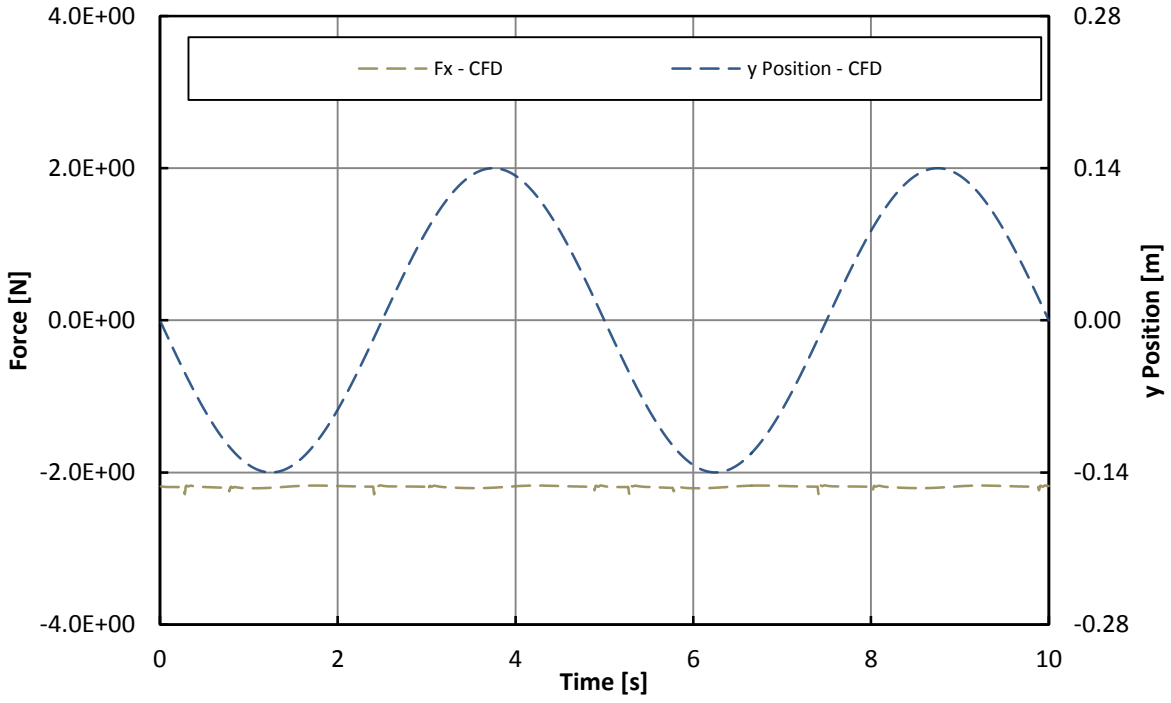

Figure AII.16: Simulation results of the SUBOFF transverse position and longitudinal force (Fx)

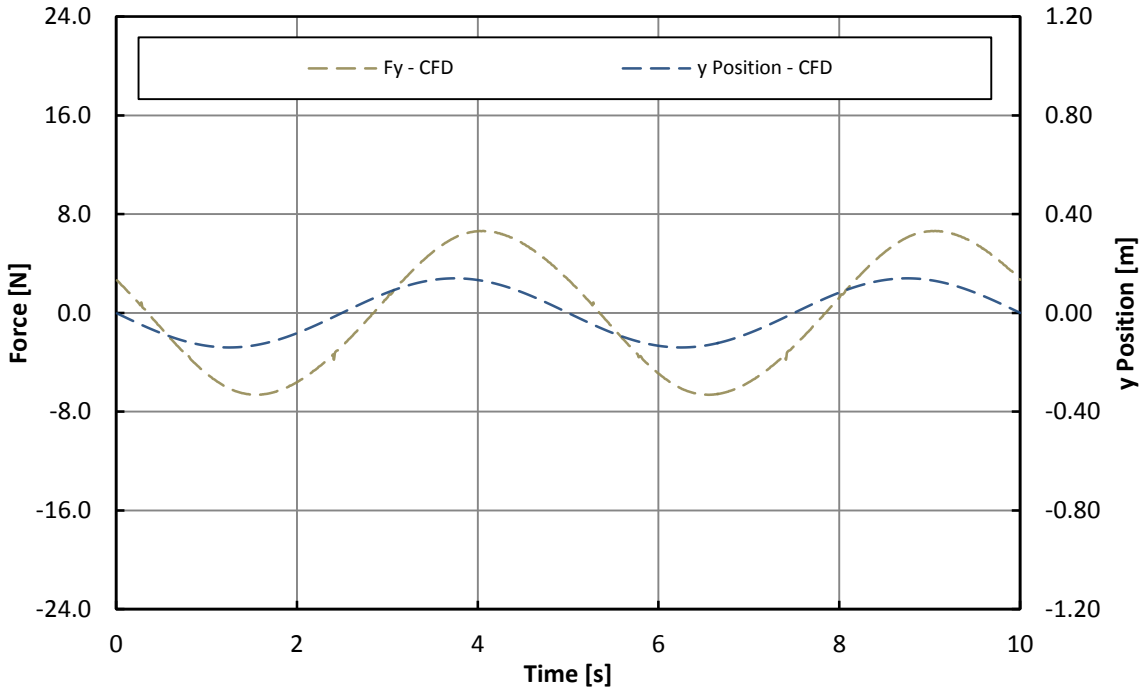

Figure AII.17: Simulation results of the SUBOFF transverse position and transverse force (Fy)

AII.7 Motion Response Test Case

AII.7.1 Geometry

The vehicle is represented by the SUBOFF model. The dimension of the fluid domain is 20m long, 3.55m wide and 1.5m high in order replicate the dimensions of the AMC Towing Tank.

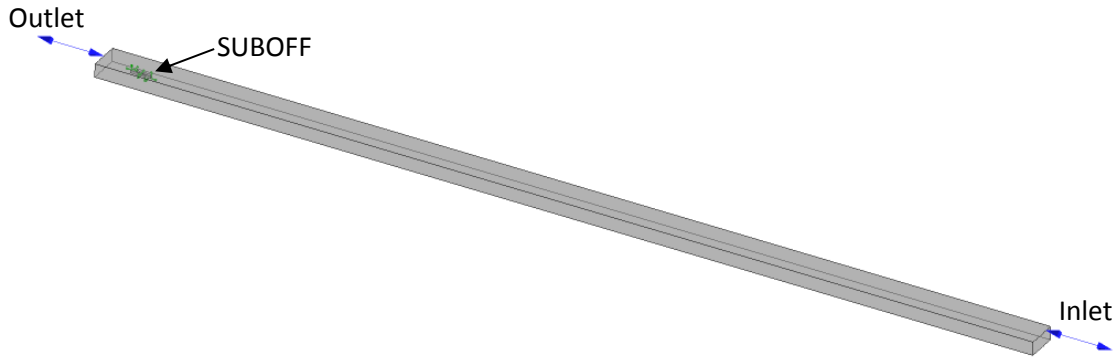

Figure AII.18: Motion response test case fluid domain

AII.7.2 Test Case Condition

A prescribed motion simulation was first carried out to determine the longitudinal force acting on the SUBOFF while it travels forwards 1.2m/s. The obtained longitudinal force, -1.5N, was prescribed as an external force in the opposite direction, representing thrust, on the SUBOFF in a coupled CFD-RBD simulation in order to examine the capability of the CFD-RBD simulation in reproducing the motion of the SUBOFF moving forward at 1.2m/s. The mesh model is the same for both the prescribed motion simulation and motion response simulation.

For the test case, the SUBOFF nosetip is initially located 10m fore of Outlet fluid domain boundary and at a depth of 0.75m. A summary of the test conditions and the rigid body parameters of the SUBOFF are given in Table AII.2.

Table AII.2: Motion response test case parameters

Parameter	**SUBOFF**
Initial nosetip coordinate [*x*, *y*, *z*]	5m,0m,-0.75m
Mass	318.6kg
Mass moment of inertia [I_{xx}, I_{yy}, I_{zz}, I_{xy}, I_{xz}, I_{yz}]	31.86kgm^2
Prescribed external force	1.5N in *x*-direction
Degrees of Freedom	1; *x*-axis translation
Initial linear velocity	1.2m/s in *x-direction*

AII.7.3 Test Case Simulation: CFX-Pre Setup

Note: Red font = expression

General

i. Create the mesh models of the fluid domain and the vehicle subdomain at its initial locations following the instructions in Section 3.
ii. Open CFX-Pre.
iii. Go to Edit>Options> CFX-Pre>General> Auto Generation and disable Automatic Default Interfaces
iv. Create a new General Case and save as "SUBOFF.cfx" in working directory
v. Import the subdomain meshs - Right click on Mesh tree > Import Mesh > ANSYS Meshing. Change file filter to all files to find the *.meshdat files
vi. Import the outer domain mesh from workbench project archive, e.g. [working directory]/SUBOFF_files/dp0/MECH/SYS.mshdb

vii. Simulation>Flow Analysis 1> Analysis Type>

- Option> Transient
- Time Duration> Option> Total Time
    - Total Time > CSimTime
- Time Steps>
    - Option > Timesteps
    - Timesteps > CSimTimeStep
- Initial Time>
    - Option > Automatic with Value
    - Time > 0 [s]

Rigid Body

i. Right click on Flow Analysis 1 and insert Rigid Body 1 for the SUBOFF

ii. Rigid Body: Rigid Body 1 >

- Basic Settings >
    - Mass > 318.6 [kg]
    - Location > SUBOFF
    - Mass moment of inertia > 31.86 [kgm^2] for all
- Dynamics >
    - External Force 1 >
        - Option > Value
        - Force >
            - Option > Cartesian Components
            - X Component > 1.5 [N]
            - Y Component > 0 [N]
            - Z Component > 0 [N]
    - Degrees of Freedom >
        - Translational Degrees of Freedom >
            - Option > X axis
- Initial Conditions >
    - Linear Velocity >
        - Option > Automatic with Value

- X Component > 1.2 [ms^-1]
- Y Component > 0 [ms^-1]
- Z Component > 0 [ms^-1]

Fluid Domain

i. Rename ‘ Default Domain’ to ‘FluidDomain’
ii. FluidDomain > Basic Settings >
    - Location and Type >
        - Location > ….. (Select all three mesh)
        - Domain Type > Fluid Domain
        - Fluid 1 > Option > Material > Water
        - Domain Models > Pressure > Reference Pressure > 1 [atm]
        - Buoyancy Model > Non-Buoyant
        - Domain Motion > Stationary
        - Mesh Deformation>
            - Option > Regions of Motion Specified
            - Mesh Motion Model > Option > Displacement diffusion
            - Mesh stiffness >
                - Option > Increase near Boundaries
                - Model Exponent > 10

Vehicle Subdomain

i. Right click on FluidDomain and insert Subdomain 1 for the SUBOFF subdomain
ii. Subdomain: Subdomain 1 >
    - Basic Settings > Location > [Select SUBOFF subdomain]
    - Mesh Motion > Mesh Motion >
        - Option > Rigid Body Solution
        - Rigid Body > Rigid Body 1

Subdomain Interface

i. Right click on FluidDomain and insert Domain Interface 1 for SUBOFF subdomain.
ii. Domain Interface 1>
    - Basic Settings >

- Interface Type > Fluid Fluid
- Interface Side 1
    - Domain (Filter) > FluidDomain
    - Region List > SUBOFFInnerInterface
- Interface Side 2
    - Domain (Filter) > FluidDomain
    - Region List > SUBOFFOuterInterface
- Additional Interface Models >
    - Mass and Momentum > Conservative Interface Flux
- Mesh Connection Method >
    - Mesh Connection > GGI

iii. Fluid Domain>

- Domain Interface: Domain Interface 1 Side 1 > Boundary Details >
    - Mesh Motion >
        - Option > Rigid Body Solution
        - Rigid Body > Rigid Body 1
- Domain Interface: Domain Interface 1 Side 2 > Boundary Details >
    - Mesh Motion >
        - Option > Rigid Body Solution
        - Rigid Body > Rigid Body 1

Domain Boundaries

Inlet:

i. Right click on Fluid Domain and insert boundary ‘Inlet’

ii. Fluid Domain > Boundary: Inlet >

- Basic Settings >
    - Boundary Type > Opening
    - Location > Inlet
- Boundary Details >
    - Mass and Momentum >
        - Option > Opening Pres. And Dirn
        - Relative Pressure > 0 [Pa]

Outlet:

i. Right click on Fluid Domain and insert boundary ‘Outlet’
ii. Fluid Domain > Boundary: Outlet >
    - Basic Settings >
        - Boundary Type > Opening
        - Location > Outlet
    - Boundary Details >
        - Mass and Momentum >
            - Option > Opening Pres. And Dirn
            - Relative Pressure > 0 [Pa]

Wall:

i. Right click on Fluid Domain and insert boundary ‘Wall’
ii. Fluid Domain > Boundary: Wall >
    - Basic Settings >
        - Boundary Type > Wall
        - Location > Wall
    - Boundary Details >
        - Mass and Momentum >
            - Option > Free Slip Wall

SUBOFF:

i. Right click on Fluid Domain and insert boundary ‘SUBOFF’
ii. Fluid Domain > Boundary: SUBOFF >
    - Basic Settings >
        - Boundary Type > Wall
        - Location > SUBOFF
    - Boundary Details >
        - Mesh Motion >
            - Option > Rigid Body Solution
            - Rigid Body > Rigid Body 1
        - Mass and Momentum >

- Option > No Slip Wall

Domain Initialization

i. FluidDomain > Initialization
    - Domain Initialization > Initial Conditions >
        - Cartesian Velocity Components >
            - Option > Automatic with Value
            - U > 0 [m s^-1]
            - V > 0 [m s^-1]
            - W > 0 [m s^-1]
        - Static Pressure >
            - Option > Automatic with Value
            - Relative Pressure > 0 [Pa]

Solver

i. Solver Control > Basic Settings >
    - Advection Scheme > High Resolution
    - Transient Scheme >
        - Option > Second Order Backward Euler
        - Timestep Initialization > Automatic
    - Turbulence Numerics > Option > First Order
    - Convergence Control >
        - Min. Coeff. Loops > 1
        - Max. Coeff. Loops > 3
    - Interrupt Control > Interrupt Control Conditions >
        - Insert ‘Interrupt Condition 1’
        - Interrupt Condition 1 >
            - Option > Logical Expression
            - Logical Expression > MeshOrthoAngle < 10

ii. Right click on Solver and insert ‘Expert Parameters’
    - Expert Parameters > Discretisation > meshdisp diffusion scheme > value > 3
    - Expert Parameters > Convergence Control > Memory Control >

- Enable ‘topology estimate factor’
- Value = 1.2

iii. Output Control >

- Trn Results > Transient Results >
  - Insert ‘Transient Results 1’
  - Transient Results 1 >
    - Output Frequency >
      - Option > None
- Monitor > Monitor Points and Expressions >
  - Insert the monitor points below. Note that it is essential that the names of the monitor points tracking the position and orientation of the SUBOFF be identical to the names of their respective parameters in WorkBench for the remeshing process.
    - Monitor Point Name > SUBOFF_RollAngle
      - Expression Value >
        (rbstate(Euler Angle X)@SUBOFF)*180/pi
    - Monitor Point Name > SUBOFF_PitchAngle
      - Expression Value >
        (rbstate(Euler Angle Y)@SUBOFF)*180/pi
    - Monitor Point Name > SUBOFF_YawAngle
      - Expression Value >
        (rbstate(Euler Angle Z)@SUBOFF)*180/pi
    - Monitor Point Name > SUBOFF_LocX
      - Expression Value >
        ave(Total Centroid Displacement X)@SUBOFF
    - Monitor Point Name > SUBOFF_LocY
      - Expression Value >
        ave(Total Centroid Displacement Y)@SUBOFF
    - Monitor Point Name > SUBOFF_LocZ
      - Expression Value >
        ave(Total Centroid Displacement Z)@SUBOFF
    - Monitor Point Name > SUBOFF_VelP
      - Expression Value >

rbstate(Angular Velocity X)@SUBOFF

- Monitor Point Name > SUBOFF_VelQ
  - Expression Value >

    rbstate(Angular Velocity Y)@SUBOFF
- Monitor Point Name > SUBOFF_VelR
  - Expression Value >

    rbstate(Angular Velocity Z)@SUBOFF
- Monitor Point Name > SUBOFF_VelU
  - Expression Value >

    rbstate(Linear Velocity X)@SUBOFF
- Monitor Point Name > SUBOFF_VelV
  - Expression Value >

    rbstate(Linear Velocity Y)@SUBOFF
- Monitor Point Name > SUBOFF_VelW
  - Expression Value >

    rbstate(Linear Velocity Z)@SUBOFF
- Monitor Point Name > SUBOFF_AccelPdot
  - Expression Value >

    rbstate(Angular Acceleration X)@SUBOFF
- Monitor Point Name > SUBOFF_AccelQdot
  - Expression Value >

    rbstate(Angular Acceleration Y)@SUBOFF
- Monitor Point Name > SUBOFF_AccelRdot
  - Expression Value >

    rbstate(Angular Acceleration Z)@SUBOFF
- Monitor Point Name > SUBOFF_AccelUdot
  - Expression Value >

    rbstate(Linear Acceleration X)@SUBOFF
- Monitor Point Name > SUBOFF_AccelVdot
  - Expression Value >

    rbstate(Linear Acceleration Y)@SUBOFF
- Monitor Point Name > SUBOFF_AccelWdot
  - Expression Value >

rbstate(Linear Acceleration Z)@SUBOFF

- Monitor Point Name > SUBOFF_Fx
  - Expression Value > force_x()@SUBOFF
- Monitor Point Name > SUBOFF_Fy
  - Expression Value > force_y()@SUBOFF
- Monitor Point Name > SUBOFF_Fz
  - Expression Value > force_z()@SUBOFF
- Monitor Point Name > MeshAngleQuality
  - Expression Value > MeshOrthoAngle

Expressions

i. Insert the following expressions:
   - Expression Name > CSimTime
     - Definition > 10 [s]
   - Expression Name > CSimTimeSteps
     - Definition > 0.01 [s]
   - Expression Name > MeshOrthoAngle
     - Definition > 180/pi*minVal(Orthogonality Angle Minimum)@REGION:B40

Execution Control

i. Right on Simulation Control and insert 'Execution Control'
   - Execution Control >
     - Run Definition >
       - Solver Input File > [working directory]/SUBOFF.def
     - Parallel Environment
       - Run Mode > Platform MPI Local Parallel
       - Number of Processes > 7
     - Partitioner >

- Partitioning Detail >
  - Partitioner Type > Optimised R.C.B.
  - Partitioning Weighting > Automatic
- Partitioner Memory >
  - Memory Alloc Factor > 1.4

- Solver >
  - Solver Memory >
    - Memory Alloc Factor > 1.4

Remeshing Configuration

i. Right click on Configuration and insert ‘Configuration 1’

- Configuration 1 >
  - General Settings >
    - Insert ‘Activation Condition 1’
      - Activation Condition 1 >
        - Option > Start of Simulation
  - Remeshing >
    - Under Remesh Definitions, insert ‘Remesh 1’
    - Remesh 1 >
      - Option > User Defined
      - Activation Condition(s) > Interrupt Condition 1
      - Location > B40

        (Note: Specify the FluidDomain reference ID)
      - External Command >

/ansys_inc/v140/Framework/bin/Linux64/runwb2 -B –R /[working directory]/WB_Remesh.wbjn

- Replacement File >

/[working directory]/SUBOFF_files/dp0/MECH/SYS.mshdb

Finalising the CFX-Pre Setup

i. Write the solver definition file as SUBOFF.def.

AII.7.4 Simulation Results

Figure AII.19 show the predicted position and velocity of the SUBOFF in response to the prescribed thrust force of 1.5N with respect to time. The averaged predicted linear velocity of the SUBOFF in the x-direction was 1.2m/s with a standard deviation of 0.01% (99% confidence level), matching the desired velocity response, 1.2m/s. The distance travelled after 10s was 12.01m which was within 0.08% of the analytical solution, 12.00m.

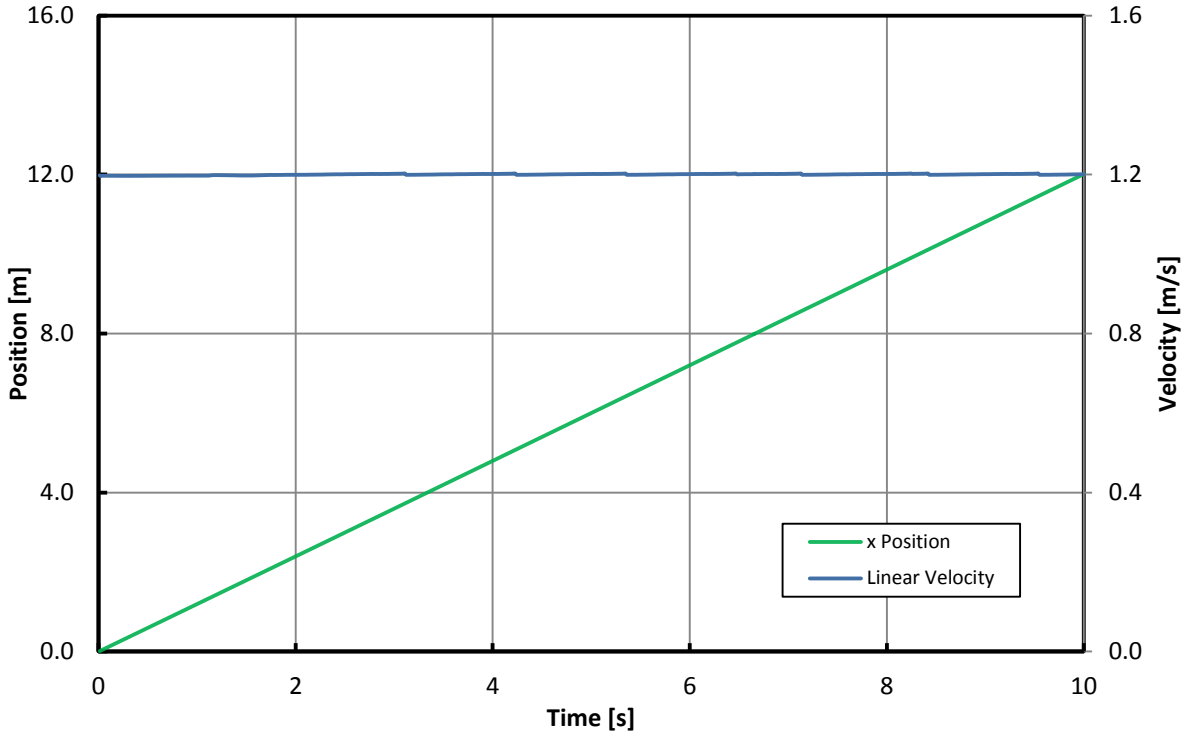

Figure AII.19: Simulation results of the SUBOFF position and velocity as a function of time for the motion response test case.

[Page intentionally left blank]

Appendix III :

The ANSYS CFX-MATLAB Interface

AIII.1 Introduction

This appendix presents an interface to couple the CFD model within ANSYS CFX to a control system within a MATLAB environment for manoeuvring simulations. The CFD model also includes a built-in Rigid Body Dynamics model that enables it to predict the motion response of the AUV to its control planes, propulsion, and external forces. The interface presented relies on the native languages of the ANSYS CFX module, the MATLAB module and the operating system, thus avoiding compatibility issue and the need for user defined subroutines within ANSYS CFX.

The capability of the interface is demonstrated through a simulation of an AUV moving in parallel to relative to a larger vehicle, with the AUV's propulsion controlled through the MATLAB environment. The results shown within this appendix have been produced to demonstrate capability. The results presented here must not be taken as accurate predictions.

AIII.2 Simulation Architecture

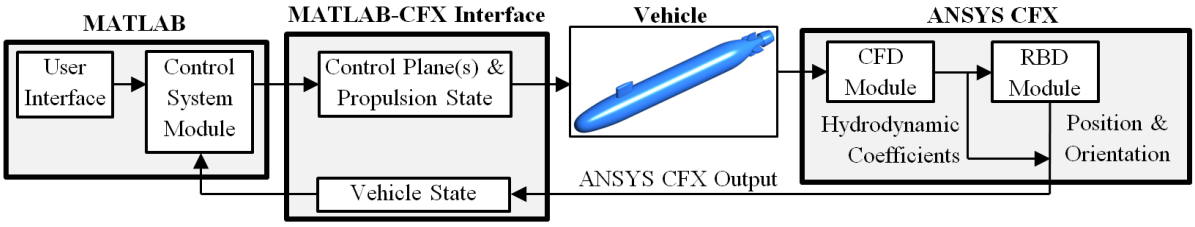

Figure AIII.1: Block diagram of the simulation subcomponents.

Figure AIII.1 shows the block diagram of the simulation architecture. The simulation is controlled via a user interface within the MATLAB environment. The simulation is controlled via the MATLAB environment whereby the test parameters and the vehicle control states can be changed either through the user interface or vehicle control system module. The hydrodynamic forces and moments of the vehicles, i.e. *X*, *Y*, *Z*, *K*, *M*, *N*, are computed using the CFD solver within ANSYS CFX. The motion of the vehicles, i.e. translation and rotation,

in response to the hydrodynamic components, gravitational forces, inertia forces, and additional external forces such as propulsion, are then computed by the 6-DOF RBD solver within ANSYS CFX. The ANSYS CFX output containing the external forces and moments, positions, Euler angles, velocities, and accelerations of the vehicles are transferred to the MATLAB-based control system through the ANSYS CFX-MATLAB Interface (ACMI). Based on the information from ANSYS-CFX, the control system computes the new states of the control components of the vehicles (e.g. control fins, propulsion or their equivalent forces and moment) in order to maintain the desired trajectory. The new states of the control components of the vehicles are transferred back into ANSYS CFX through the AMCI, and the control components of the vehicles within ANSYS CFX are updated accordingly. Figure AIII.2 shows the flow process of the ACMI.

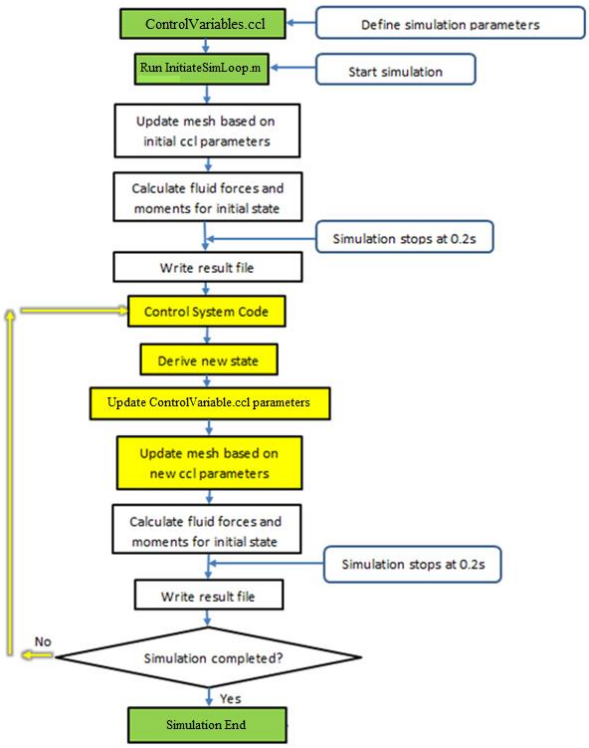

Figure AIII.2: Flow process of the ANSYS CFX-Matlab Interface simulation.

Note: The simulation generates a comma-separated-value format dat file containing the variables monitored by CFX which can be plotted in MATLAB. The dat file is updated when the simulation is interrupted every 0.2s.

AIII.3 Test Case (Implementaion of the ACMI)

The test case involves the DARPA sized SUBOFF overtaking a cylindrical-shaped body (Vehicle 2) which eight times larger than the former (see Figure AIII.3). The SUBOFF is propelled forward by a thrust force of 104N and has an initial speed of 0.8m/s in the *x*-direction at the start of the simulation. After 8s, the thrust force is reduced to 52N by the dummy control code in the MATLAB script. The purpose of the test case is to verify the capability of the interface to initiate and control the simulation using a MATLAB script. A summary of the test case conditions are summarized in Table AIII.1.

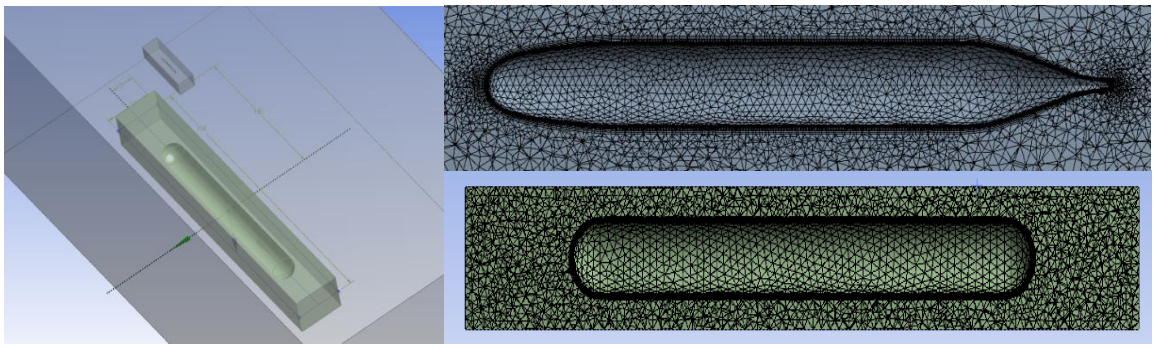

Figure AIII.3: Fluid domain and mesh model of the ACMI test case

Table AIII.1: ACMI test case parameters

Parameter	**SUBOFF**	**Vehicle 2**
Initial nosetip coordinate [*x, y, z*]	0m, 0m, 30m	30m, 3m, 30m
Length	4.356m	34m
Diameter	0.508m	4m
Mass	699.21kg	-
Mass moment of inertia [I_{xx}, I_{yy}, I_{zz}, I_{xy}, I_{xz}, I_{yz}]	69.92kgm^2	-
Motion	Solution Dependent (RBD)	Stationary
Prescribed thrust force	104N 52N (after 8s)	-
Inlet flow speed	1m/s	

AIII.3.1 Test Case Setup

The setup approach for the ANSYS CFX component of the simulation is similar to the motion response test case outlined in Appendix 2.

The simulation model files listed in Table AIII.2 are provided in the storage media attached to this thesis and online at <https://www.dropbox.com/s/d82o3gm8oca5c8m/Remesh18SuboffLinuxV1_170912.zip>.

A description of the terminal-based ANSYS CFX commands and MATLAB commands for the interface between the two environments is given in the M-files (*.m).

Table AIII.2: List of simulation files for the CFX-MATLAB interface test case

File	Description
Suboff.wbpj	Workbench project file.
Suboff_files	Workbench project subfolder containing the geometry and mesh files.
ControlVariables.ccl	Variables that can be controlled by the MATLAB environment. Edit parameters before initialising the simulation to set the initial conditions. The same file used by MATLAB to update the simulation variable when it is running.
InitiateSimLoop.m	MATLAB script used to initiate and control the CFX simulation.
ControlDummy.m	MATLAB script allowing results to be extracted system during simulation into a readable format (csv) by a MATLAB-based control system. Updates the simulation variables with the control outputs.
WB_Remesh.wbjn	The CFX re-meshing script. Generic, requires no modification.

AIII.3.2 Running the Simulation

i. Extract the simulation files to "/tmp/Remesh/". If another working directory is preferred, change the paths accordingly in the 'ControlVariables.ccl' file.
ii. Run the InitiateSimLoop.m to initiate the simulation.

AIII.3.3 ACMI Test Case Results

Figure AIII.4 shows the time history of the SUBOFF velocity in response to the thrust force prescribed by the MATLAB script. Slight fluctuations were observed at the start of the simulation which is normal due to the simulation calculating a reasonable equilibrium state in the first two to three time steps. The velocity of the SUBOFF increases up to the point of 8s where the prescribed thrust force is reduced to half. The velocity decreases thereafter as expected, thus verifying the capability of the MATLAB script to control the CFX simulation.

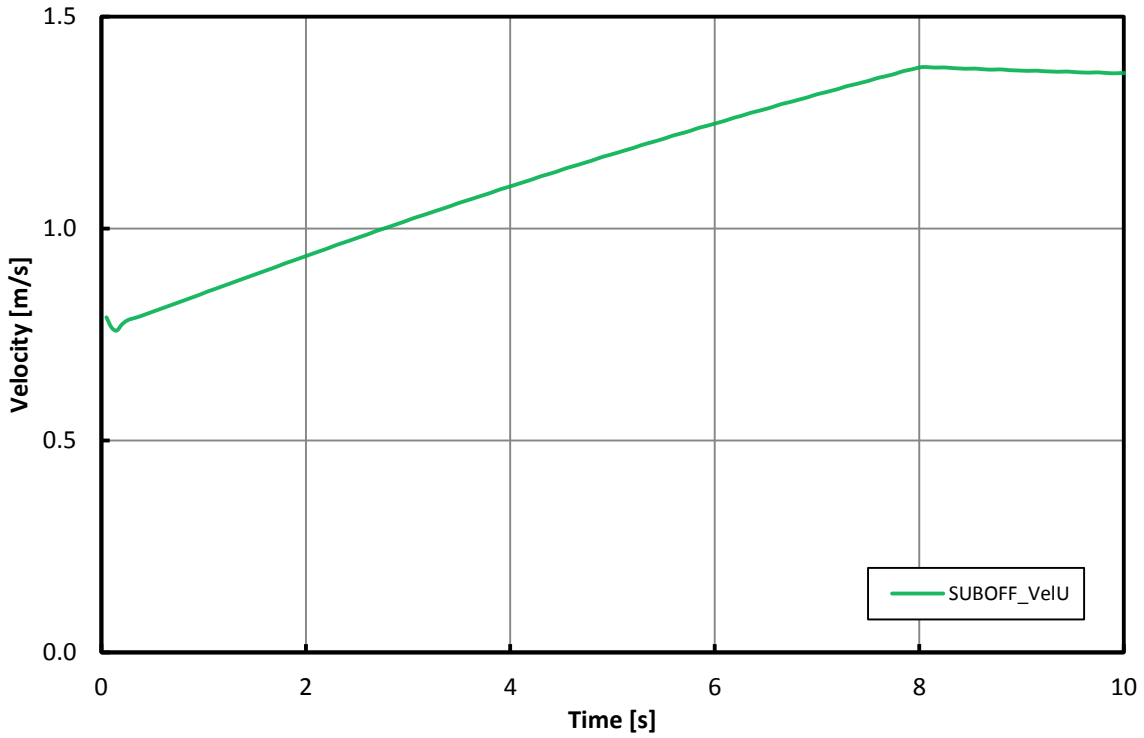

Figure AIII.4: Time history of the SUBOFF velocity in the *x*-direction in response to the prescribed thrust force by the MATLAB script.